Appendix C

Numerical Modeling Report

This page intentionally left blank.

Santa Susana Field Laboratory
Area IV Groundwater Numerical Modeling

US Department of Energy Task Order DE-DT0003515 Environmental Remediation Services for Environmental Compliance for Area IV

1. Introduction

The Santa Susana Field Laboratory is perhaps the most studied and characterized mountains in the State of California. Extensive efforts led by MWH as funded by The Boeing Company (Boeing), National Aeronautics and Space Administration (NASA), and the U.S. Department of Energy (DOE) have yielded a comprehensive site-wide (mountain-scale) flow model, which has been extensively calibrated against site-wide data (The Boeing Company, 2009). While the overall applicability and accuracy of the model is commendable, it must be noted that it was built and calibrated with the overarching goal of reflecting mountain-scale flows (magnitudes and directions) with particular emphasis on Areas I and III, areas that Boeing is responsible for and areas with the greatest contamination. Because the model was developed to reflect site-wide groundwater flows (general flow directions and magnitudes), it does not claim to represent a fine level of detail and does not claim to honor all known and inferred groundwater flow directions. In particular, because of the way that site characterization data are included into the calibration process, areas with higher data density tend to be those where the model is most accurate. Hence, Areas I and III are likely to be most accurate. While acknowledging the significant effort that has been spent calibrating the mountain-scale model, the DOE believes that the model may not characterize the flow paths in Area IV with sufficient accuracy to make important regulatory and remediation decisions. To improve DOE's ability to predict flow and transport in Area IV, we have modified the mountain-scale flow using an updated analysis of alluvium thickness, the most recent water-level data, and increased calibration weighting on wells in and around Area IV to ensure that these data will be honored and as a result more accurately reflect local groundwater flow conditions (although accuracies in other Areas may be sacrificed). The improved calibration will facilitate hypothesis testing with increased confidence. It is anticipated that simulated flow directions and particle paths in Area IV will be sufficiently accurate such that important monitoring and remediation decisions can be made by DOE and California Department of Toxic Substances Control (DTSC).

1.1 Purpose and Objectives

The DOE has funded Baylor University (Baylor) to update and recalibrate the Santa Susana Field Laboratory (SSFL) mountain-scale FEFLOW model (DHI-WASY, 2012). This work was undertaken with specific emphasis on calibrating model behavior in and around Area IV. This differs from the approach taken by Boeing because the mountain-scale model was calibrated to site-wide data in an effort to better understand how the various contamination plumes behave on a site-wide basis. This necessarily results in a model that balances simulated heads throughout the model domain according to the weighting scheme. While it is recognized that this is the best approach to understanding the entire flow system, this methodology does not focus on any specific region of the SSFL. For example, heads and flow paths in Area IV, of specific interest to the DOE, did not provide sufficient confidence to make decisions about future data collection efforts or remediation strategies. To address this deficiency, Baylor has recalibrated the SSFL mountain-scale model using a reinterpretation of the alluvium thickness in and around Area IV

and corresponding changes to recharge, removal of geologically inconsistent features, addition of a zone of anisotropy, an update to the unsaturated flow model, the latest site data, and increased weights on data local to Area IV.

Research for the DOE at the SSFL site includes:

- Interpretation of data and conceptual-model development for hydrogeology, groundwater flow, and contaminant transport at the SSFL site,
- Review of the existing FEFLOW mountain-scale numerical groundwater flow and contaminant transport model at the SSFL site,
- Technical review of groundwater investigations made by other parties at the SSFL site,
- Document and manuscript preparation related to groundwater issues for the DOE at SSFL Area IV,
- Participation in meetings between the DOE and regulatory agencies, such as the California DTSC, and potential public meetings, and
- Other technical tasks related to groundwater issues at SSFL as requested by the DOE.
- Options for presenting particle tracks including development of a 1-D FEHM contaminant-transport model based on particle tracks developed with the FEFLOW model in SSFL Area IV.

1.2 Background

Activities at SSFL since 1948 have included testing of liquid-fueled rocket engines, research associated with nuclear-energy applications, and various other activities related to liquid-metal engineering. Work at SSFL in general and Area IV in particular since the mid-1990s has focused on site restoration. Major categories of operational facilities at SSFL are rocket-engine testing stands, component testing, support and testing laboratories, materials testing and production, storage areas, landfills, surface water ponds, leach fields, sewage treatment, facilities maintenance, incinerators, and nuclear energy support (MWH, 2009). An area within Area IV designated as the Energy Technology Engineering Center (ETEC) was leased to DOE or DOE's predecessor (Atomic Energy Agency and the Energy Research and Development Administration) and was used for research and development of nuclear-energy technologies, liquid-metal heat exchanger components, lasers, and related technologies.

Groundwater contamination in Area IV related to DOE activities includes trichloroethylene (TCE) at the former sodium disposal facility (FSDF) and other locations, tritium near the former Building 4010, and Sr-90 at the Radioactive Materials Handling Facility (RMHF) leach field. Discernible groundwater migration of the tritium plume has occurred down gradient of the presumed source area; whereas movement of TCE contamination at various locations appears to be more complex and/or limited. Indications are that migration of the Sr-90 has been limited, likely due to sorption onto the bedrock medium.

1.3 Previous Groundwater Flow Modeling

Significant effort has been made to synthesize SSFL site data into a comprehensive conceptual model of groundwater flow, contaminant fate, and transport (MWH, 2009). This conceptual understanding has been included in the construction of the groundwater flow model of the site and adjacent areas, which was optimized to available data for the 2009 Groundwater RI report. The objectives of the groundwater flow

model included developing the conceptual model, estimating the overall water budget, understanding groundwater-discharge occurrences, investigating the impacts of historical groundwater withdrawals, quantifying fluxes from contaminant source locations, and evaluating the effectiveness of potential monitoring locations. The 2009 flow model was calibrated to observations of water levels in wells, surface-discharge locations, historical pumping data,. Particle tracking with the flow model was used to evaluate potential flow pathways from contaminant source areas.

Several modifications to the groundwater flow model were made in response to comments on the 2009 Groundwater RI report, culminating in the "Run 55" version of the model, completed in 2012. Changes to the model including adjustments to well depths and locations relative to faults, weighting of some head observations, splitting some recharge zones, additional zonation of the North Fault, long open boreholes represented as discrete elements, and grouping of shallow wells as perched wells. Most significantly for groundwater flow in Area IV, a surficial zone of higher hydraulic conductivity was added to prevent the simulation of excessive groundwater mounding in Area IV and the FSDF lineament structures were removed as high-conductivity zones based on observations in trenching across these apparent features. Although Run 55 was not formally documented in a report, modifications and results of this version of the model were technically reviewed by the SSFL groundwater working group, consisting of representatives from DOE, Boeing, and NASA.

Run 55 was the most recent model construction and calibration of the SSFL groundwater flow model completed by Matrix Solutions, a Boeing contractor. Baylor received the FEFLOW finite element model (FEM) and Interface Modules (IFMs) constructed by Matrix Solutions (specific FEFLOW input files that interrogate the model results). The FEM included all model-related information, such as the geological zoning and corresponding parameters. The IFMs were created by Matrix Solutions to facilitate input/output communications with the model so that recharge and hydraulic conductivities could be updated, and so that heads, gradients, and group flows and ratios could be exported as needed for the calibration process. This FEM and accompanying IFMs formed the basis of the groundwater flow model update by DOE. The calibrated parameter values resulting from Run 55 were used as initial conditions to begin the calibration of the updated model.

2. Groundwater Model

2.1 Conceptual Model

There is a long history of modeling at the SSFL going back to the site conceptual model (SCM) developed by Montgomery Watson (2000). This work described groundwater flow and the distribution and fate of TCE in both dense non-aqueous liquid (DNAPL) and dissolved phases. It also described the general occurrence of TCE in the unsaturated and saturated portions of the subsurface. However, a key concern following a review of the SCM in 2000 was that a representation of three-dimensional groundwater flow at the SSFL and the adjacent areas was needed. To this end, the SCM was updated (Cherry et al., 2007) and AquaResource Inc. and MWH Americas Inc. (2007) developed a three-dimensional mountain-scale FEFLOW (DHI-WASY, 2012) model of the site. Specifics of the conceptual model for groundwater flow, including the hydrogeologic framework, boundary conditions, and hydrogeologic parameters are described by MWH (2009).

The SSFL is located on a local topographic high (Simi Hills) 240–275 m (800–900 ft) above the surrounding valleys. Its primary constituent, the Chatsworth Formation, is a fractured and faulted sandstone with interbeds of siltstones, mudstones, and shales and it is the primary water-bearing geologic formation. The Chatsworth Formation has been uplifted and faulted such that geologic units dip to the northwest at an angle of 25° and are offset across faults. A thin layer of alluvium, which at certain times and locations contains perched groundwater, is found at numerous locations (with a large component in Area IV) and often overlies faults. At some locations within the SSFL, the groundwater in the Chatsworth Formation rises into this alluvium.

The groundwater system is recharged by precipitation throughout the Simi Hills and rates vary with the type of geologic material, slope, and precipitation (AquaResource Inc. and MWH Americas Inc., 2007). Because of fairly low hydraulic conductivities for fractured sandstone, depths to groundwater are relatively shallow (15–23 m or 50–75 ft). The elevation of groundwater at the SSFL is up to 275 m (900 ft) higher than the groundwater levels in the surrounding alluvial valleys (Simi and San Fernando Valleys). A simple comparison of area water levels suggests that general groundwater flow is from the higher elevations (Simi Hills) toward the topographically lower areas (alluvial valleys).

The complex stratigraphy and structural features of the Chatsworth Formation influence local three-dimensional groundwater flow including the local pathways and rate of movement of groundwater at the SSFL and adjacent areas. Groundwater flow directions are influenced by the storage and transmission properties of individual rock formations, complex interactions with multiple formations, and faults and shear zones. Higher groundwater elevations in the vicinity of the SSFL typically result in downward vertical head gradients (although local upward gradients are observed). Groundwater recharged in the Simi Hills ultimately discharges through a number seeps and phreatophytes on the slopes of the Simi Hills, lateral flow at depth toward and beneath adjacent valleys, and pumping on- and off-site. Therefore, a three-dimensional representation of hydrogeologic conditions is required to assess site-specific groundwater flow directions (AquaResource Inc. and MWH Americas Inc., 2007).

Specifically, the model was developed with specified-flux recharge conditions at the ground surface (calibration parameters), no flow at the bottom of the model, and seep/phreatophyte discharge at local topographic lows. A regional-scale groundwater flow model supplies constant-head boundary conditions to the lateral model faces (AquaResource Inc. and MWH Americas Inc., 2007). The model solves the steady-state flow equation. Although never truly a steady-state system, major groundwater pumping in and around Area IV largely ceased prior to 2009 but only data collected from 1995 to 1998 were used to calibrate that model. In this model update, only data collected since 2009 were used for calibration. Transient model runs were also performed for comparison to historical pumping data. The installation of monitoring wells, production wells, and other instrumentation over the last 56 years in response to water supply and groundwater monitoring requirements at the SSFL facilitated development of a well-supported hydrogeological model.

2.2 Numerical Implementation

FEFLOW (DHI-WASY, 2012) was selected for numerical implementation of the SCM because it includes modules for (AquaResource Inc. and MWH Americas Inc., 2007):

- Groundwater discharge zones (seeps) irregularly distributed along the slopes of the Simi Hills;

- Multiple formations, including steep changes in topography;
- Folded geologic layers with variable dips that are discontinuous in places;
- Directional hydraulic conductivity aligned with the dipping beds;
- Irregular distribution of faults with variable properties; and
- Irregular distribution of pumping and other anthropogenic influences.

FEFLOW uses the FEM to solve the groundwater flow equations (conservation of mass or continuity in saturated and unsaturated media) and hence can be based on an unstructured mesh that captures the complex stratigraphy at the SSFL. Specific advantages include (AquaResource Inc. and MWH Americas Inc., 2007):

- An ability for local mesh refinement to focus on specific points of interest or to more precisely simulate observed physical features (faults, pumping wells, seepage locations, etc.) and naturally complex boundary conditions;
- An ability of elements to conform to the pronounced vertical variation of aquifer/aquitard layers;
- An ability to align principal directions of hydraulic conductivity with bedding planes, which is believed to be an important control on groundwater flow at the SSFL; and
- Advanced boundary conditions (constrained seeps) to avoid non-physical boundary conditions.

In addition, the new Algebraic Multigrid Method for Systems (SAMG) solver (Thum et al., 2011) allows for solution of a 39-layer steady-state model with 11,484,498 elements and 5,904,845 nodes in about five minutes on 36 2.3-GHz cores. Such computational efficiency affords an ability to calibrate the model using the automated parameter estimation software, PEST (Doherty, 2016a, b). Also, larger contrasts in hydraulic conductivity are allowed in FEMs when the mesh aligns with stratigraphic formations. Although FEFLOW allows for discrete-fracture modeling, the computationally efficient equivalent porous medium approach was used because evidence from the SSFL site indicates a generally well-interconnected fracture network.

2.3 Updates from Run 22 to Run 55

2.3.1 Background

In December 2009, a Draft Site-Wide Groundwater Remedial Investigation Report (RI Report) for Santa Susana Field Laboratory (SSFL) was submitted to the California Department of Toxic Substances Control (DTSC) (MWH, 2009). The report included three-dimensional groundwater flow system analyses based on the Mountain Scale Groundwater Flow Model (MSGFM) developed using FEFLOW representing the Site Conceptual Model (SCM) for groundwater flow (Run 22). DTSC provided written comments on the Draft RI Report including the modeling work in a document dated December 21, 2011 (Malinowski, 2011).

A series of MSGFM runs were conducted between 2009 and 2015 to assess various potential modifications of the model (Runs 22 to 55). Note that Run 55 of the model was the starting point for further updates to the MSGFM performed by DOE in support of the Preliminary Draft Groundwater RFI Report Area IV. In August 2012, DTSC was presented with a summary of updates to the groundwater flow model that reflect refinements to the conceptual model and incorporated field data collected since the Draft RI Report was published in 2009. A Draft Work Plan was submitted to DTSC on May 17, 2013

proposing updates to the MSGFM to address DTSC comments, incorporate new field data and analysis, and update model analysis of flow directions and Darcy flux. The DTSC provided comments on and contingent approval of the Draft Work Plan in their September 17, 2013 letter. Nearly two years later on September 9, The Boeing Company (2015) sent a memo outlining the proposed responses to DTSC comments and included a thorough description of the proposed updates to the MSGFM. Those updates that were implemented in Run 55 of the MSGFM are summarized and reviewed here.

The purpose of the flow modeling was to represent the three-dimensional groundwater flow directions and Darcy fluxes to support characterization of the nature and extent of contamination at SSFL. Specifically, this support would include an evaluation of the suitability of the existing monitoring network and identify potential locations for any additional monitoring based on the predicted flow directions and Darcy fluxes under a variety of flow conditions (historic, current, future).

DOE further updated the MSGFM to focus on Area IV (James et al., 2017), building on Run 55 of the model. The purpose of this update was to facilitate fate and transport simulations for specific contaminant plumes in Area IV with measured chlorinated solvent and/or radionuclide concentrations. This allows for an evaluation for the potential of monitored natural attenuation while also helping to identify well-placement locations to maximize the potential for plume monitoring and interception. This MSGFM update emphasized matching groundwater observations in and near Area IV, relative to other locations at SSFL. Specific changes to the MSGFM from Run 22 to Run 55 are summarized below and some of the related updates supporting this report are briefly described.

2.3.2 Lowering the Depth to the Bottom, No-flow Boundary

The base of the MSGFM was lowered from sea level to 600 m below sea level, which is consistent with the inferred saltwater interface indicated by the Bob Hope oil and gas well drilled west of the site. The 2009 model had 39 layers, and this was increased to 53 layers to accommodate the deeper bottom boundary. The number of nodes was increased from about 3M to about 13.5M.

2.3.3 Incorporation of Adjustable Hydraulic Conductivity Decrease with Depth

Consistent with what is observed in nature, a decrease in hydraulic conductivity with depth (depth decay) was added to the model as an adjustable parameter during calibration. DTSC and the Boeing Expert Panel felt that it was important to calibrate the strength of depth decay so that it was not arbitrarily specified using a generally accepted textbook value. Additional conceptual models are under consideration by Boeing in which depth decay is not considered at all.

2.3.4 Update to Recharge and Recharge-zone Parameterization

Additional recharge zones were added to better represent local conditions, variability, and a wider range of recharge. Moreover, because spurious groundwater mounding was observed in some locations, the upper layers of the model were adjusted to incorporate a discrete weathered bedrock zone of higher hydraulic conductivity underlying alluvium, which was discretized into three distinct model layers. The upper weathered zone is not linked to the depth decay of hydraulic conductivity. DOE further updated the recharge zones and alluvial thickness in Area IV (James et al., 2017, Section 2.3.4)

2.3.5 Updated Fault Zones and Parameterization

Responses to DTSC comments as discussed in the August 2012 meetings, and results of the field work completed as part of the Data Gap SAP implementation suggested updates to fault locations. However, it

was agreed that representing faults as vertical features in the flow model, even though they are known to dip at high angles, is appropriate if observation locations in the model, such as wells, are positioned on the appropriate side of the faults. Structural updates based on the field work completed since 2009 were incorporated into the revised model structure along with the deeper model base. Refinements to the fault locations and modeled observation locations were made. Additional parallel splays were added to the North Fault and its trace was extended further west. Between North Fault traces, additional parameter zones were added. Two adjacent disturbed-rock zones were added around the North and Happy Valley Faults to increase parameter variation during calibration and improve the fit of simulated head to observed head measurements. Wells RD-51 and RD-56 were moved from the south to the north of the southern trace of the North Fault because all faults in the model are assumed vertical and the water levels were measured north of the fault when considering dip. Although additional parameterization was added to the FSDF Structure, this feature was replaced with a zone of anisotropy in the DOE update (James et al., 2017, Section 2.3.7). The most recent site fault map does not include a western extension of the North Fault to intersect the Burro Flats Fault; however, a corresponding zone of deformation banding and probable reduced hydraulic conductivity was included in the DOE update to the flow model.

2.3.6 Updated Data Used for Calibration

Additional observation data collected between 2009 and 2013 were added to the calibration data set to ensure better representation of steady-state conditions and improved spatial coverage in Run 55 of the MSGFM. Additional multi-level head measurements were included so that calibration would more accurately reflect vertical gradients observed at the site. Finally, the MSGFM was updated to explicitly consider the heads measured in long, open wells. Note that the DOE update only used data collected from 2009 through 2016 to reflect the conditions closer to steady state (James et al., 2017, p. 19). Although data weighting during calibration was updated from Run 29 to Run 55, further adjustments were made to weights by the DOE to specifically focus on Area IV (James et al., 2017, Section 3.2).

2.4 DOE Updated Model Data Inputs

2.4.1 Well Data from the Boeing Environmental Data Management System

The water-level data set used to calibrate the model was obtained from the Boeing Environmental Data Management System (BEDMS) through CDM Smith. The set contains groundwater elevations and well information from 1984 through 2016 for all the wells at the SSFL.

2.4.2 DOE Data from CDM Smith

Updated groundwater elevation data were obtained from CDM Smith for wells already existing in the Boeing dataset (PZ, RD, RS) and wells new to the Boeing dataset (DD, DS), all in or near Area IV. New water-level measurements were collected in January, February, April, and May of 2016 (only data from 2009 onward were used).

2.4.3 Updated Analysis of Alluvium Thickness

An analysis of the alluvium thickness in Area IV of the SSFL was carried out by Dr. Bill Arnold. Three data sources were used. The first was the CDM Smith database on soil thickness from soil sampling surveys in Area IV. The second was site-wide data on soil depth provided by Dr. Nicholas Johnson of MWH. One caveat with this set is that the source of the data was not known to Dr. Johnson, was used by him to estimate total soil volumes, and was not checked or validated by him. The third data source was

data from bedrock outcrops created by digitizing outcrop locations from satellite imagery. The locations of all alluvium-thickness measurements and bedrock outcrops are shown in Figure 1.

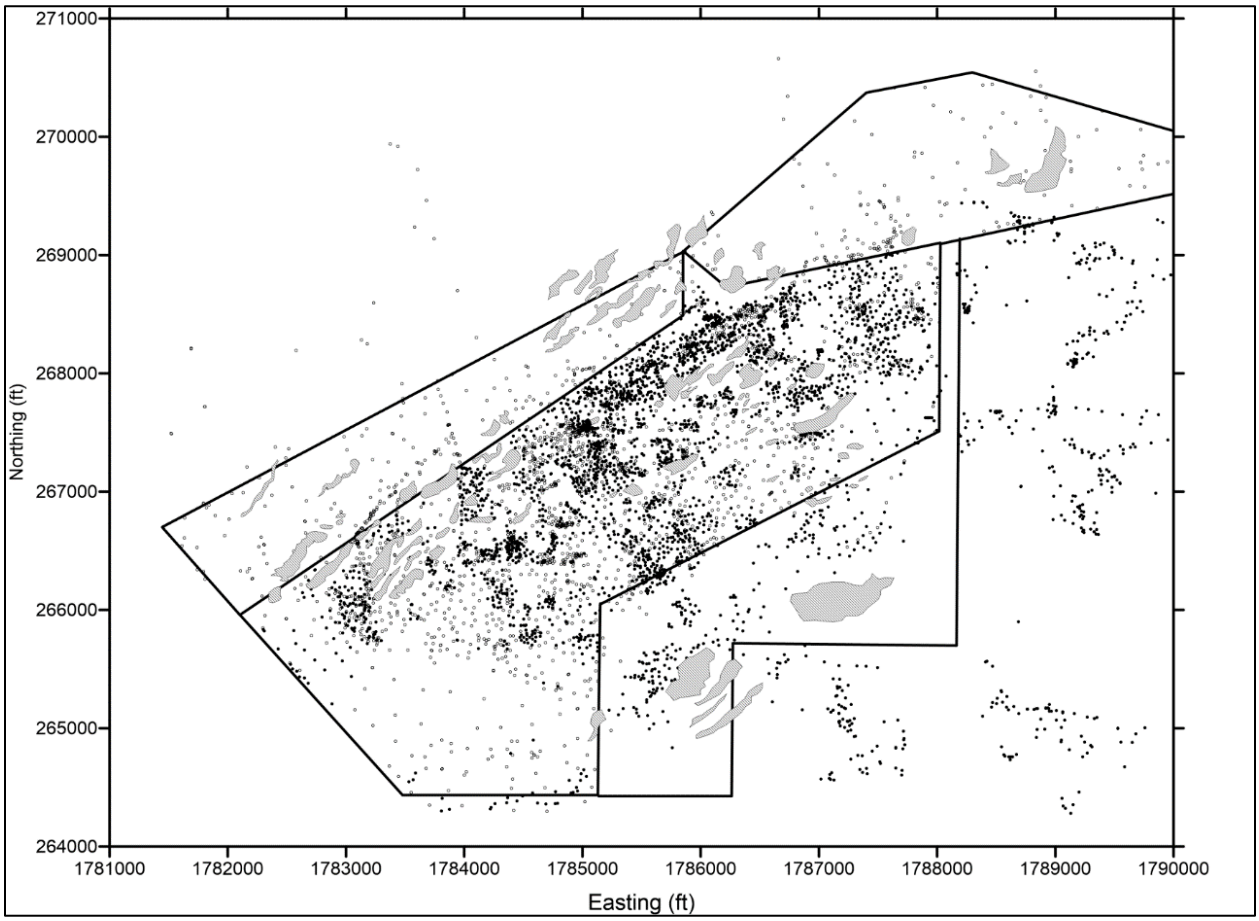

Figure 1: Location of alluvium thickness measurements and bedrock outcrops in and around Area IV. Locations of data from (Johnson, personal communication) are shown with black circles and from the CDM database are shown with gray circles. Bedrock outcrops are indicated by the irregular gray polygons.

A variogram analysis, shown in Figure 2, was used to estimate the spatial correlation characteristics of alluvium thickness. An anisotropic spherical model with a correlation length of 103.6 m (340 ft) and an anisotropy ratio of 1.5 was fit to the data at a resolution of 1.5 m (5 ft). The direction of maximum correlation is N35°E, which is parallel to the strike of the beds. In the analysis, there was a significant nugget effect (13), corresponding to over half of the semi-variance. The alluvium thickness was deterministically set to zero for locations corresponding to bedrock outcrops.

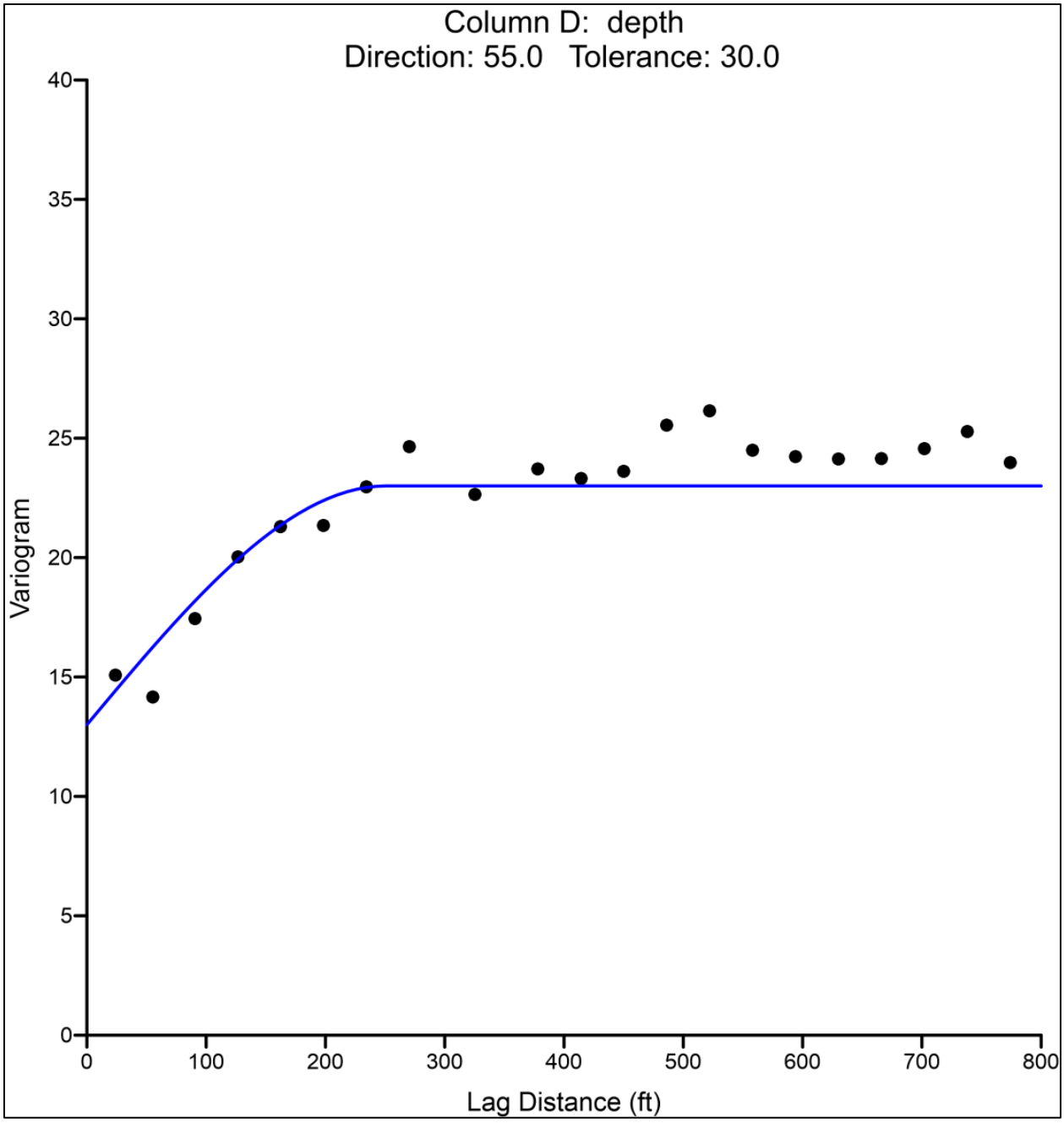

Figure 2: Anisotropic spherical variogram of alluvium thickness data in the NE-SW direction.

Kriging was used to estimate the spatial distribution of alluvium thickness in Area IV including a buffer zone around the area. Figure 3 is a contour plot of alluvium thickness based on the Kriging analysis.

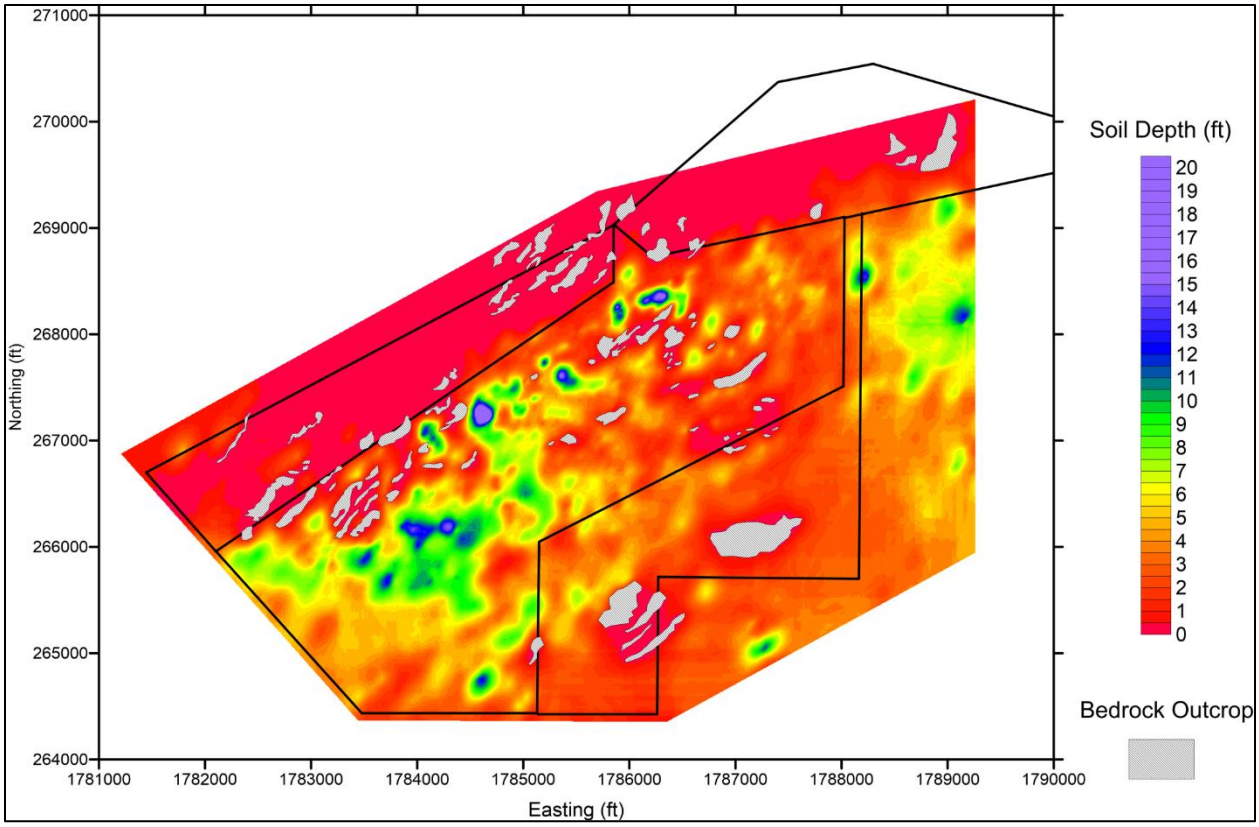

Figure 3: Kriged alluvium thickness in and around Area IV.

2.4.4 Assignment Convention for Updated Alluvium Thickness

In the FEFLOW model, each finite element is assigned a unique hydraulic conductivity "zone" corresponding to a stratigraphic unit or fault. These zones comprise the majority of calibration parameters and they are adjusted so that model simulations most closely correspond to site data. Because these hydraulic-conductivity zones reflect geologic materials, a change in alluvium thickness necessitated a change to the corresponding alluvium hydraulic conductivity zones in the model. Hence, the resulting updated alluvium thickness was discretized onto the FEFLOW finite element mesh. Specifically, the center of each finite element nearest to each Kriged alluvium thickness datum (on a 1.52×1.52 m^2 [5×5 ft^2] grid) was used to identify whether or not that cell was assigned as alluvium. The assignment convention is illustrated in Figure 4. For example, if the depth of the alluvium was between the midpoint of layer 3 and the midpoint of layer 4, then alluvium was assigned to the element in layer 3 and all elements above. If the updated alluvial thickness decreased, then the unit below the element was extended upward. In most locations, the unit below was weathered rock. The original alluvium distribution on the top layer of the model is shown in Figure 5. The alluvium distribution on the top layer of the model resulting from the analysis is shown in Figure 6. In general, the updated alluvium in Area IV was larger and thicker.

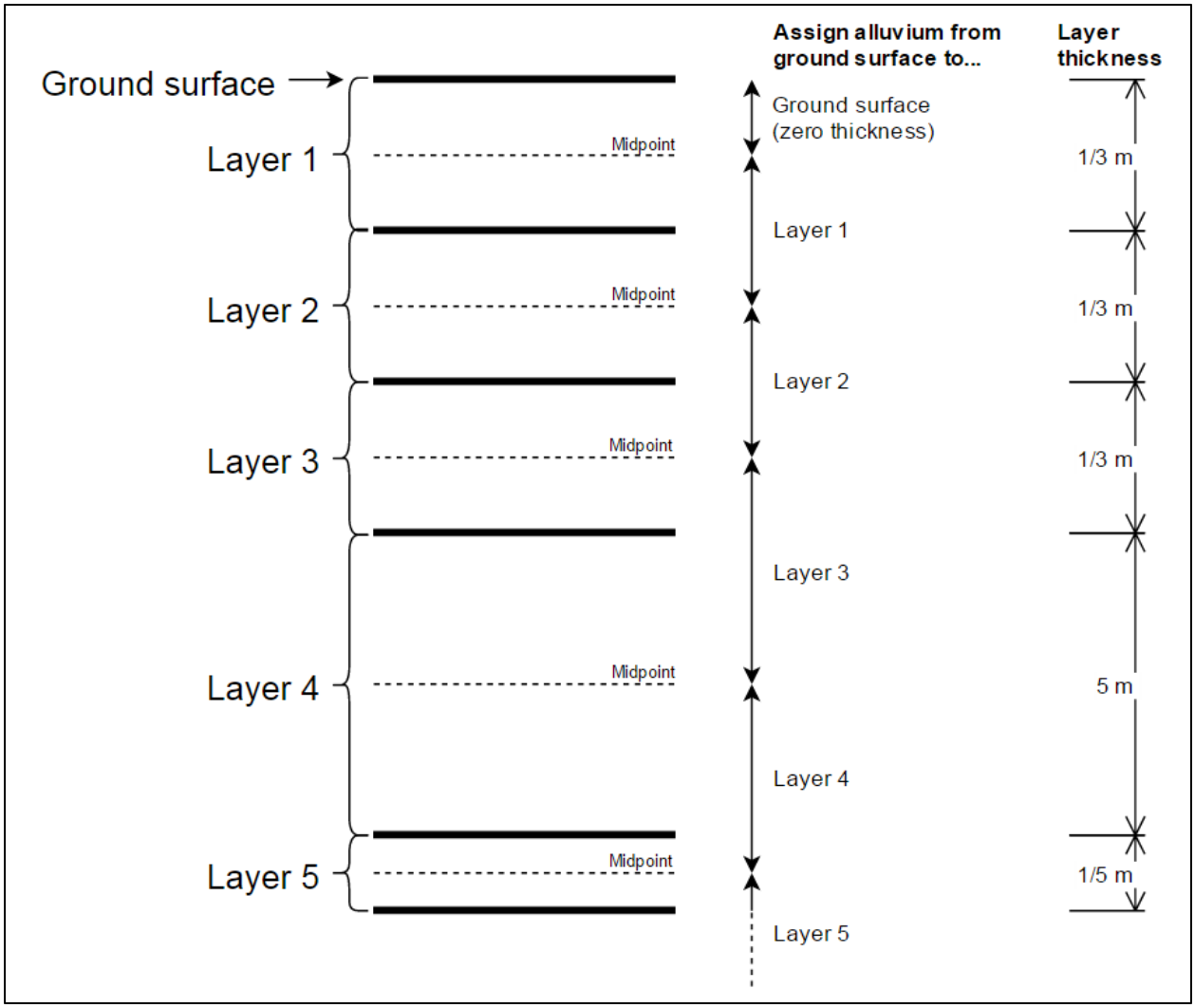

Figure 4: Convention used to update alluvium depth by specifying a finite element as alluvium or the unit below.

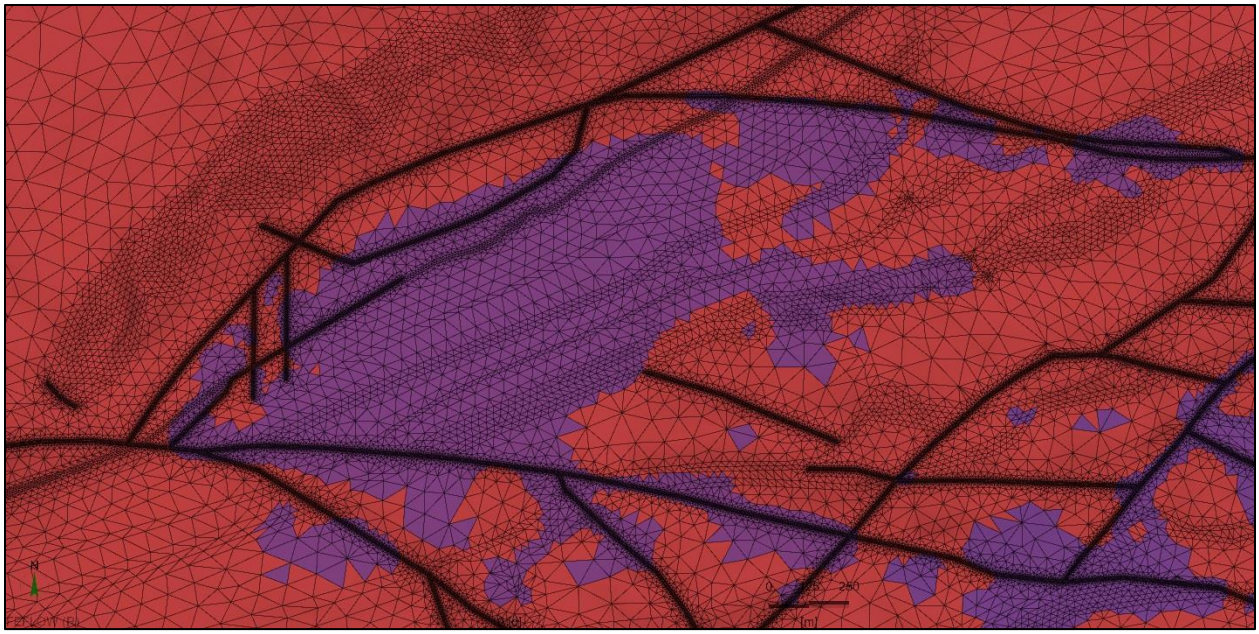

Figure 5: Previous Area IV alluvium distribution (alluvium is purple).

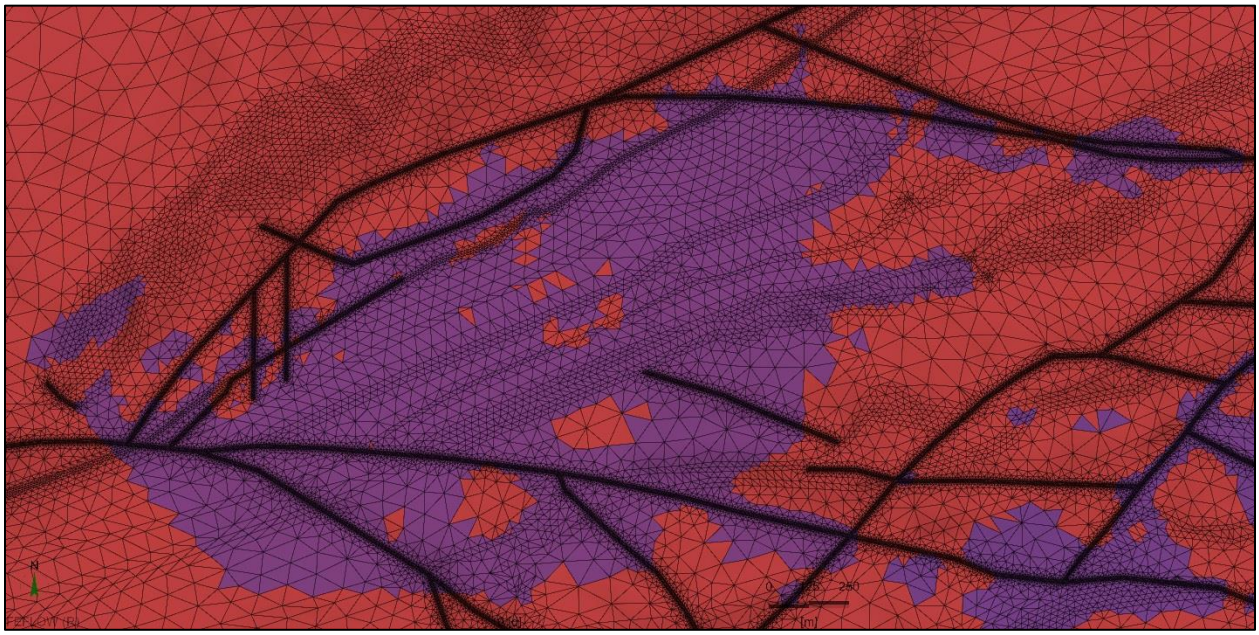

Figure 6: Updated Area IV alluvium distribution (alluvium is purple).

One additional change was made to the alluvium thickness in the region corresponding to a dredged portion of Area IV (MWH, 2013). The 36 purple model elements shown in Figure 7 for layers 1 through 11 were set to alluvium to correspond to the deeper backfill in this dredged area.

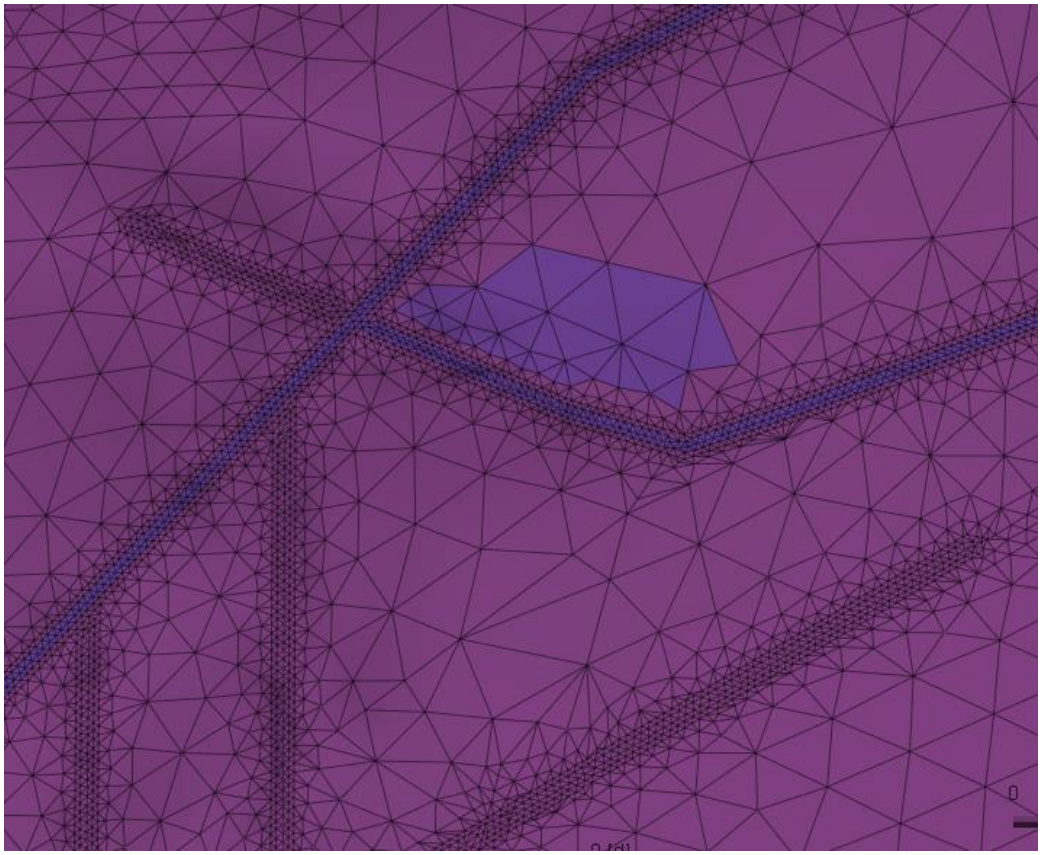

Figure 7: Portion of the Area IV alluvium that was deepened due to trenching activities.

2.4.5 Recharge Adjustment

In addition to hydraulic conductivity zones, recharge "classes" also comprised a calibration parameter group. These recharge classes were assigned to the elements in the top layer of the model and generally correspond to the hydrogeologic zone and sub-catchment. Each recharge class was independently calibrated because, for example, recharge would be quite different through a shale outcrop than through alluvium. Recharge class names are numeric (e.g., "1008000," which are all listed in the Appendix) and should not be confused with corresponding calibrated recharge class values, which are decimal multipliers of average annual precipitation. The recharge class assignments on the alluvium of Area IV were based on designated "sub-catchments" in the alluvium. The original alluvial recharge class distribution in the model is shown in Figure 8 for the west portion of Area IV while Figure 10 shows the eastern portion. Because the alluvium distribution changed with the update, the distribution of the alluvial recharge classes had to be updated correspondingly. The recharge classes, differentiated by color, are shown in Figure 9 for western Area IV and in Figure 11 for eastern Area IV. Recharge class 1008000 was created in western Area IV due to a newly defined large alluvium patch. Figure 12 and Figure 13 show the composite recharge class distributions over all Area IV alluvium before and after the model update.

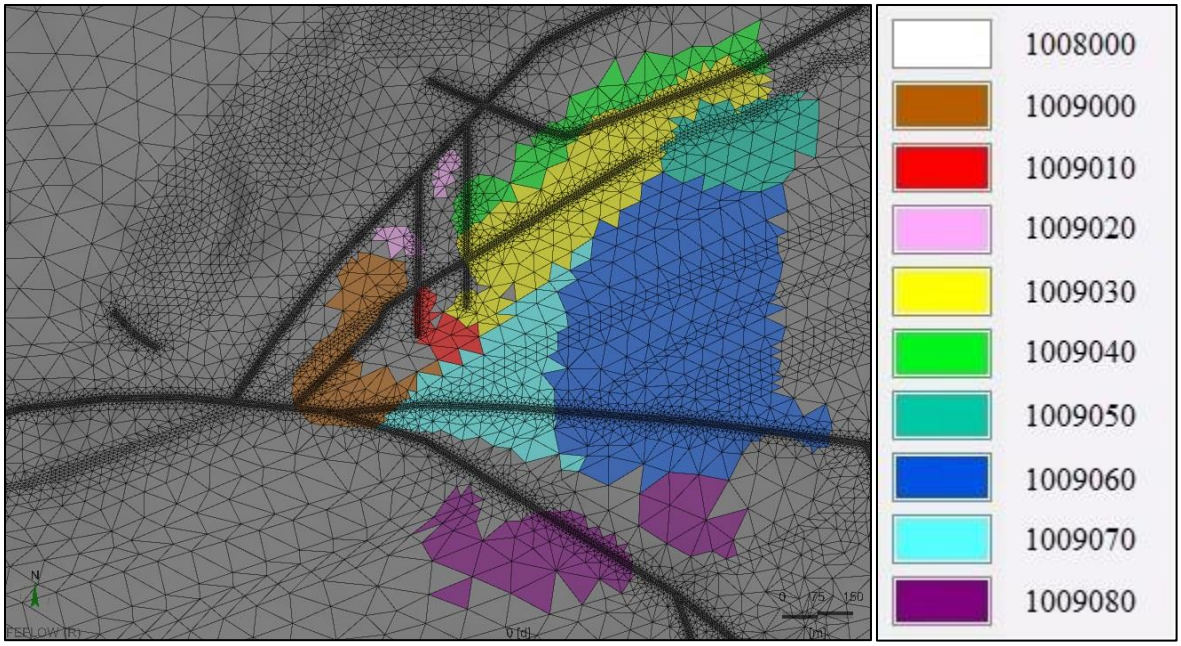

Figure 8: Previous western Area IV alluvial recharge class distribution. (Note: recharge class 1008000 is not in the original distribution.)

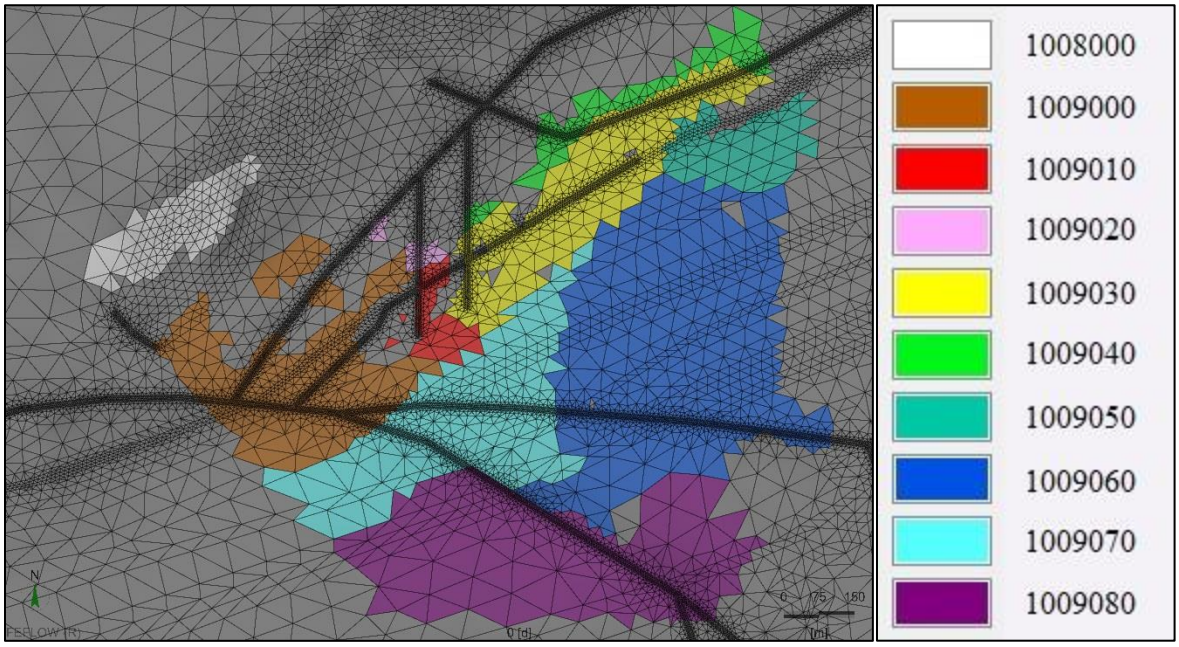

Figure 9: Updated western Area IV alluvial recharge class distribution. (Note: recharge class 1008000 has been added to the distribution.)

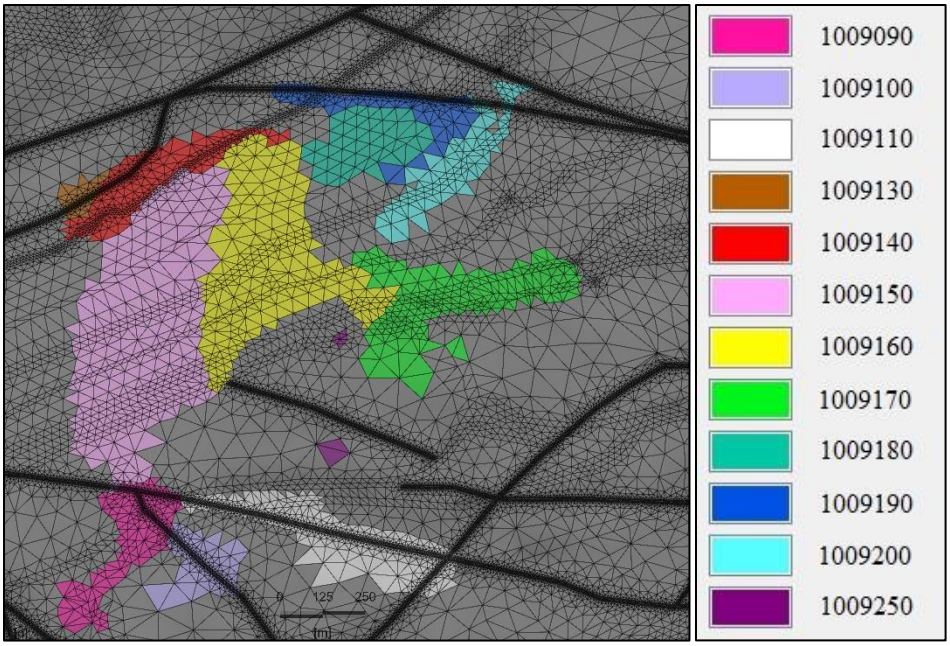

Figure 10: Previous eastern Area IV alluvial recharge class distribution.

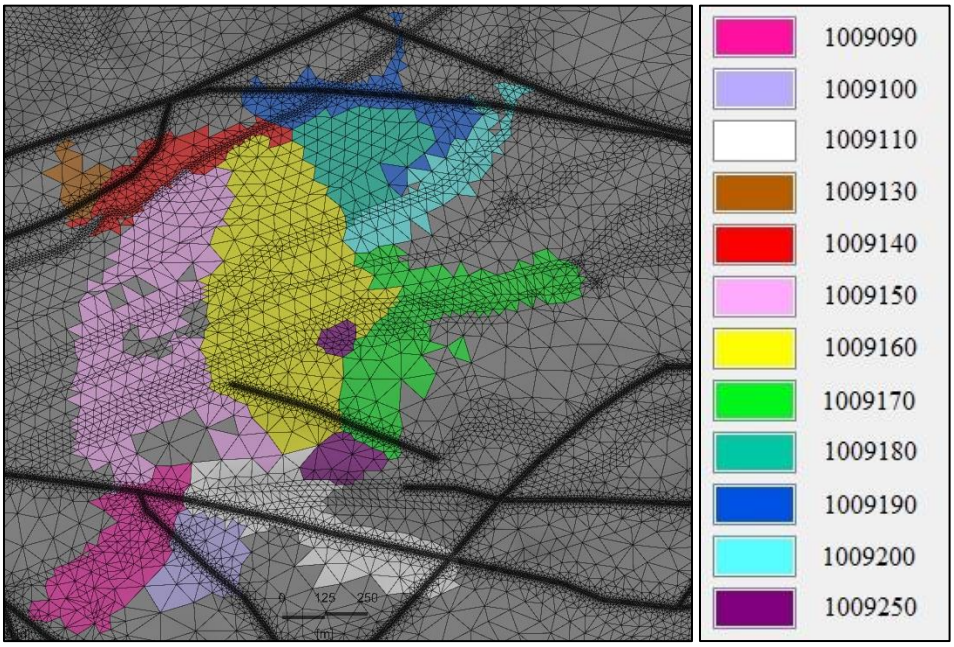

Figure 11: Updated eastern Area IV alluvial recharge class distribution.

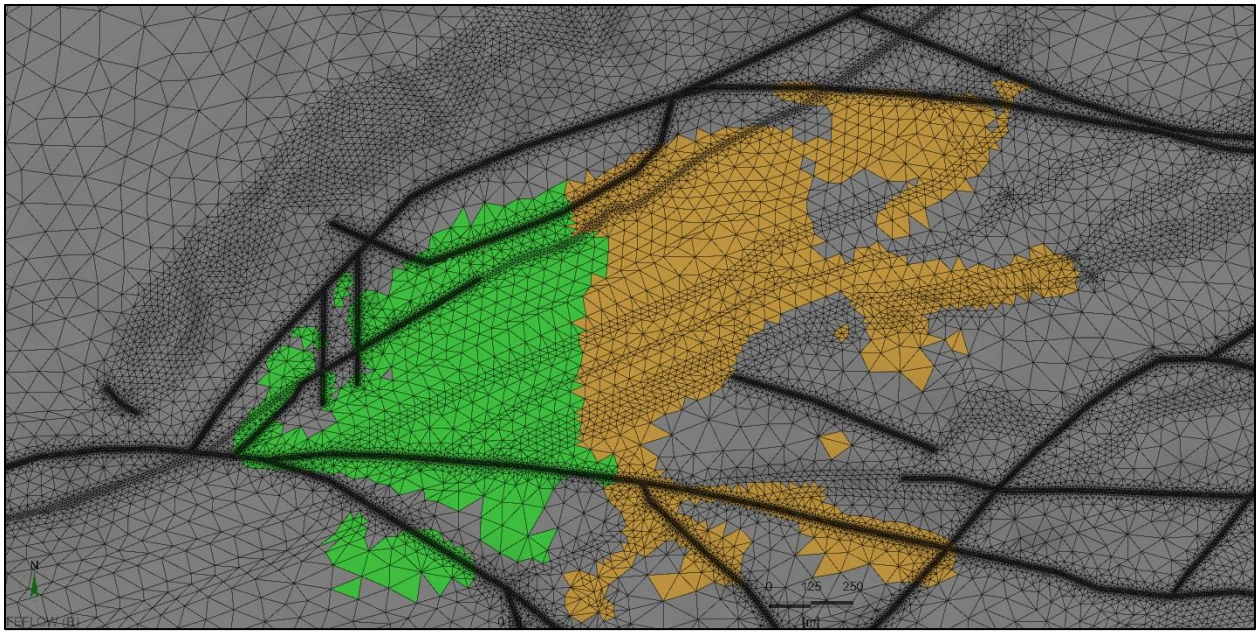

Figure 12: Previous Area IV alluvial recharge class. Green represents recharge classes from Figure 8 (east); orange represents recharge classes from Figure 10 (west).

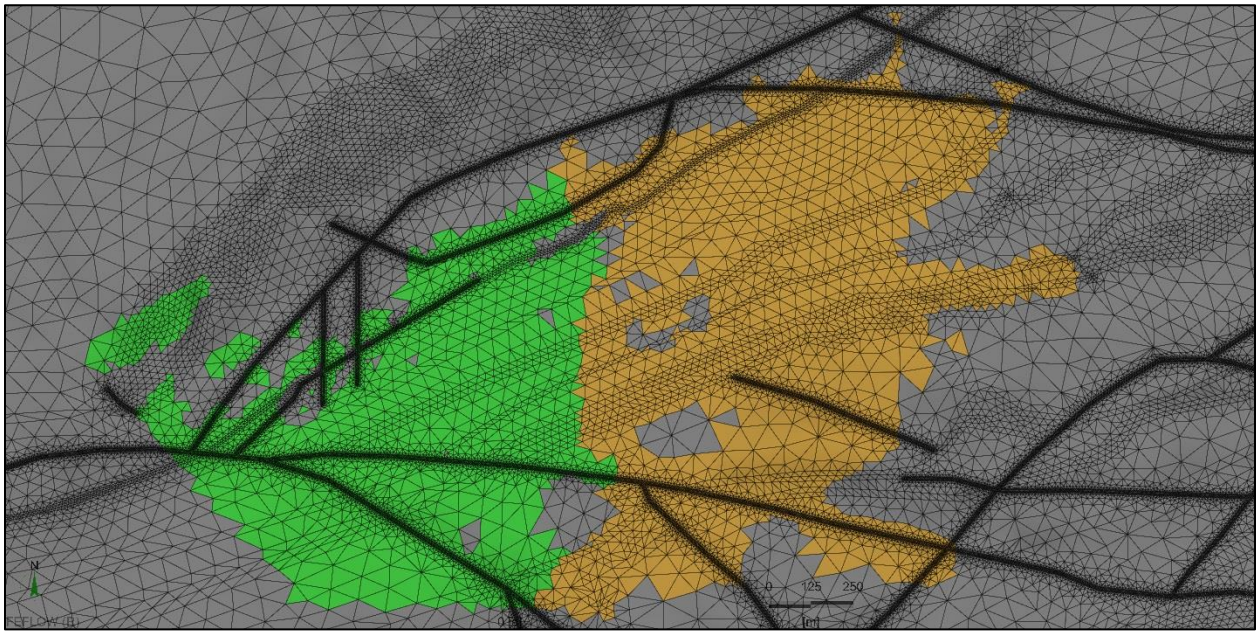

Figure 13: Updated Area IV alluvial recharge class distribution. Green represents recharge classes from Figure 9 (east); orange represents recharge classes from Figure 11 (west).

2.4.6 Removal of Selected Faults and Features

Three additional changes were made to assignments of hydraulic conductivity zones in the model in Area IV to make the model more consistent with the latest understanding of site geology. In all cases, the hydraulic conductivity zone identifiers were set equal to those in the region immediately surrounding the

feature that was removed from the model. Because hydraulic conductivities vary from layer to layer, this assignment of the feature's hydraulic conductivity was performed on a layer-by-layer basis.

First, the portion of the SRE/RMHF Lineament that traverses the North Fault was removed (hydraulic conductivities set equal to those of the background geologic unit for each layer). The red oval in Figure 14 indicates the portion of the SRE/RMHF Lineament that was removed from the model.

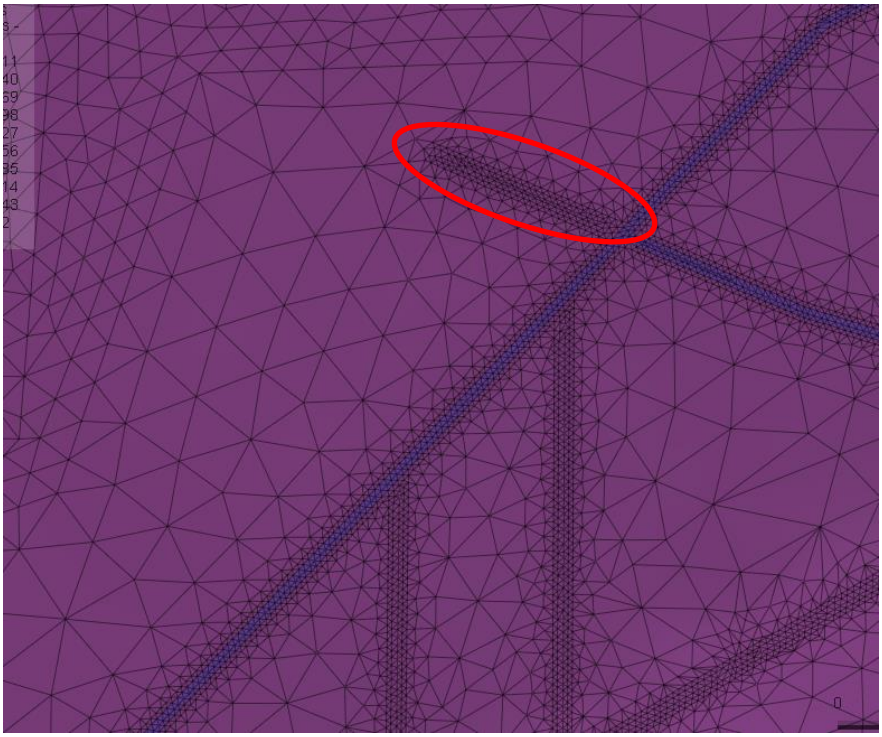

Figure 14: Portion of the SRE/RMHF Lineament that was removed from the model by setting its hydraulic conductivities to those in the background layer by layer as indicated by the red oval.

Second, the fault feature north of the Burro Flats Fault and west of the North Fault in Area IV was similarly removed by setting the hydraulic conductivities of each layer to that of the surrounding geologic units.

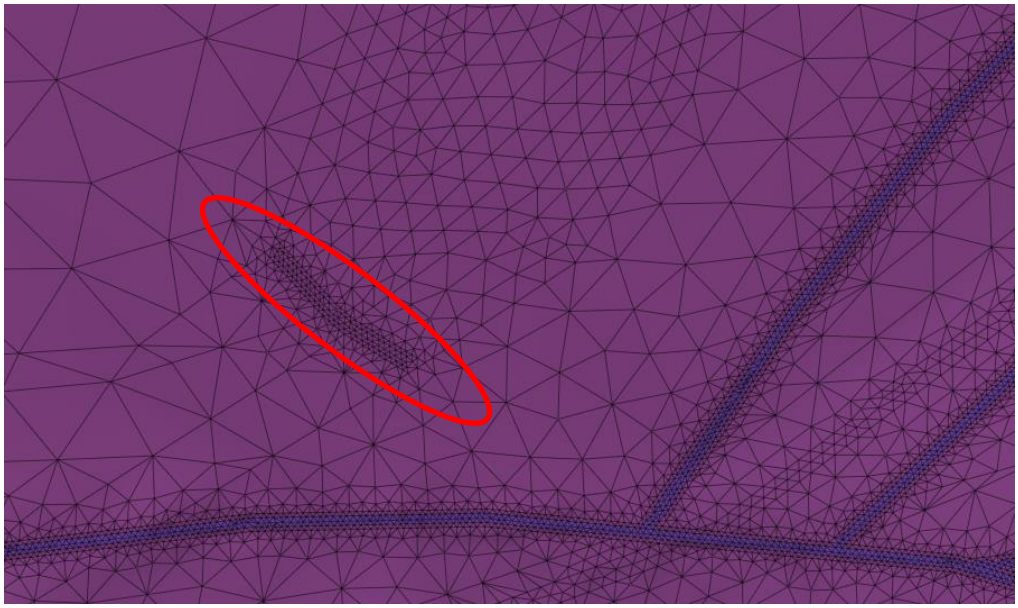

Figure 15: Fault feature that was removed from the model by setting its hydraulic conductivities to those in the background layer-by-layer, as indicated by the red oval.

Finally, the FSDF Structures were treated similarly and removed from the model. Note that the Lot Bed intersects these FSDF Structures. North of the Lot Bed, the hydraulic conductivities of the FSDF Structures were set equal to those of the geologic unit between the Structures (layer by layer). South of the Lot Bed, hydraulic conductivities were set to those of the surrounding geologic units.

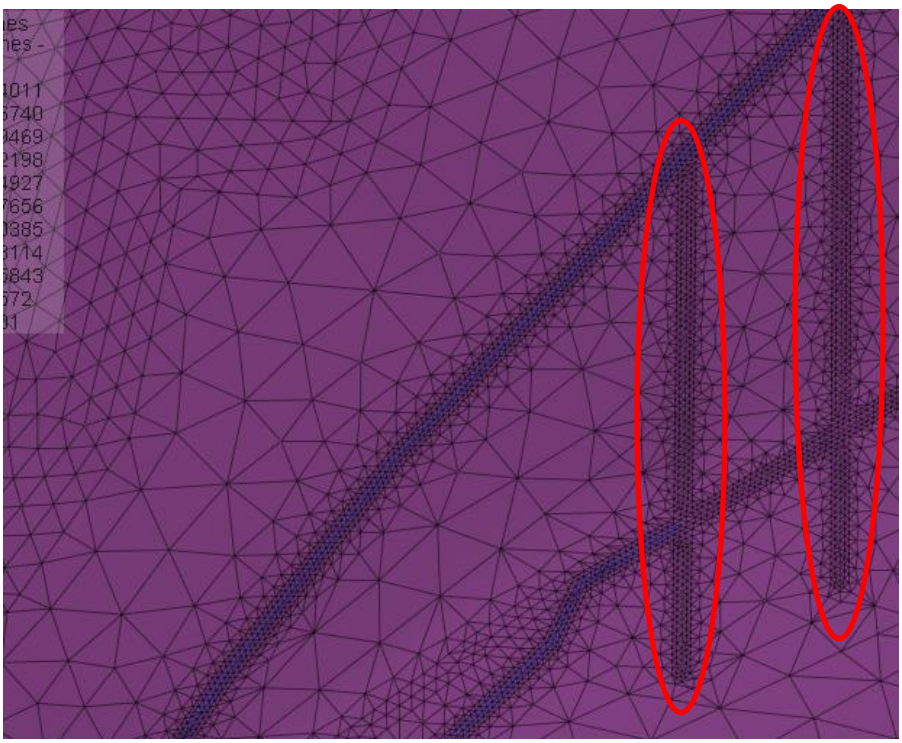

Figure 16: FSDF Structures removed from the model by setting their hydraulic conductivities to those in the background layer-by-layer, as indicated by the red ovals.

2.4.7 Introduction of Anisotropy

The geologic mapping and excavations along the western and eastern FSDF Structures revealed intensely fractured rock from below the alluvium to perhaps 102 m (335 ft) below ground surface (MWH, 2013). These fractures trended in a northeast to southwest direction. To represent this conceptual model in FEFLOW, a zone of horizontal anisotropy was established in Area IV in the wedge-shaped region between the intersection of the Burro Flats Fault and the north Fault that extends through the former FSDF Structures and up to the SRE/RMHF Lineament. To effect this change, layers 5 through 13 in the region outline by the red polygon in Figure 17 were assigned a southwest to northeast trending horizontal anisotropy. Colors in this figure represent the Euler angles, which were set to −135° within the polygon. Outside of the polygon, FEFLOW automatically generated Euler angles to correspond to layer angles (parallel to dip and strike).

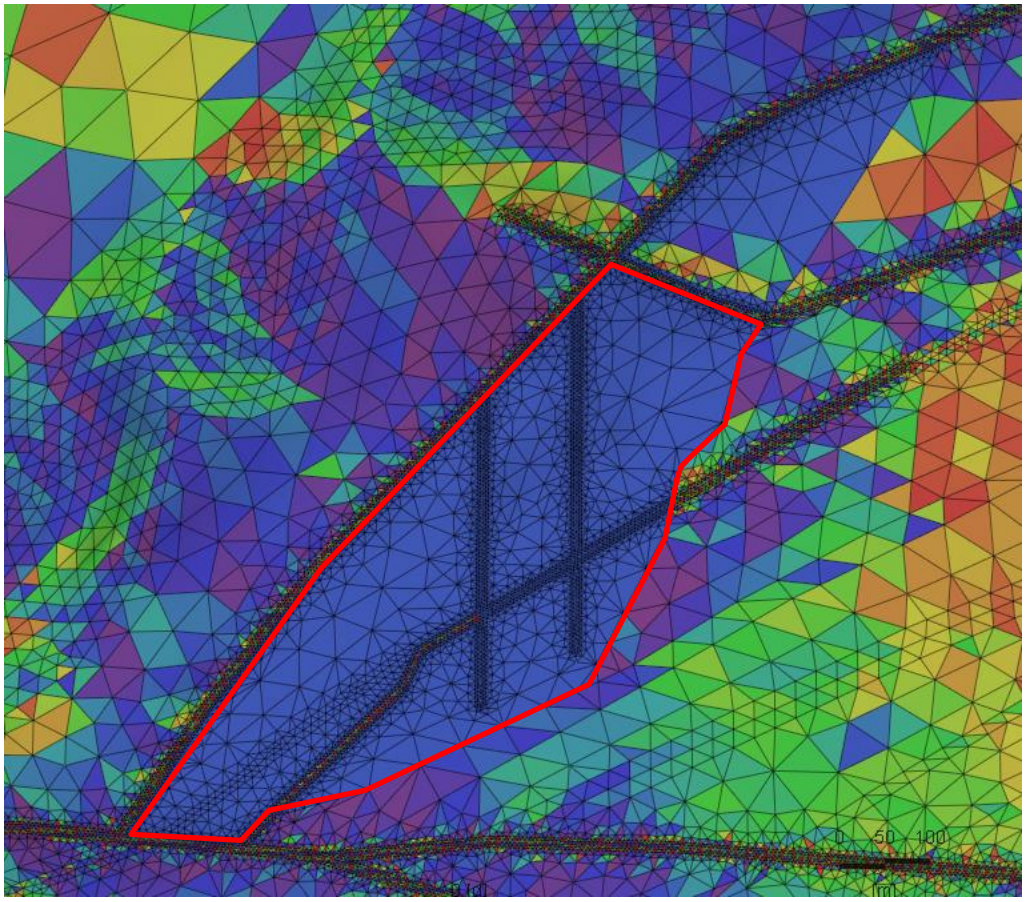

Figure 17: Euler angles for model elements. Within the region outlined by the red polygon, the Euler angle was set to −135° to represent the southwest-northeast trending anisotropy aligned with observed fractures.

2.4.8 Unsaturated Flow Model Update

Since Run 55, the effective saturation in the model was updated by Matrix Solutions (but not documented) according to the Modified van Genuchten model (Schaap and van Genuchten, 2006; van Genuchten, 1980):

$$S_e = \frac{S - S_r}{S_s - S_r} = \begin{cases} \left[1 + (-\alpha\psi)^n\right]^{-m} & \psi < 0 \\ 1 & \psi \geq 0 \end{cases}, \quad (1)$$

$$K_r = s_e^{\delta}, \quad (2)$$

$$\alpha > 0 \quad m > 0 \quad n > 0,$$

with parameters defined in Table 1. This update minimizes the potential for the calibration model to return water levels that are above the ground surface.

Table 1: Unsaturated zone parameters.

Parameter name	Symbol	Value	Units
Effective saturation	S_e	Dependent	Fluid volume per void volume
Saturation	S	Independent	Fluid volume per void volume
Residual saturation	S_r	0.315946	Fluid volume per void volume
Maximum saturation	S_s	1	Fluid volume per void volume
Fitting parameter	α	0.311097	m^{-1}
Pressure head	ψ	Independent	m
Fitting parameter	n	1.42359	–
Fitting parameter	m	0.29751	–
Relative conductivity	K_r	Dependent	–
Fitting parameter	δ	0.553428	–

2.5 Observations Used in Model Calibration

2.5.1 Water Levels in Wells

2.5.1.1 Well Measurement Elevation Convention

The convention used to specify the measurement elevation (*z*-location) where model heads are extracted from FEFLOW for comparison to site data during calibration is shown in Figure 18. If the groundwater elevation was above the screen of the well, the measurement elevation was designated as the midpoint of the screen top and bottom. If the groundwater elevation was within the screen of the well, the measurement elevation was designated as the midpoint of the screen bottom and groundwater level. Several wells had no screen data and were hence assigned zero weight and not considered in the calibration. These were C-1, C-3, C-7, C-10-01, C-18-02, PZ-006B, RD-101-1, RD-101-4, RD-101-5, RD-101-9, and RD-35C-1 through RD-35C-9.

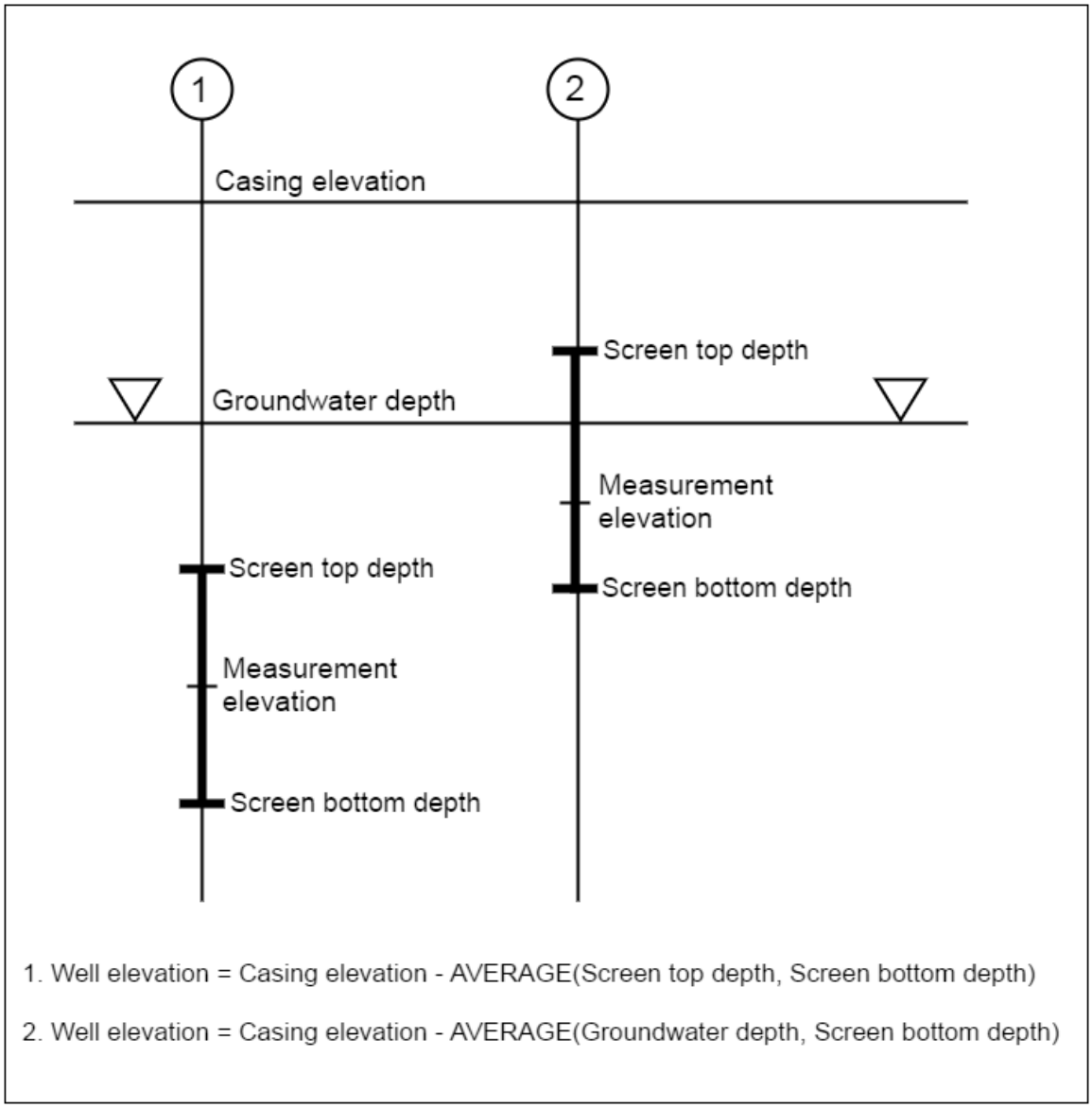

Figure 18: Convention used to assign a z-location to a head measurement.

2.5.1.2 Data Date Restriction

No data prior to January 1st, 2009 were considered when calculating heads, gradients, and initial calibration weights. This date was selected to represent a fairly steady-state period for SSFL because up through 2008, a total of 1,761,800,700 gallons were pumped while only 10,637,797 were pumped from October 26th, 2009 to May 14th of 2013 from well WS-09A (a factor of 165 less). While WS-09A is within 610 m (2,000 ft) of the nearest boundary of Area IV, it is on the other side of the Area IV groundwater divide and pumping this well should have minimal impact on Area IV groundwater levels. Groundwater pump and treat operations were deactivated in March 2001 for Alfa, in May 2002 for Bravo, in August 2007 for Delta, in September 2000 for Area I-Rd. ASU, in October 2000 for WS-05, and in February 2003 for STL-IV, all sufficiently before 2009 to support the steady-state assumption.

2.5.1.3 Heads

Head observations at wells were calculated as the average of the water-level measurements taken since 2009. Variability in these measurements was considered in the weighting scheme (i.e., an increased variability yielded a decreased weight by setting it to the inverse of the standard deviation). The head (water-level) observations were classified into eight groups listed in Table 2 with a group importance factor assigned to each. This group importance factor assured that appropriate PEST weighting was maintained as calibration iterations proceeded. Without this importance factor, the objective function (sum of weighted squared differences between measurements and observations) for each group would diverge as calibrations proceed potentially allowing less important head observations (e.g., perched water levels) to play a more important role in the calibration.

Table 2: Water-level groups.

Group name	Designation	Importance factor
*heads*1	Perched wells, never dry	0.1
*heads*2	Intermittently dry wells	0.5
*heads*3	Chatsworth discrete member monitor	20
*heads*4	Chatsworth blended member monitor	1
*heads*5	FLUTes	5
*heads*6	Westbays	20
*heads*7	Area IV	40

Specifically, observations in *heads*1 are suspected perched wells that have never been reported dry. Observations in *heads*2 are for intermittently dry wells. Both have low importance factors indicating that PEST was not strongly directed to replicate these observations. Observations in *heads*3 are from wells interrogating only a single non-dry unit, and observations in *heads*4 are from wells that blend water levels from more than one non-dry unit. Multilevel wells are in *heads*5 if they are FLUTe wells or *heads*6 if they are Westbay wells. Observations were placed in these last two groups so long as they did not satisfy the requirements to be in other heads groups first. The observations in *heads*7 are of specific interest when modeling Area IV. Observations were placed in *heads*7 if they are DD or DS wells, which were measured in 2016 and are located within Area IV or the Northwest Buffer Zone. Observations were also placed in *heads*7 if those wells are in or within 1 km of Area IV and if they would have been classified in *heads*3 or *heads*6. Other head groups were not included because perched and intermittently dry wells were not to be heavily weighted. In summary, head groups were weighted differently with low weights assigned to perched and intermittently dry wells (*heads*1 and *heads*2), higher weights to multilevel wells (*heads*5 and *heads*6), and the highest weights to Area IV wells (*heads*7). It is noted that some hand adjustments were made to weights that, in the modeler's best professional judgment, were important to constraining flow paths from wells with known contamination where particle tracks were subsequently initiated. Specifically, the weight on the head measurement for RD-94 was increased by a factor of three while water levels in RD-22, RD-50, RD-65, RD-150, RD-156, and DD-140 had their weights increased by a factor of two.

2.5.2 Gradients in Head

Gradient observations between specific wells were calculated as the average of the head difference measurements for a pair of wells selected to straddle stratigraphic units and faults. Using head differences as calibration targets allows PEST to specifically identify the confining unit or fault that establishes the

gradient. Head differences were calculated four times per year (quarterly) when such a pair of measurements was available. Variability in these measurements was also considered in the weighting scheme (details below). The gradient (head difference) observations were classified into six groups listed in Table 3.

Table 3: Head difference groups.

Group name	Designation	Importance factor
*grads*11	Across shale	5
*grads*12	Along/across faults	5
*grads*14	FLUTe/Westbay – head change interval	2.5
*grads*15	Well nests	5
*grads*16	Uniform sage member	5
*grads*17	Area IV	10

Gradients were typically assigned an importance factor of 5, except for FLUTes/Westbays (2.5 because these heads were also specifically considered in *heads*6 and *heads*7) and Area IV (10). The gradient observations in *grads*17 are of specific relevance to Area IV and have at least one well of the pair located in Area IV.

2.5.3 Groundwater Seeps and Phreatophytes

The total flows (m^3/day) from seep and phreatophyte in specific watersheds were retained as observation values from the PEST55 analysis. Variability in these values was considered in the weighing scheme. Seep and phreatophyte flow observations were classified into two groups, listed in Table 4.

Table 4: Seeps and phreatophytes groups.

Group name	Designation	Importance factor
*seeps*18	Seeps and phreatophytes (non-Area IV)	8
*seeps*19	Seeps and phreatophytes (Area IV)	16

The seep and phreatophyte flows in *seeps*19 are the two seeps downgradient (northwest) of Area IV (i.e., Meier Canyon A2 and Meier Canyon B) and these were given twice the importance factor of the remaining seeps.

2.5.4 Flow Ratios

The three seep-ratio observations are the ratios of seep and phreatophyte flows in west to those in the north, south, and east sub-domains of the model. Using seep ratios as calibration targets ensures that the general flow patterns at the SSFL were honored and to avoid too much flow exiting any one side of the model. Seep-ratio observations were classified into one observation group in PEST and were assigned an importance factor of 5

3. Groundwater Model Calibration

3.1 Parameter-estimation Method

Modeling is routine in environmental-management investigations, especially at sites where heavy investment may follow important decisions. Models provide the bridge between our understanding of

environmental processes formulated through mathematical descriptors, such as Darcy's law, and predictions of system behavior, perhaps subject to remediation efforts. In doing this, they provide important decision-making support.

Models serve another important role in environmental management—a role that is often insufficiently recognized. Specifically, this role is to process all available site data, both hard and soft. Examples of such data include qualitative impressions of the disposition of geological layering supported by borehole intersections at a small number of locations, geophysical data, point measurements of hydraulic properties, historical measurements of system state at different locations, geochemical inference, and so on. A good model will extract maximum information content from site data during the calibration process while also reproducing historical site measurements. This leads to:

1. Predictions of future system behavior with decreased uncertainty,
2. The ability to quantify uncertainty,
3. The ability to examine the contribution of dataset members in reducing uncertainty to its current level,
4. The ability to quantify contributions to uncertainty from model parameterization, and
5. The ability to quantify how additional data-collection activities could reduce model predictive uncertainty.

Where a modeling exercise addresses all of the issues listed above, it is indeed paying returns on the investment of model development. For this to be accomplished, however, the model must be used in conjunction with appropriate parameter-estimation and uncertainty-analysis software that maximizes the potential of the model in relation to the goals listed. It is the authors' contention that the use of such software in conjunction with complex, site-specific models should be viewed as an indispensable component of model-based decision making and management.

PEST (Parameter ESTimation) (Doherty, 2016a, b) was used to calibrate the FEFLOW parameters including hydraulic conductivities (716 independent parameters), recharge classes (46 parameters), vertical anisotropy ratios (61 independent parameters with the rest of the 481 total parameters tied), and hydraulic-conductivity depth decay (one parameter). PEST conducts gradient-based, nonlinear parameter estimation, based on the Gauss-Marquardt-Levenberg algorithm, and adjusts model parameters to minimize the weighted, least-squares objective function. PEST has also been extensively applied for uncertainty assessments and sensitivity analyses (Doherty, 2015; Doherty and Hunt, 2009; Doherty et al., 2011; Gallagher and Doherty, 2006; James et al., 2009; Moore and Doherty, 2006; Moore et al., 2010; Tonkin and Doherty, 2005; Tonkin et al., 2007; White et al., 2016).

3.2 Objective Function

The objective function is defined as the weighted sum-of-squared-differences between the measured and simulated water levels (613 observations), head gradients (219 observations), seep and phreatophyte flows (36 observations), and flow ratios (3 observations):

$$\Phi = \sum_{i=1}^{613} w_i \left(h_{\text{sim}} - h_{\text{meas}} \right)_i^2 + \sum_{j=1}^{219} w_j \left(\Delta h_{\text{sim}} - \Delta h_{\text{meas}} \right)_j^2 + \sum_{k=1}^{36} w_k \left(q_{\text{sim}} - q_{\text{meas}} \right)_k^2 + \sum_{l=1}^{3} w_l \left(qr_{\text{sim}} - qr_{\text{meas}} \right)_l^2, \qquad (3)$$

where *w* are weights, *h* are heads, Δ*h* are head gradients, *q* are seep and phreatophyte flows, *qr* are flow ratios, and subscripts "sim" and "meas" stand for simulated and measured, respectively. Weights carefully considered factors such as the importance of matching certain heads, gradients, and seeps, particularly those in and around Area IV.

3.2.1 Initial Weighting of Observations

The initial weights for observation targets were specified as a function of the observation variability. For heads, individual weights were the inverse of the standard deviation of the measurements. If the standard deviation in head was zero (indicating only one measurement) or less than 0.1, then the individual weight was calculated as the inverse of the average of the standard deviations of all the heads. This prevents excessively high weights for measurements that may have only a few data points. For gradients, individual weights were the inverse of the standard deviation of the gradients. For seep and phreatophyte flows, the standard deviation was calculated as

$$\sigma_X = \frac{100|X| - \frac{1}{10}|X|}{3.92}, \tag{4}$$

where *X* is the observation value. This was because the seep and phreatophyte flows were highly uncertain and their 95% confidence interval was assessed to be from 1/10 to 100× the measured value. The initial weights for flows were the inverse of their standard deviations. For the seep ratios, the initial weights were set equal to one, but were adjusted as described below.

3.2.2 Adjusted Weighting

The initial weights described above were adjusted by observation group factors (see Table 2 through Table 4). These adjusting group factors were influenced by the group's importance factor, which was based on professional judgment of how important it was that the FEFLOW model accurately reflect these observations. Throughout the model calibration, it was the goal that the value of the objective function comprise approximately 50% heads, 25% gradients, and 25% seeps and flow ratios. This goal was achieved using a recursive approach where the adjusted weights of the next PEST calibration were calculated as a function of the weights and observation group objective-function values of the previous PEST run. For each successive PEST-calibration weighting scheme, the adjusting group factors were scaled by the non-Area IV flows (*seeps*18) observation group objective function and non-Area IV flows group importance. The adjusting group factor, f_i, for the i^{th} observation group was calculated as

$$f_i = \sqrt{\frac{I_i \Phi_Q}{\Phi_i I_Q}}, \tag{5}$$

where I_i is the i^{th} group importance factor, Φ_Q is the value of the objective function for *seeps*18 from the preceding PEST calibration, Φ_i is the value of the objective function of the i^{th} group from the preceding PEST calibration, and I_Q is the *seeps*18 group importance factor. Thus, the adjusting group factor for *seeps*18 was equal to one and the remaining adjusting group factors were scaled such that their relative contribution to the total objective function stayed fairly constant at the 0.5:0.25:0.25 ratio. Again, an observation's weight from the previous run was multiplied by its respective adjusting group factor to obtain the adjusted weight for the subsequent PEST calibration. This procedure ensured that relative

contributions to the objective function remain fairly constant after each iteration of the calibration process. Including the hand changes to individual weights for head values from wells thought critical to constraining flow paths from contaminated wells, the final objective function comprised 56% heads, 23% gradients, and 21% seeps and flow ratios.

It is also important to note that the calibrated parameter values from a prior PEST iteration were used as initial values for the next PEST iteration.

4. Groundwater Model Calibration Results

Several plots have been made to visually evaluate calibration results for the various runs in a spatial and statistical sense. Ideally, head residuals should be randomly distributed in space. Head residuals should also be normally distributed with a mean of zero. Deviations from this may give information on structural errors in the flow model or unintended biases introduced in the objective function. Simulated flow paths should be generally consistent with the conceptual model of the flow system and should not be inconsistent with existing observations of groundwater contamination.

4.1 Simulated Head Residuals

A cross plot, two residual histograms, and two probability plots were constructed for the results of Run60. The cross plot (Figure 19) shows that higher residuals generally occur at measured head levels of 475 to 575 m. The histograms (Figure 20 and Figure 21) show that head residuals are skewed toward higher values (i.e., low simulated head). The probability plots (Figure 22 and Figure 23) show that distributions of head residuals deviate only somewhat from normal for both the entire model domain and the wells near and within Area IV.

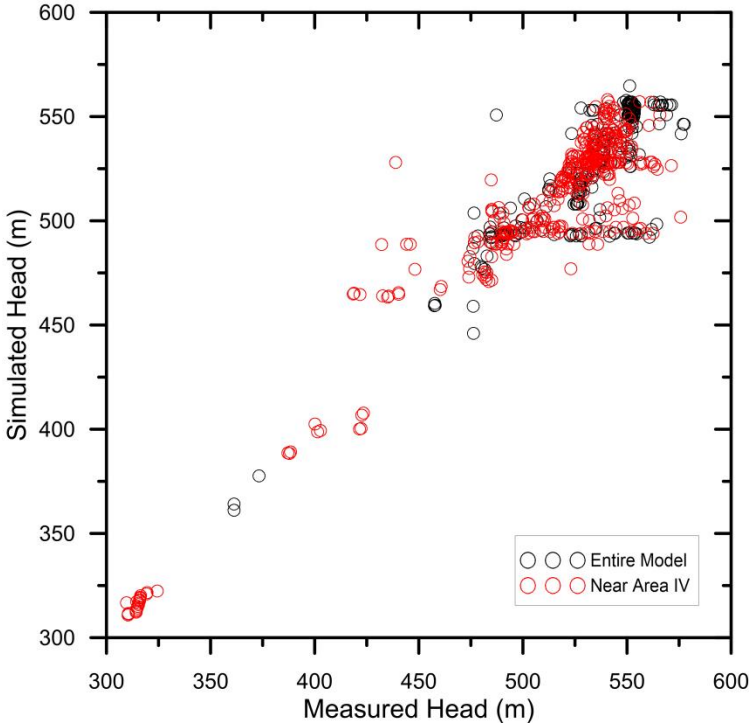

Figure 19: Plot of simulated versus measured heads in the calibrated flow model..

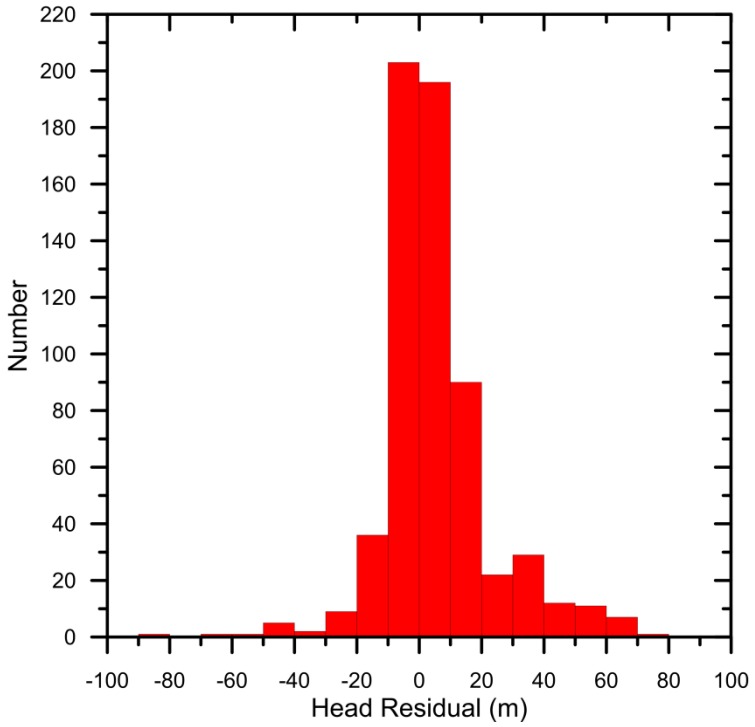

Figure 20: Histogram of head residuals in the calibrated flow model (entire model).

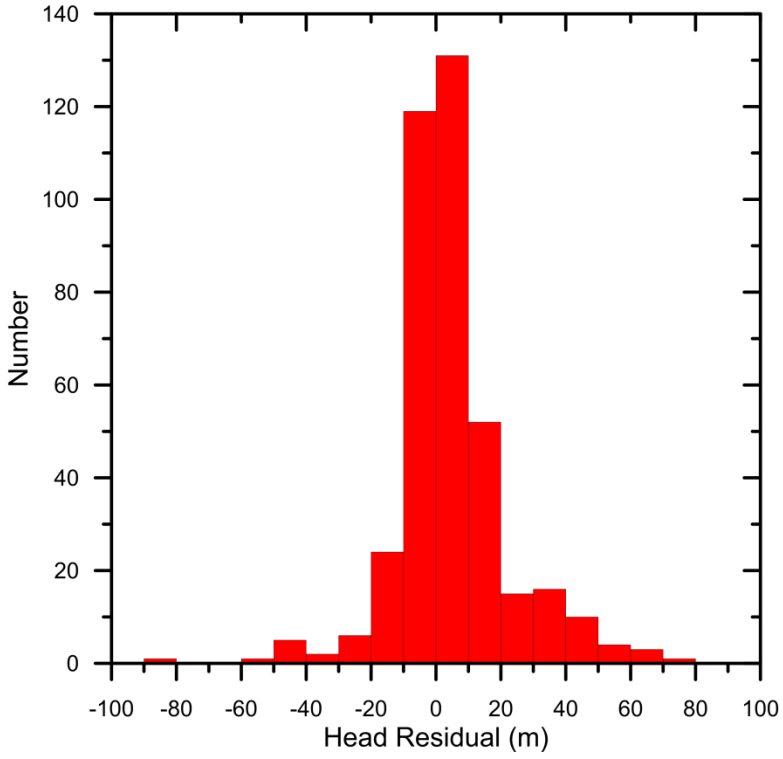

Figure 21: Histogram of head residuals in the calibrated flow model (within and near Area IV).

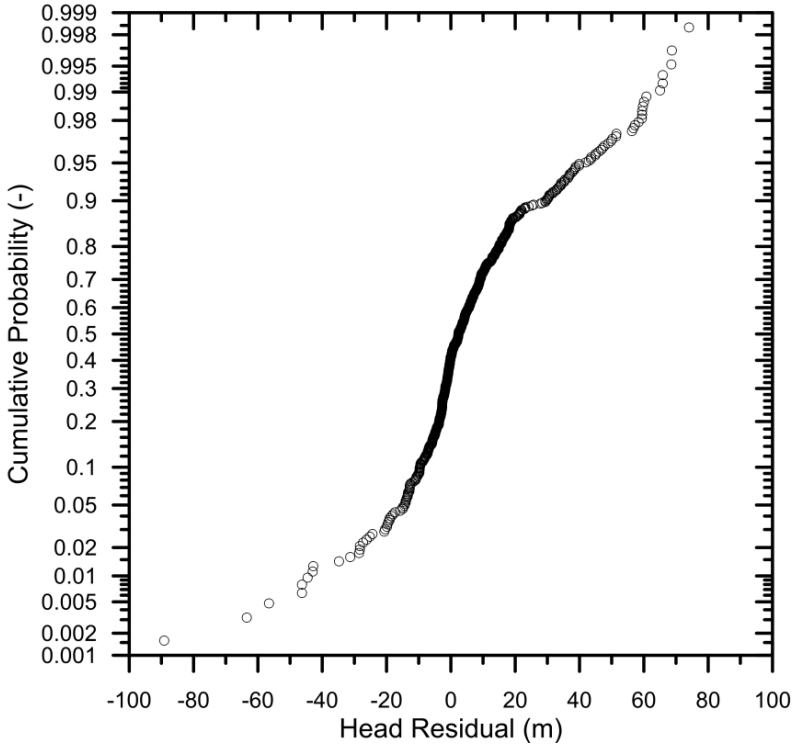

Figure 22: Probability plot of head residuals in the calibrated flow model (entire model).

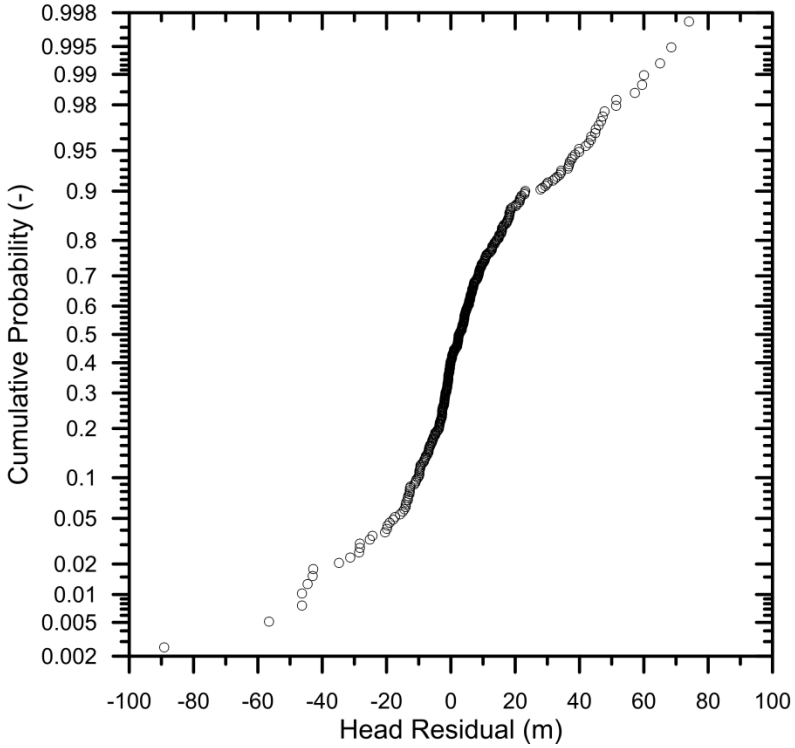

Figure 23: Probability plot of head residuals in the calibrated flow model (within and near Area IV).

The head residuals near Area IV are shown in Figure 24. The spatial distribution of head residuals near and within Area IV shows broad clustering of positive and negative values. Overall, the simulated heads are too low over most of Area IV. Caution should be used in interpreting this figure because values of residuals are superimposed for multi-completion wells.

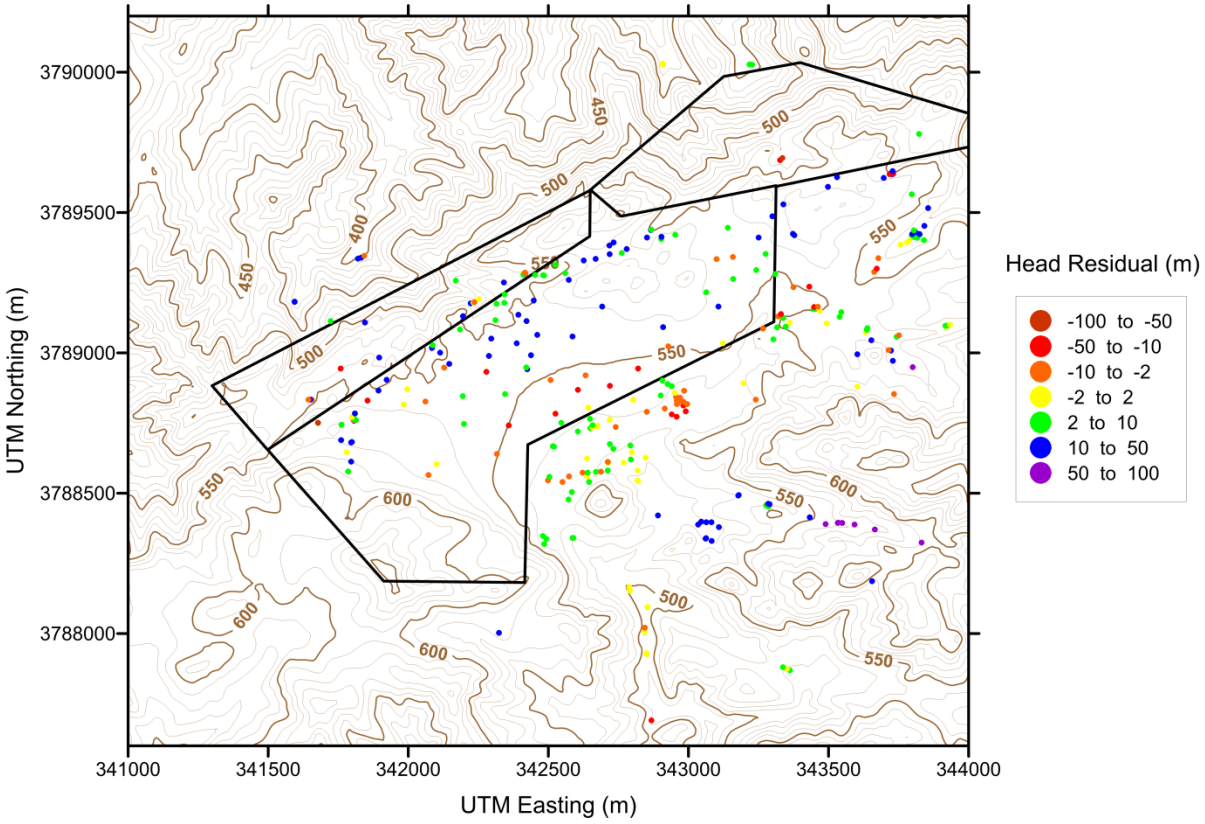

Figure 24: Head residuals in the calibrated flow model near Area IV.

4.2 Calibrated Parameter Values

With 674 unique parameters calibrated, results are presented in tables in the Appendix. Non-fault geologic units are listed in Table 8. Fault geologic units are in Table 9. Calibrated recharge multipliers are in Table 10.

4.3 Null Space Monte Carlo Analysis

Given that this is an underspecified system with 1,244 parameters but only 671 observations (more unknowns than equations), calibration of the model required the singular-value decomposition technique to be able to formulate a tractable problem (Christensen and Doherty, 2008; Tonkin and Doherty, 2005). That is, parameters were linearly combined into fewer super-parameters that can be uniquely estimated given the calibration data set (671 observations). However, this calibration technique also admits that there is an infinite combination of parameters that can calibrate the model roughly equally well. Sets of parameters that calibrate the model roughly equally well can be determined through a calibration-constrained Monte Carlo analysis, known as the null space Monte Carlo (NSMC) technique (James et al., 2009; Tonkin and Doherty, 2009). The goal of the NSMC analysis was to quantify uncertainty in flow-model predictions within the framework of model calibration uncertainty.

The first step in the NSMC technique was to generate 100 random sets of the 671 parameters using a normal distribution centered on the calibrated value with variance set by assuming that the ranges of calibrated parameter values from all 12 calibration exercise (12 calibration runs were made during the natural progression of this research with the last of these presented here) were equal to the 95% confidence interval (1.96 standard deviations). The PEST utility, SUPCALC (Doherty, 2016b), determined the number of super-parameters that would be uniquely estimated and for the objective function used in the calibration this was 82 super-parameters. Next, each of the 100 sets of random parameters, was modified using the PNULPAR (Doherty, 2016b) routine in PEST, which removed the projection of a random parameter field onto the calibration solution space (the component of the parameter field that comprises its ability to calibrate the model – the range of the parameter to which the objective function is sensitive). Finally, the set of solution-space adjusted random parameters was run through PEST to push each parameter to a value that calibrated the model. A total of 100 parameter sets that calibrate the model equally well (fit heads, head gradients, seeps, and flow ratios) resulted; each yielding different particle tracking results. This technique facilitated uncertainty quantification through the development of "horse tail" particle tracks emanating from each release point.

Flow paths from the 100 NSMC flow model simulations are shown in Figure 25 to Figure 36 for the 12 contaminant source locations. The particle track colored by depth below the land surface on each figure is that from the calibrated model. The gray particle paths shown in each figure represent multiple, equally likely flow paths from the same source location, corresponding to the NSMC realizations of the flow model. Flow paths represent streamlines emanating from each well until they exit the model domain. It is important to note that this means they are not constrained by time and in some cases the times necessary to exit the model domain exceed thousands of years.

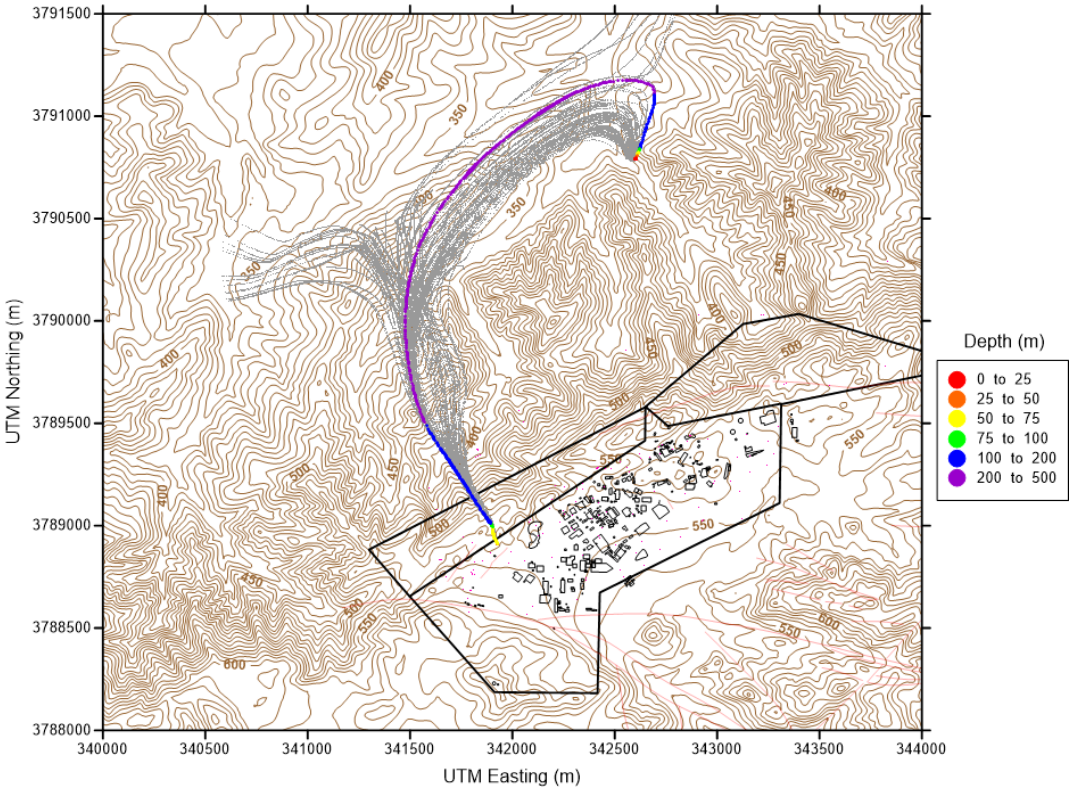

Figure 25: The 100 NSMC flow paths from well DD-140.

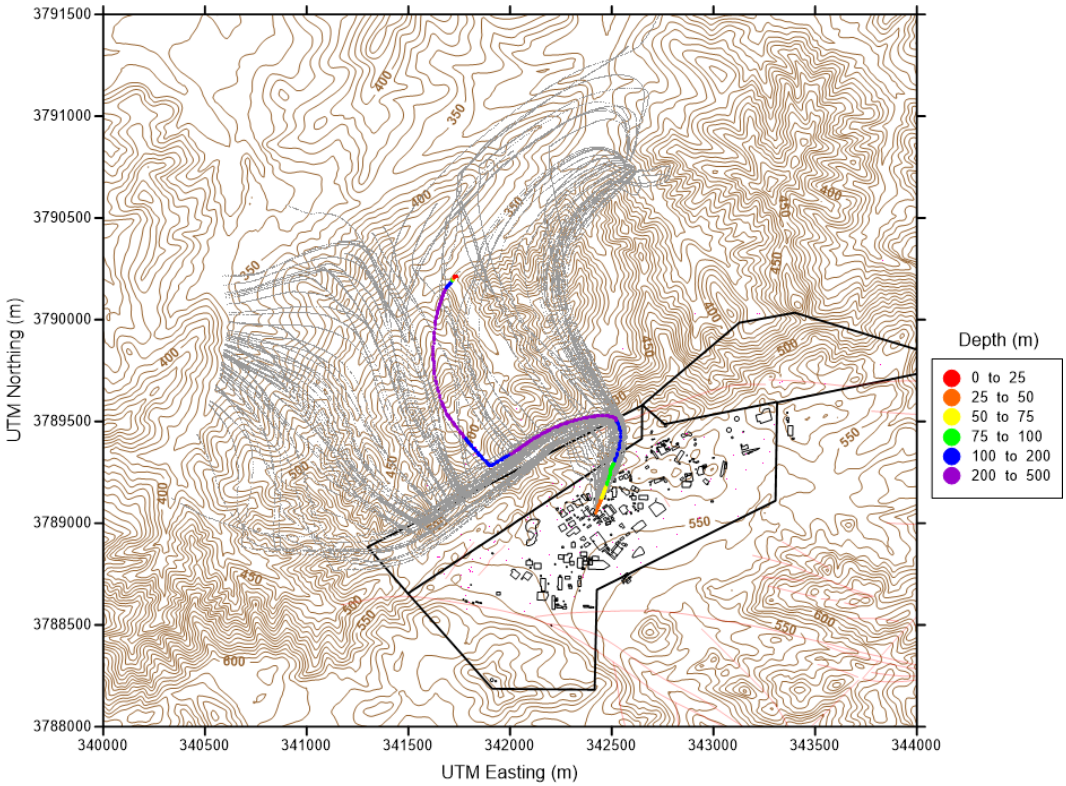

Figure 26: The 100 NSMC flow paths from well DD-144.

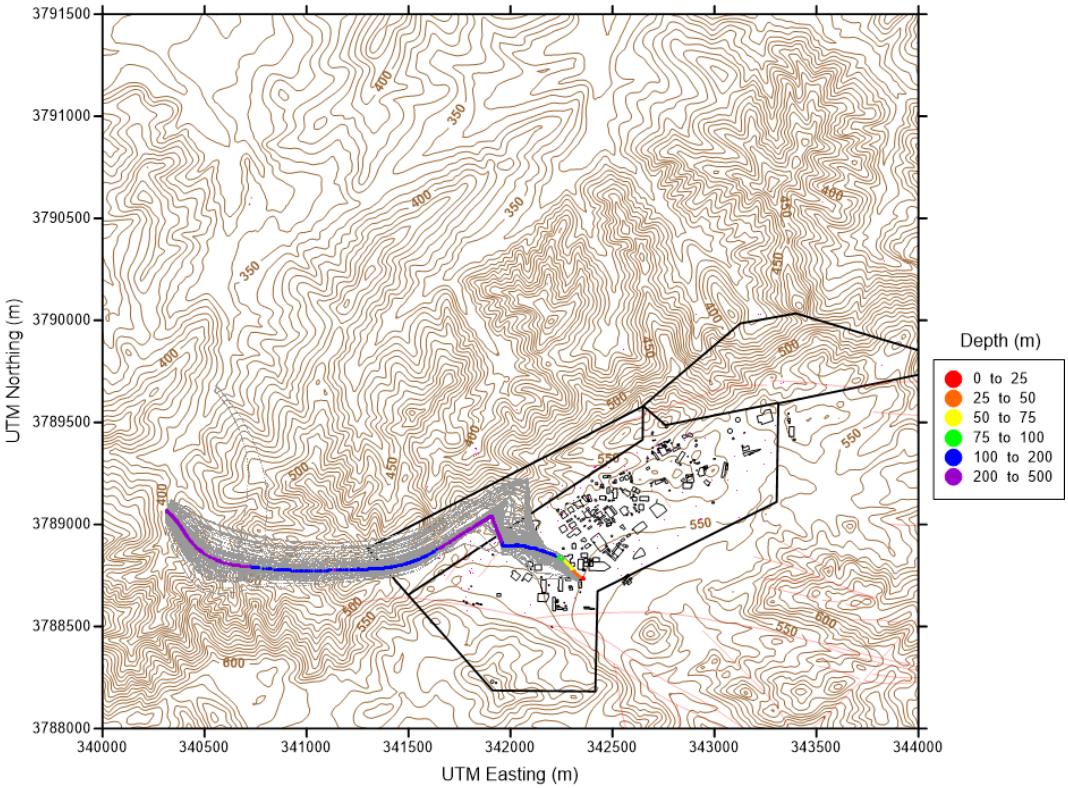

Figure 27: The 100 NSMC flow paths from well DD-145.

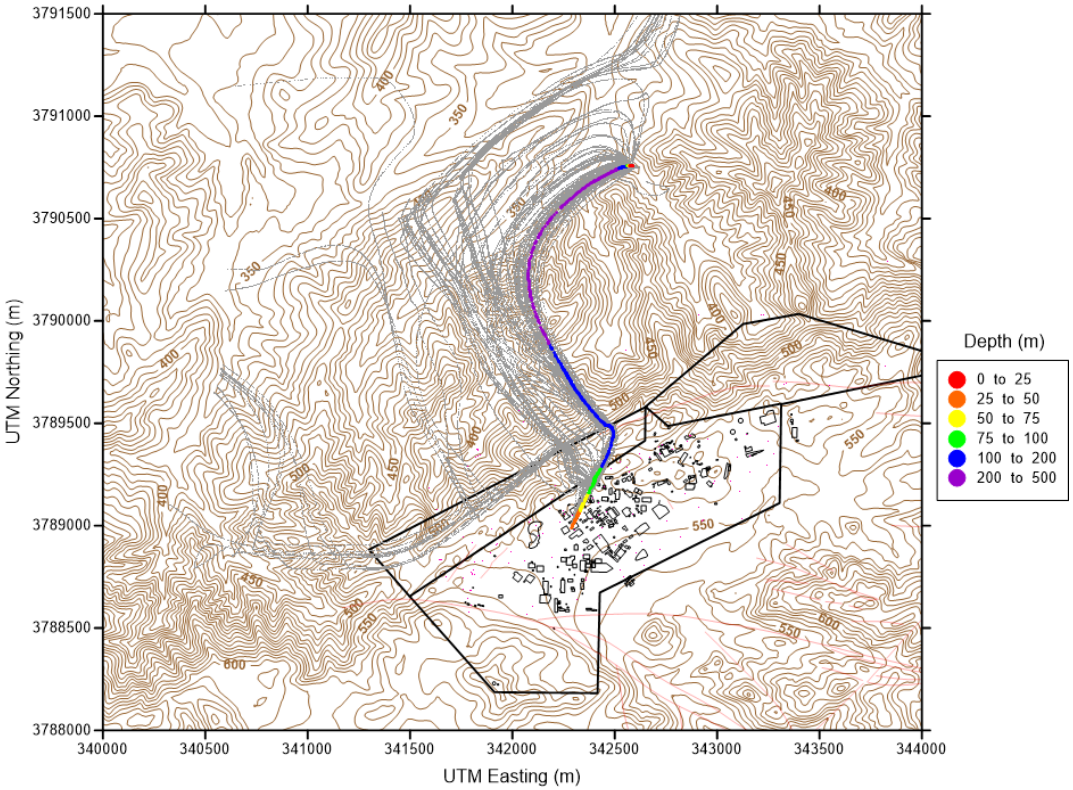

Figure 28: The 100 NSMC flow paths from well PZ-109.

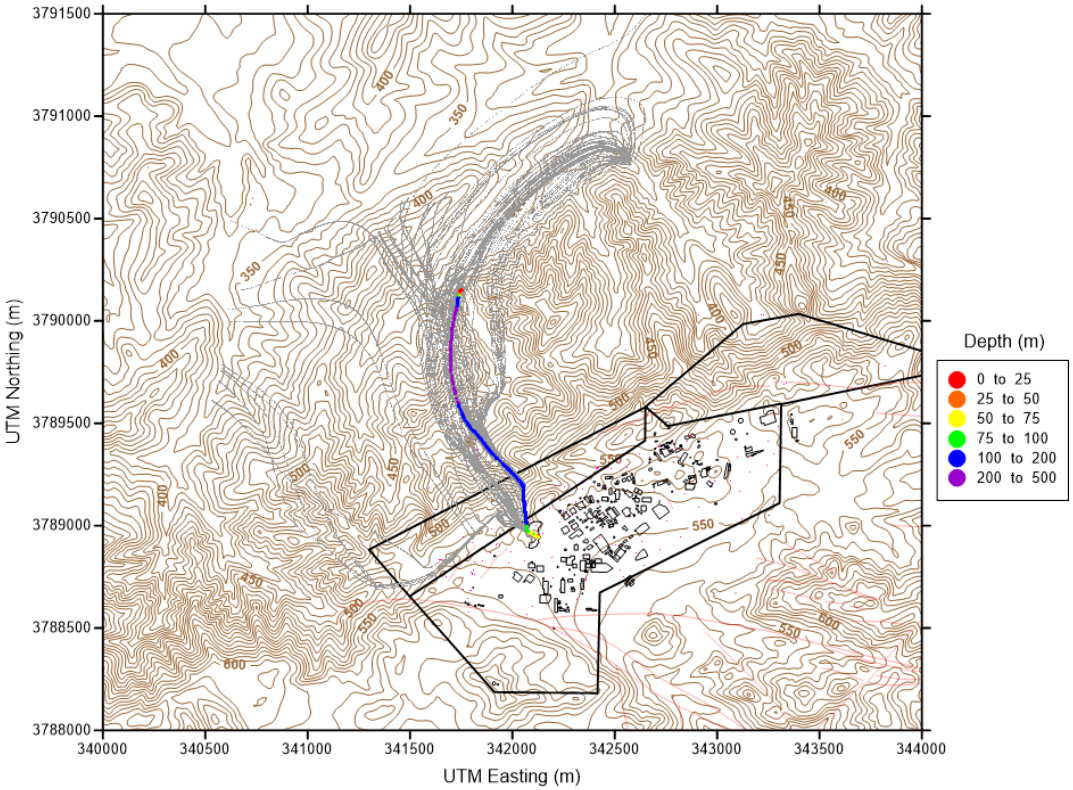

Figure 29: The 100 NSMC flow paths from well RD-07.

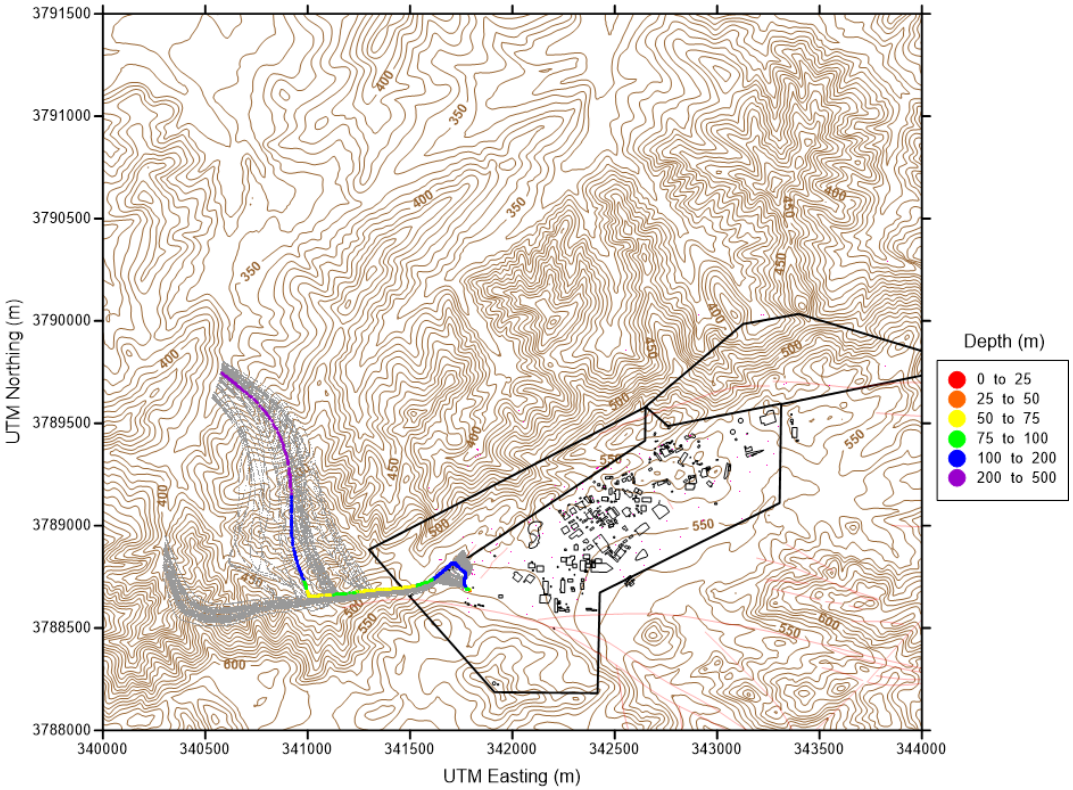

Figure 30: The 100 NSMC flow paths from well RD-21.

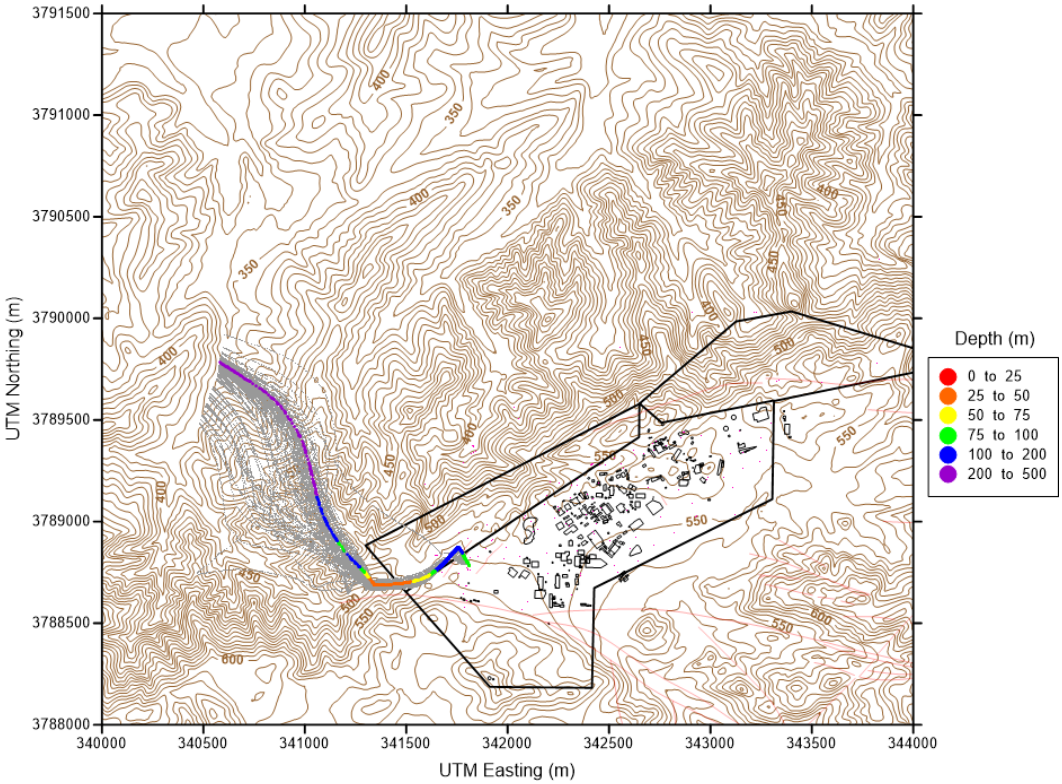

Figure 31: The 100 NSMC flow paths from well RD-23.

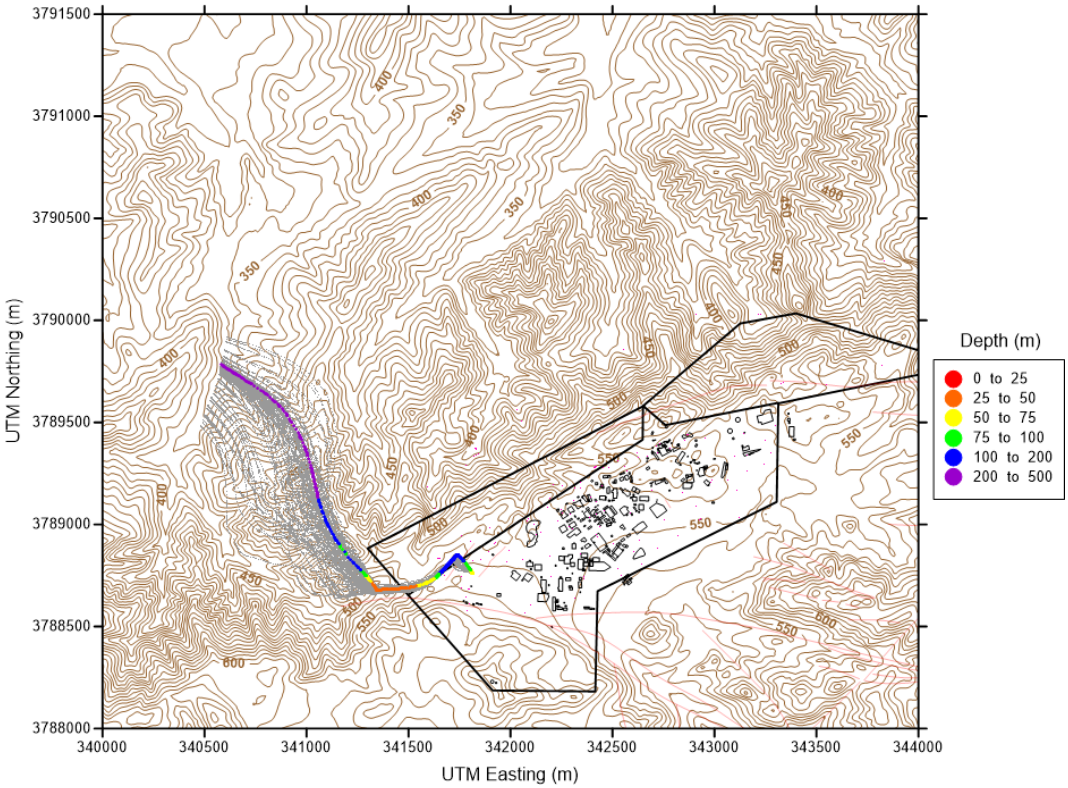

Figure 32: The 100 NSMC flow paths from well RD-54A.

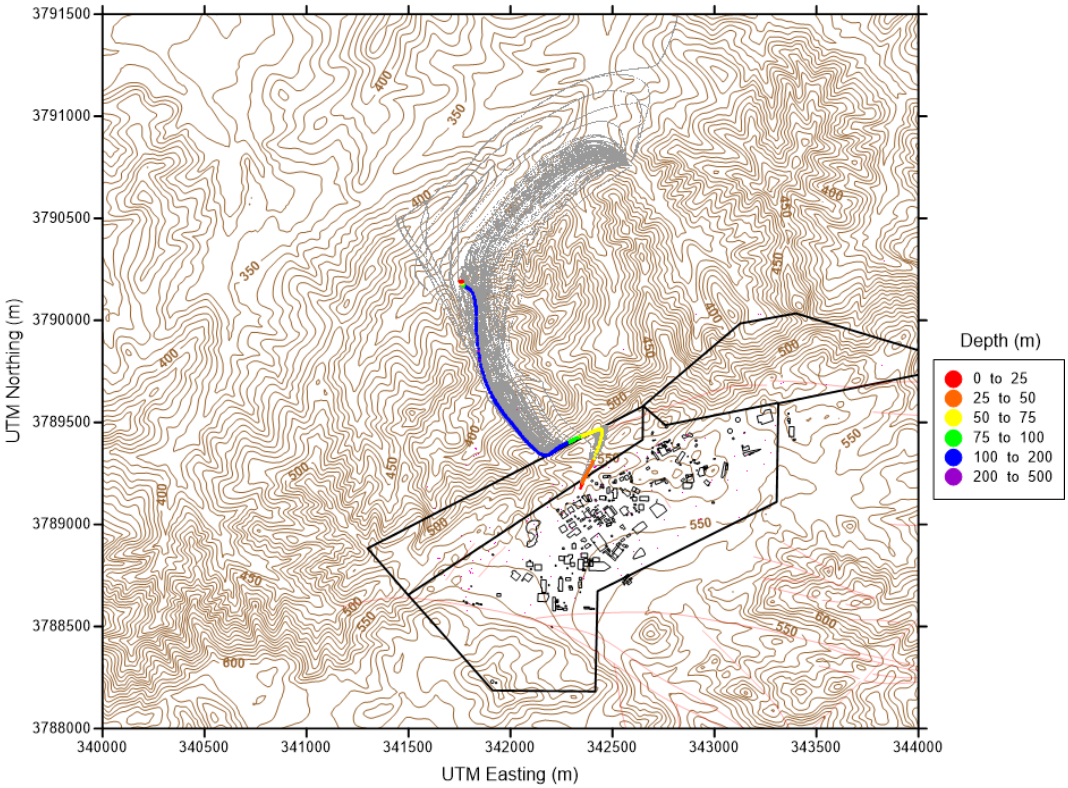

Figure 33: The 100 NSMC flow paths from well RD-90.

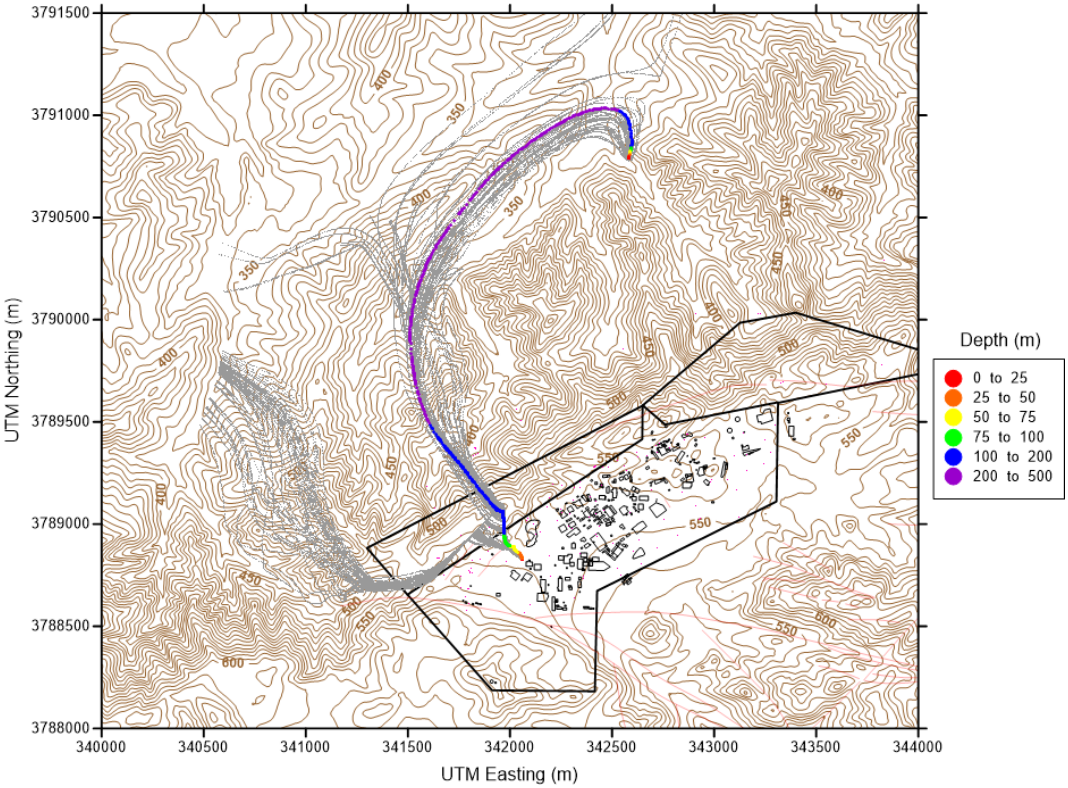

Figure 34: The 100 NSMC flow paths from well RD-91.

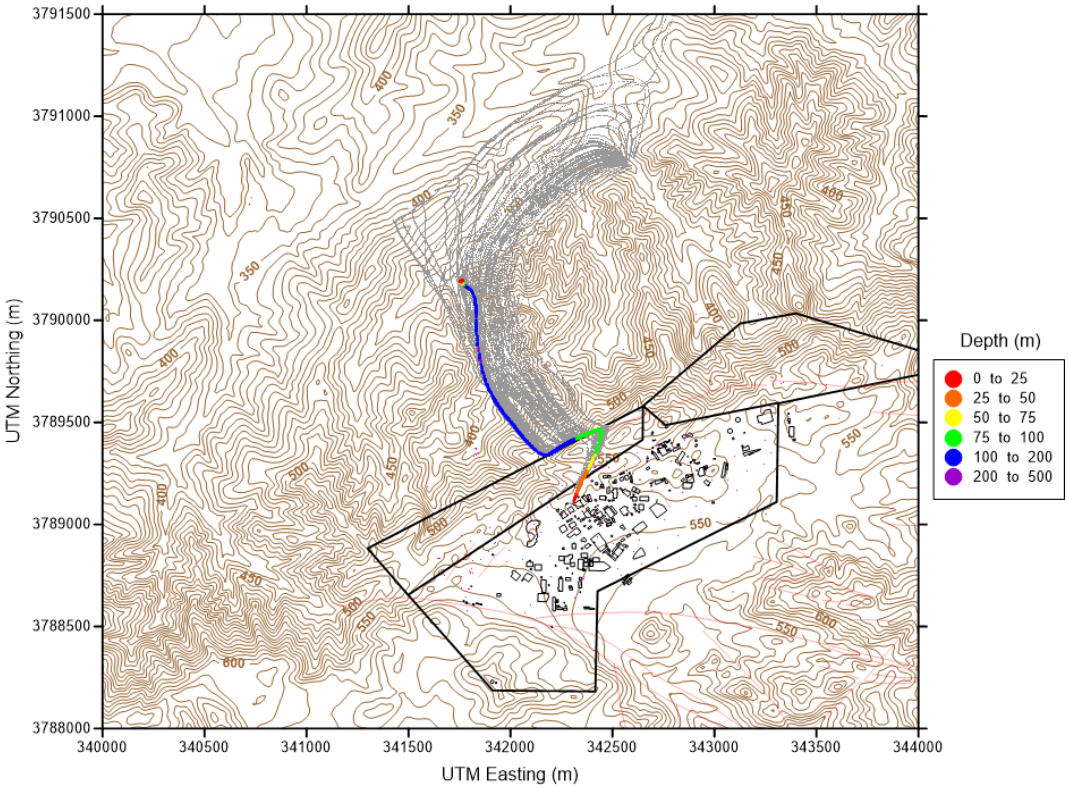

Figure 35: The 100 NSMC flow paths from well RD-95.

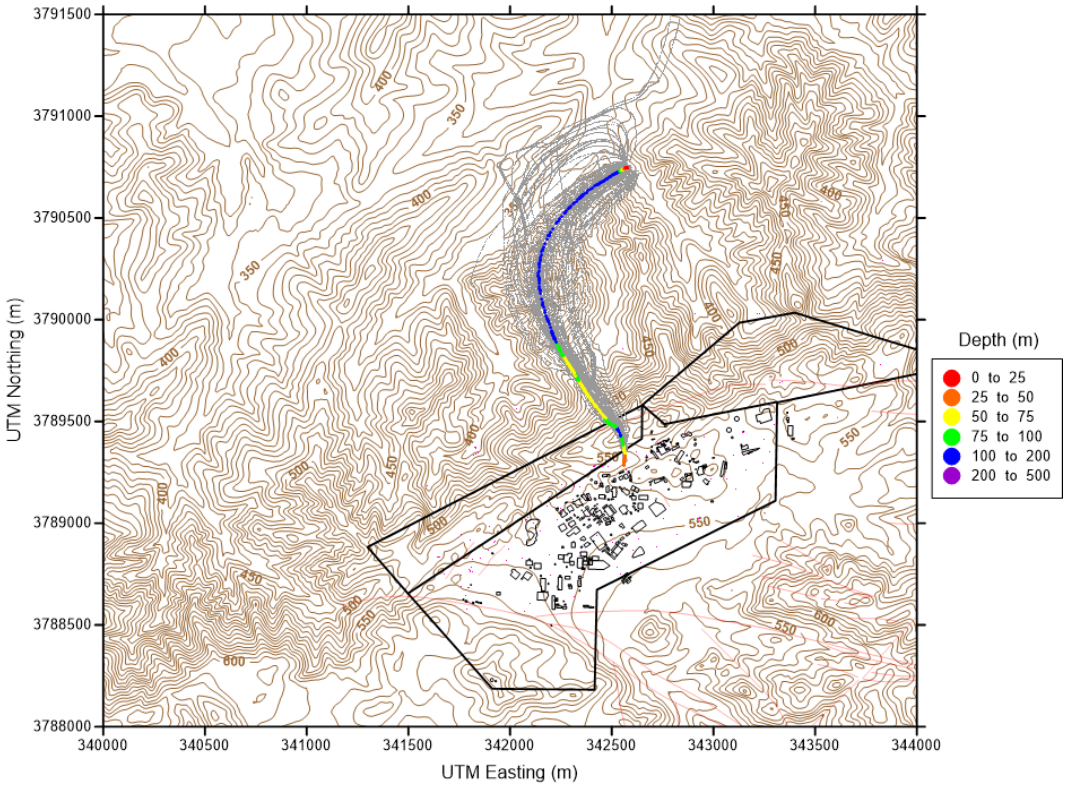

Figure 36: The 100 NSMC flow paths from well RD-98.

4.4 Simulated Flow Paths

FEFLOW has a particle-tracking algorithm that returns streamlines (flow paths) emanating from a specified source location. Random-walk dispersivity was turned off and the porosity for the entire site was set to a representative value of 0.15. One hundred NSMC particle tracks were developed for releases (5 m below the water table) at wells RD-23, RD-07, PZ-109, RD-95, RD-98, DD-144, and PZ-105, wells with groundwater contamination levels above maximum contaminant levels (MCLs) that are associated with sources for which DOE has potential responsibility.

The 100 NSMC particle paths provide a visual representation of uncertainty in groundwater flow paths from the contaminant source locations and the ultimate discharge locations of groundwater along the flow paths. As expected, the width of the uncertainty band increased with distance from the source with some sources having highly divergent potential flow paths (e.g., RD-91). It should be noted that the contaminant plume width for each flow path would be influenced by transverse dispersion, which was not included in the particle-tracking analysis. Consequently, the ensemble uncertainty in contaminant pathways from a given source would be wider than indicated by the particle paths shown in Figure 25 to Figure 36.

The strength of the NSMC particle tracking results is that not only is the flow path associated with the lowest achievable objective function available (colored flow path on the following figures), but now flow path uncertainty can be quantified. With 100 flow paths available, only the most distant two or three flow paths on either side of the colored flow path are outside of the 95% confidence interval. It is interesting to note that there was a notable level of uncertainty in the flow-path exit locations. That is, the flow paths

exited the model domain at multiple seep locations or across a fairly broad distance along the model boundary (e.g., Figure 34). However, it is critical to note that these uncertainties are in flow paths that are independent of time in this steady-state model. Transport paths will be much shorter with sharply declining contaminant concentrations because of all of the retardation, dispersive, and degradation mechanisms in the system (e.g., dispersion, matrix diffusion, sorption, decay, etc.). Moreover, these results represent a conservative estimate of uncertainty because random-walk dispersion was not considered in the calibrations.

4.5 Sensitivity to Fault Hydraulic Properties

It is important to understand how model features impact the simulation. In Area IV, two important features within the flow model domain are the three westernmost segments of Burro Flats Fault (BFF) indicated in Figure 37 and what is known as the Sodium Reactor Experiment/Radioactive Materials Handling Facility (SRE/RMHF) Lineament indicated in magenta as a segment of the North Fault in Figure 38. To assess the sensitivities of the model calibration and simulated flow paths from contamination sources to these features, their hydraulic conductivities were systematically increased by an order of magnitude (made less of a barrier to flow) and decreased by an order of magnitude (made stronger flow barriers). If the calibration was significantly impacted (i.e., an increase in objective function components of >10%), this indicates that the hydraulic conductivities of these features are important to establishing water levels, head gradients, and flows. Changes to the flow paths were also examined.

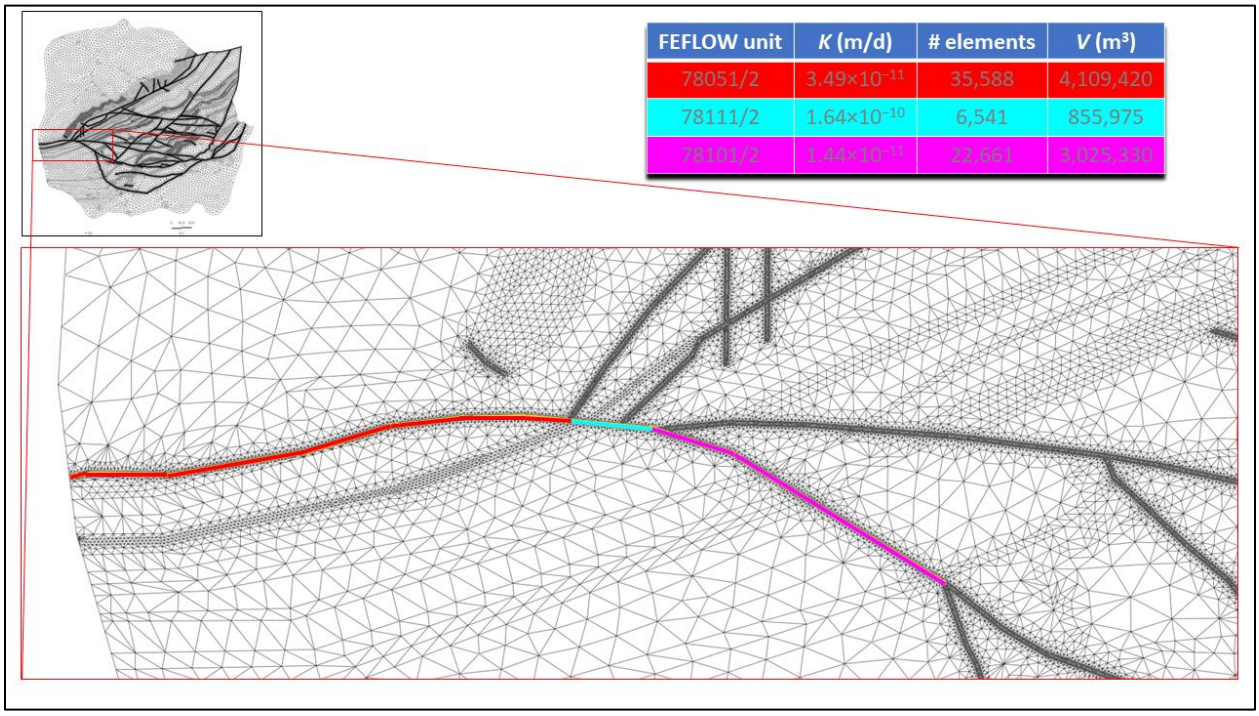

Figure 37: The three segments of the Burro Flats Fault that were adjusted in the sensitivity study.

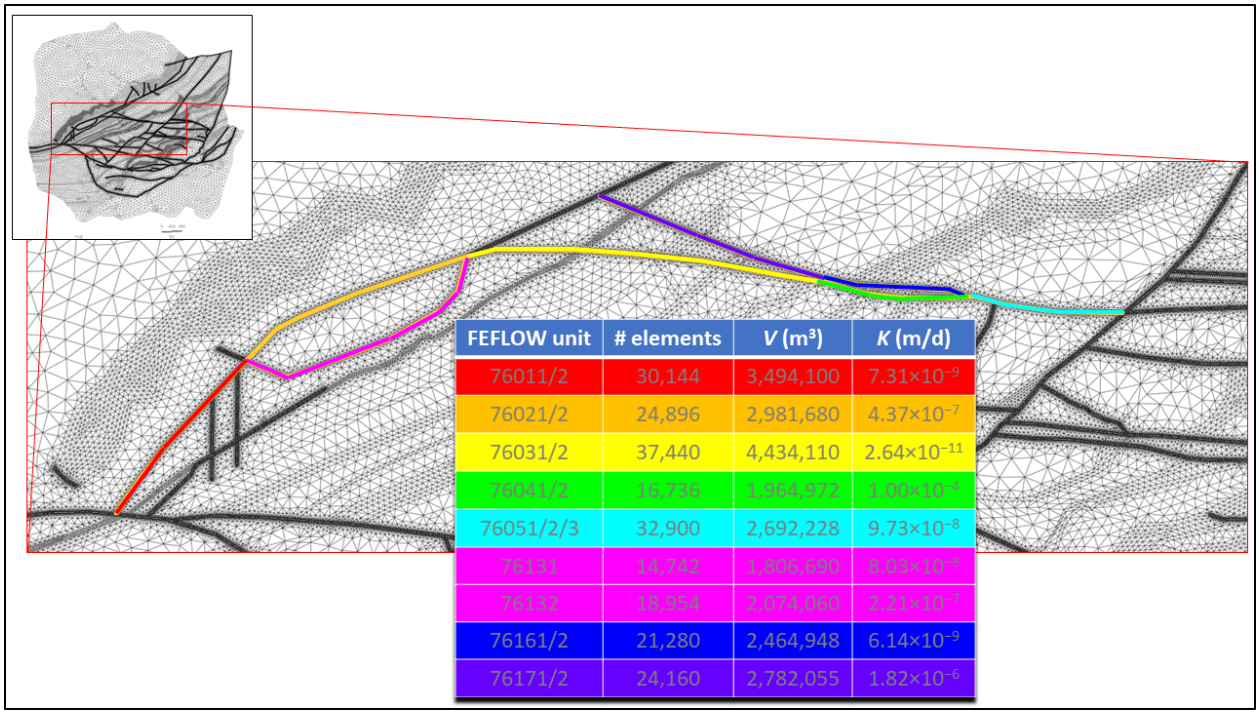

Figure 38: Segments of the North Fault with the SRE/RMHF Lineament in magenta.

Table 5 lists the increases to the total objective function as well as the change to each of its components subject to the fault sensitivity study. Note that an increase in the objective function corresponds to a poorer match between simulated and observed values. Specific observations include:

- Increasing the Burro Flats Fault hydraulic conductivity by an order of magnitude: Increased the total objective function by 22% and the component for the heads in Area IV (*heads8*) by 66%. This fault must act as a barrier to flow or it prevents the simulation from honoring observed water levels in Area IV.
- Decreasing the Burro Flats Fault hydraulic conductivity by an order of magnitude: Increased the objective function by only 1% and *heads8* by only 2%. This indicates that the fault is acting as a barrier to flow and augmenting the barrier makes little difference to the calibration.
- Increasing the SRE/RMHF Lineament hydraulic conductivity by an order of magnitude: Increased the objective function by 4% and that for heads by 9%. Head gradients (*grads17*) and seeps (*seeps19*) in Area IV, though, degraded by 24% and 20%, respectively. This feature must be a barrier to flow or it prevents the model from honoring the observed gradients and flows in Area IV.
- Decreasing the SRE/RMHF Lineament hydraulic conductivity by an order of magnitude: Increased the objective function by 4% and that for *heads8* by 10% (about the same as the preceding sensitivity iteration). Head gradients in Area IV improved by −4% while seeps in Area IV degraded by 2%. While making this feature act as a stronger flow barrier degrades the overall calibration, it slightly improves the gradients in Area IV.

Table 5: Change in objective function components for the feature sensitivity study.

Objective function	BFF × 10	BFF × 0.1	SRE × 10	SRE × 0.1
Total	**22%**	1%	4%	4%
grads11	0%	0%	1%	−1%
grads12	0%	0%	−6%	5%
grads14	0%	0%	1%	0%
grads15	0%	0%	−1%	2%
grads16	0%	0%	−12%	12%
grads17[*]	−29%	−2%	**24%**	−4%
heads1	−1%	−3%	−4%	1%
heads2	0%	−2%	22%	0%
heads3	1%	0%	18%	−14%
heads4	1%	1%	2%	0%
heads5	−1%	−1%	17%	0%
heads6	28%	9%	10%	−3%
heads7	−1%	0%	0%	0%
heads8[*]	**66%**	2%	9%	10%
seepratios	−6%	−6%	7%	2%
seeps18	0%	0%	−1%	0%
seeps19[*]	0%	0%	**20%**	2%
[*]Area IV				

Particle tracks for the sensitivity runs are shown in Figure 39 for the Burro Flats Fault and Figure 40 for the SRE/RMHF Lineament. Black particle tracks are for the calibrated hydraulic conductivities with red and blue tracks corresponding to increasing and decreasing hydraulic conductivities by an order of magnitude, respectively. Given that head gradients and seeps calibrations were not significantly impacted by changes to the Burro Flats Fault hydraulic conductivities, flow paths were minimally impacted. Because head gradients and seeps calibrations were notably degraded in Area IV if the SRE/RMHF Lineament acts as less of a barrier, there are more evident changes to the flow paths. Overall, the sensitivity study reveals that the calibrated model properly identified the Burro Flats Fault and SRE/RMHF Lineaments as barriers to flow required to honor observed heads in Area IV and head gradients and seeps in Area IV, respectively. Impacts to simulated flow paths from contaminant source locations are relatively small for the range of uncertainty in hydraulic conductivity of these features considered in the sensitivity analysis.

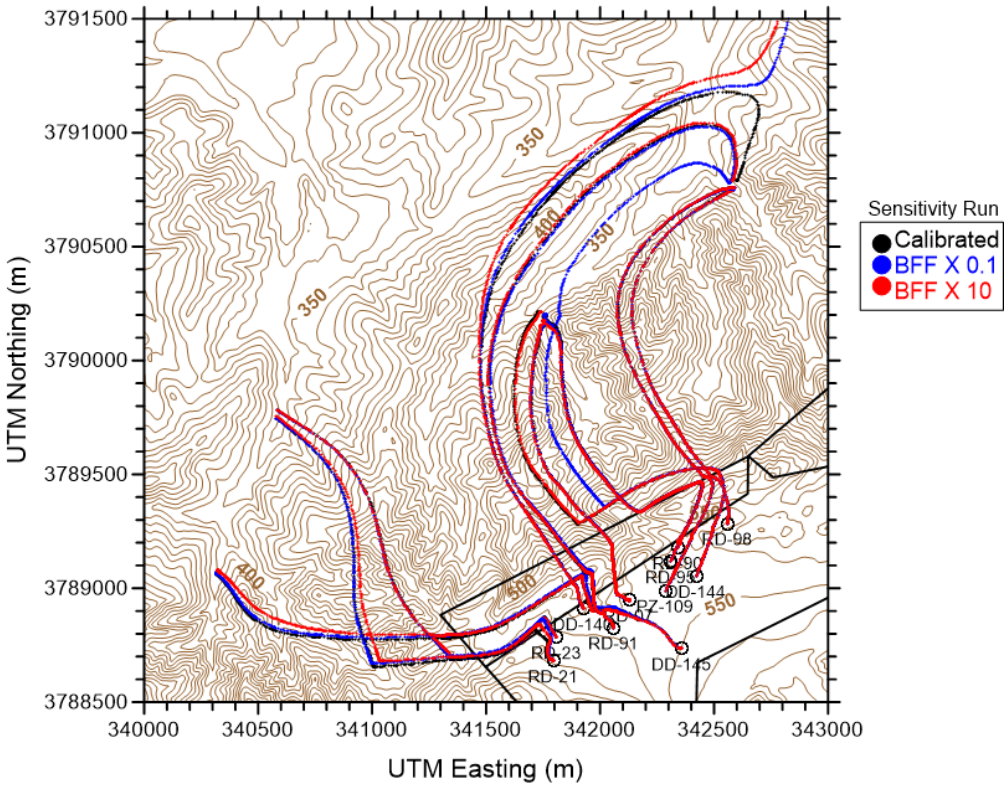

Figure 39: Particle tracks from the BFF sensitivity studies.

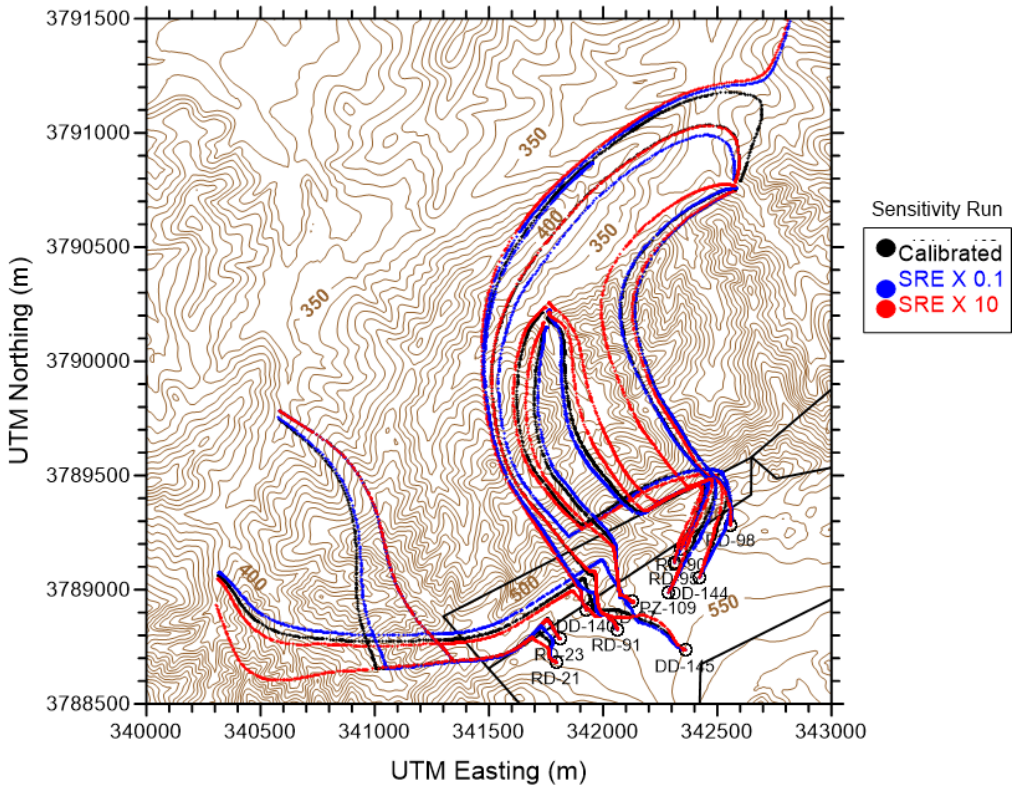

Figure 40: Particle tracks from the SRE sensitivity studies.

4.6 Contaminant Transport Model

4.6.1 Introduction

The updated and recalibrated mountain-scale groundwater flow model simulated groundwater flow paths from sources of groundwater contamination using particle tracking and the specific discharge along those flow paths. In addition, the null-space Monte Carlo analysis quantified the uncertainty in those flow paths and groundwater flow rates, as described previously. However, the particle tracking algorithm in FEFLOW does not provide simulated contaminant concentrations or important transport processes (e.g., dispersion, , matrix diffusion, sorption, decay, etc.).

A separate one-dimensional (1-D) contaminant transport model was developed and linked to the particle tracking results from the mountain-scale groundwater flow model to simulate contaminant migration from selected locations of observed groundwater contamination. The objectives of the transport model were to give reasonable estimates of the extent of contaminant migration and the maximum contaminant concentrations in groundwater with times since release. The transport model was constructed to include important features and processes relevant to the fate and transport of contaminants in groundwater. However, the model was subject to simplifications, limitations, and uncertainties, such as the 1-D nature of the model and the assumption of groundwater flow in parallel, evenly spaced fractures. Consequently, the transport model is not intended to make precise predictions of contaminant migration, but does provide reasonable guidance for remedial investigations at the site.

4.6.2 Conceptual Model of Contaminant Transport

The conceptual model of groundwater contaminant transport included release of contaminants at the surface or in the shallow subsurface, generally vertical migration in the vadose zone, and lateral transport in groundwater below the water table. Some contaminants, such as TCE, may have been released as dense non-aqueous phase liquids (DNAPLs), but the generally low groundwater concentrations of TCE and the lack of deep contamination in Area IV suggest that vertical migration of TCE as a DNAPL was limited. Physical and chemical processes potentially important to groundwater contaminant transport include advection in bedrock fractures, hydrodynamic dispersion, diffusion in the rock matrix, sorption in the matrix, radioactive decay of radionuclides, and possible chemical degradation of organic compounds.

The 1-D conceptualization of advective transport was steady-state flow along a single groundwater flow line or stream tube with groundwater movement confined to the fracture network. The steady-state conditions established in the calibrated mountain-scale groundwater flow model were considered representative of average flow conditions in the past and future in Area IV, which has been affected less by historical groundwater pumping than some other areas at the SSFL. Groundwater specific discharge was variable along the flow path as the groundwater flows through hydrogeologic units of varying hydraulic conductivity. The cross-sectional area of a groundwater stream tube varied accordingly, with a smaller cross-sectional area in zones of high conductivity and larger areas in zones of low conductivity. Hydrodynamic dispersion occurred in the longitudinal and transverse directions, but the 1-D conceptual model included only longitudinal dispersion. Neglecting transverse dispersion resulted in overestimates of contaminant concentrations in numerical simulations. The simplified conceptual model of matrix diffusion was a system of parallel, evenly spaced fractures with diffusive mass transfer between the fractures and matrix occurring perpendicular to the fractures. An equilibrium, linear-isotherm model for sorption of relevant aqueous species was included in the conceptual model. Radionuclide mass and activity reduction occurred by first-order radioactive decay. Several lines of evidence indicate that chemical degradation of TCE has occurred in groundwater at the site. Alternative potential conceptual models of degradation are available; however, such processes were conservatively not included in the contaminant transport model, resulting in potential overestimates of contaminant concentrations.

The exact timing, duration, and location of contaminant releases that have affected groundwater quality in Area IV are uncertain. The conceptual model of contaminant sources in the 1-D transport model was assumed to be a continuous release of a specified concentration with a duration of 10 years, beginning approximately 50 years ago. Contaminant sources at seven locations were included in transport model simulations. These locations were specified as wells with observed groundwater contamination. The locations, associated presumed source, and contaminants of concern are listed in Table 6.

Table 6. Contaminant source locations for the 1-D transport model.

Well	Associated facility	Contaminant of concern
RD-23	FSDF	TCE
RD-07	Building 56 Landfill	TCE
PZ-109	Building 4057/4059/4626	PCE
RD-95	Uncertain	Tritium
RD-98	RMHF Leachfield	SR-90
DD-144	HMSA	TCE
PZ-105	Metals Clarifier/DOE Leachfields	TCE

4.6.3 Numerical Implementation

The 1-D transport model was implemented using the FEHM software code with the FEM (Zyvoloski, 2007). The model domain consisted of a series of quasi-3D elements connected along the stream line derived from the particle tracks. Each element in the model was 1 m in length. The streamtube defined by the 1-D transport model had a nominal cross-sectional area of 1 m^2 that varied in thickness transverse to flow to account for variations in specific discharge along the stream path. The groundwater flow rate simulated by the mountain-scale model was specified at the upstream end of the 1-D transport model and the downstream end was specified hydraulic head.

Each element volume was subdivided into a groundwater flow domain corresponding to fractures in the bedrock and a rock matrix domain using the generalized dual-porosity module in FEHM. Flow occurred only in the fracture domain, diffusive mass transfer of contaminants occurred between the fracture domain and the rock matrix, and diffusion occurred within the rock matrix. Radioactive decay or chemical degradation occurred in the fractures and matrix, and sorption may occur in the rock matrix. The rock matrix was discretized into ten elements that increased exponentially in thickness perpendicular to the fracture to obtain a more accurate numerical solution to the matrix diffusion process. The generalized dual-porosity algorithm implemented in the 1-D transport model was equivalent to a system of parallel, evenly-spaced fractures in the porous bedrock.

Parameter values representative of the average hydrogeologic conditions in Area IV and of the contaminants of concern were used in the 1-D transport model. The relevant parameters specified in the model are listed in Table 7.

Table 7. Parameter values in the 1-D transport model.

Parameter	Value
Fracture porosity (−)	0.01
Rock matrix porosity (−)	0.14
Longitudinal dispersivity (m)	10
Bulk density (kg/m^3)	2750
Effective diffusion coefficient (m^2/s) (TCE, PCE, Sr-90)	1.8×10^{-11}
Effective diffusion coefficient (m^2/s) (Tritium)	5.5×10^{-11}
Sorption coefficient of Sr-90 (mL/g)	15
Half-life of tritium (years)	12.3
Half-life of Sr-90 (years)	28.8

Parameter values used in the 1-D contaminant transport model were taken primarily from MWH Inc. (2009). The sorption coefficient for strontium was based on a review of data on sorption, as related to groundwater pH and clay content of the aquifer medium (U.S. EPA, 1999). The value of 15 mL/g was the minimum of the range given for near neutral pH and 10 to 20 weight% clay content.

A continuous source of contaminated groundwater at a specified concentration was applied at the upstream end of the 1-D transport model for the first ten years of the simulation. Conceptually, this source could correspond to infiltration from the vadose zone, a leach field, leaking surface impoundment, or dissolution of a DNAPL source. Because the original source concentrations at the site are unknown, the value of the specified concentration at the beginning of the simulation was determined by a trial-and-error method in which the specified concentration was adjusted so that the maximum simulated contaminant

concentration near the source after 50 years was approximately equal to the average currently observed concentration. This process of calibrating the contaminant source concentration was conducted separately for each of the source locations investigated.

4.6.4 Transport Model Results

The results of the 1-D contaminant transport model are presented as a series of figures for the seven source locations listed in Table 6. Figure 41 to Figure 75 are series of figures repeated for each source location, so that Figure 41 to Figure 45 are a set for a TCE source at the location of well RD-23, Figure 46 to Figure 50 are a set for a TCE source at RD-07, etc.

The first figure in each set is a map showing the simulated particle path from the calibrated mountain-scale flow model (shown in color) superimposed on the multiple, equally likely particle paths from the null-space Monte Carlo analysis (shown in gray). The color scale indicates the depth below ground surface of the particle path along its entire length from the source to either a groundwater discharge point or the boundary of the mountain-scale model.

The second figure in each set has a plot of groundwater flux versus distance along the stream line particle path and plots of simulated contaminant concentration versus distance along the stream line for 20, 50, and 100 years after release at the contaminant source. The first plot is calculated from the particle tracking results of the mountain-scale flow model and is an input to the 1-D transport model. The second plot is output from the 1-D contaminant transport model.

The third, fourth, and fifth figures in each set are maps that illustrate the results of the 1-D transport model regarding the estimated migration distance of contaminated groundwater for 20, 50, and 100 years after release at the contaminant source, respectively. The simulated contaminant concentrations along the particle path are indicated by the colors plotted and represent a snapshot of the distance contamination has traveled at that time. The simulated particle paths have been truncated for values of simulated concentration that are less than one tenth of the MCL (e.g., at a value of 0.5 μg/L for TCE).

The results indicate significant variation in the extent of simulated contaminant migration from the different source locations. The TCE plumes from the locations of wells RD-23 and RD-07, and the Sr-90 plume from RD-98 are simulated to migrate a few tens of meters 100 years after release. The limited contaminant migration from the locations of RD-23 and RD-07 is attributable to the low simulated groundwater flux on the order of 0.01 to 0.03 m/year in the region immediately downgradient of the source. The limited migration of Sr-90 from the location of RD-98 is associated with the sorption of strontium onto the sandstone matrix. The more extensive simulated migration of TCE, PCE, and tritium of up to several hundred meters from the locations of the other wells is related to the higher values of simulated groundwater flux downgradient of the wells, generally on the order of 0.1 to 1 m/year and the absence of assumed sorption of the contaminants.

The maximum simulated contaminant concentrations decreased with time for all contaminants because of the processes of longitudinal dispersion and matrix diffusion, as shown in Figure 42, Figure 47, Figure 52, Figure 57, Figure 62, Figure 67, and Figure 72. In addition, radioactive decay resulted in decreases in maximum simulated concentrations for tritium by orders of magnitude and for Sr-90 by several times over the period of 100 years following the contaminant releases. The 1-D transport model results

indicated that the maximum concentrations for tritium from the location of well RD-95 and for TCE from well PZ-105 decreased below the MCL for those contaminants within 100 years of contaminant release.

The variability and uncertainty in potential groundwater flow paths from the source locations are indicated by the results of the null-space Monte Carlo particle tracking analyses shown in Figure 41, Figure 46, Figure 51, Figure 56, Figure 61, Figure 66, and Figure 71. However, neither these particle tracking results nor the 1-D contaminant transport model results included the effects of transverse dispersion, which spreads groundwater contamination in the direction perpendicular to the flow path. Consequently, the complete envelope of uncertainty in groundwater flow paths from the source locations would be wider than indicated by the NSMC results.

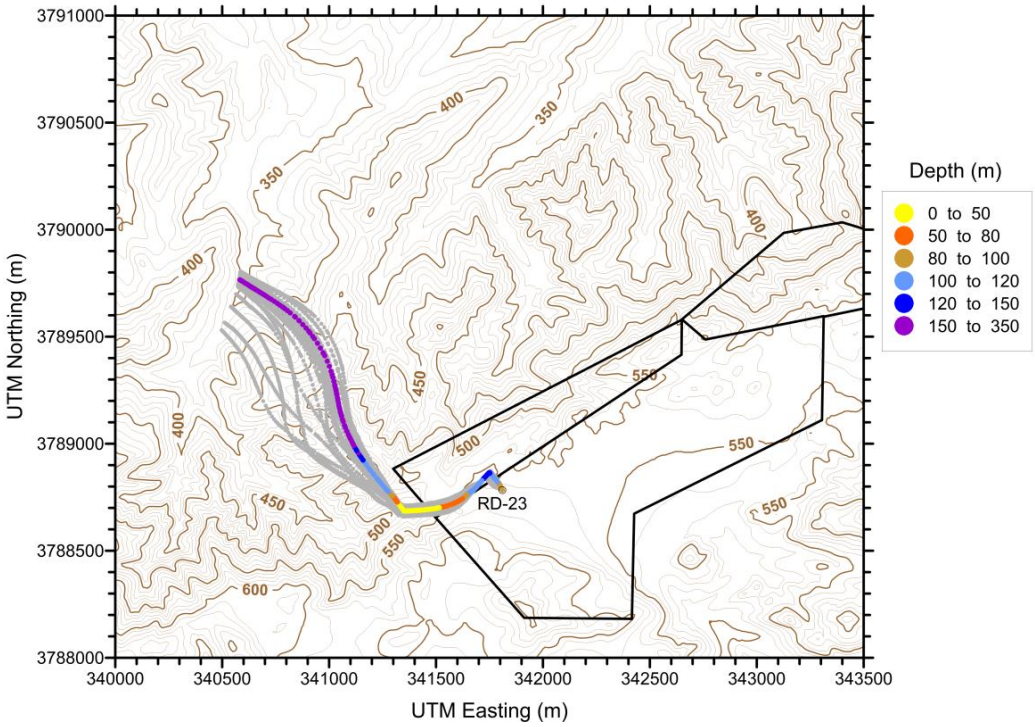

Figure 41: Simulated groundwater flow path with depth from well RD-23. Alternative flow paths from the null-space Monte Carlo analysis are shown in gray.

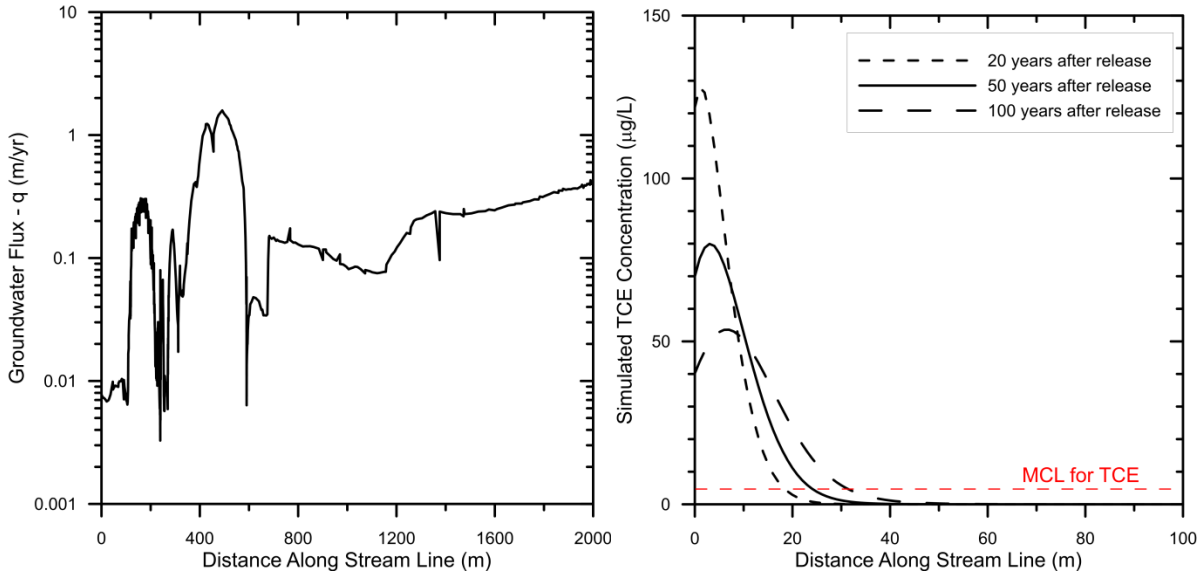

Figure 42: Simulated groundwater-flux profile and TCE-concentration profiles for three times following release along the flow path from well RD-23.

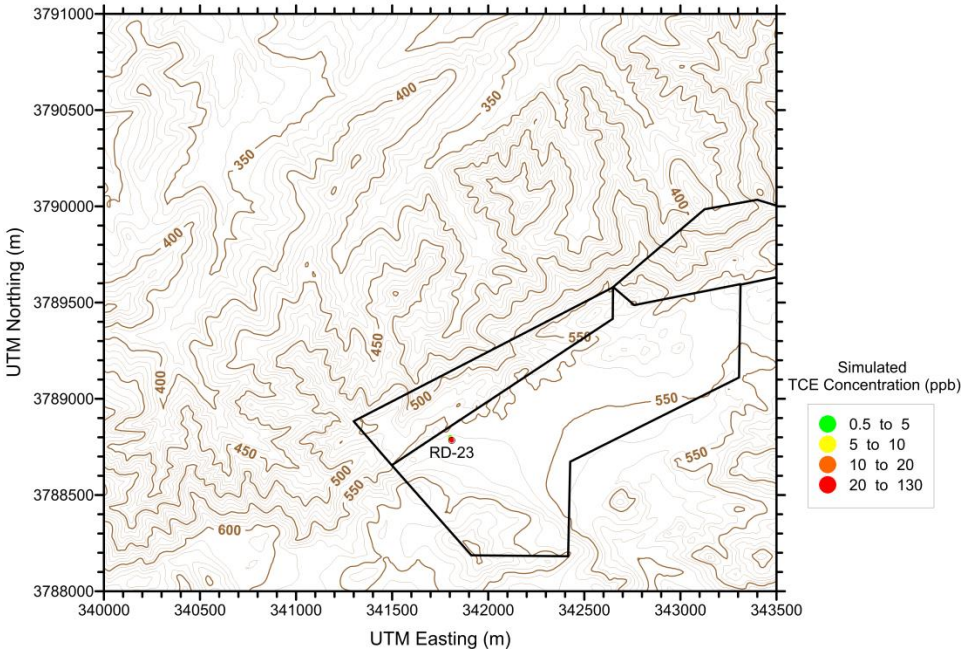

Figure 43: Simulated TCE concentrations 20 years post-release from a source at well RD-23. The particle track was truncated at simulated concentrations of less than 0.5 µg/L.

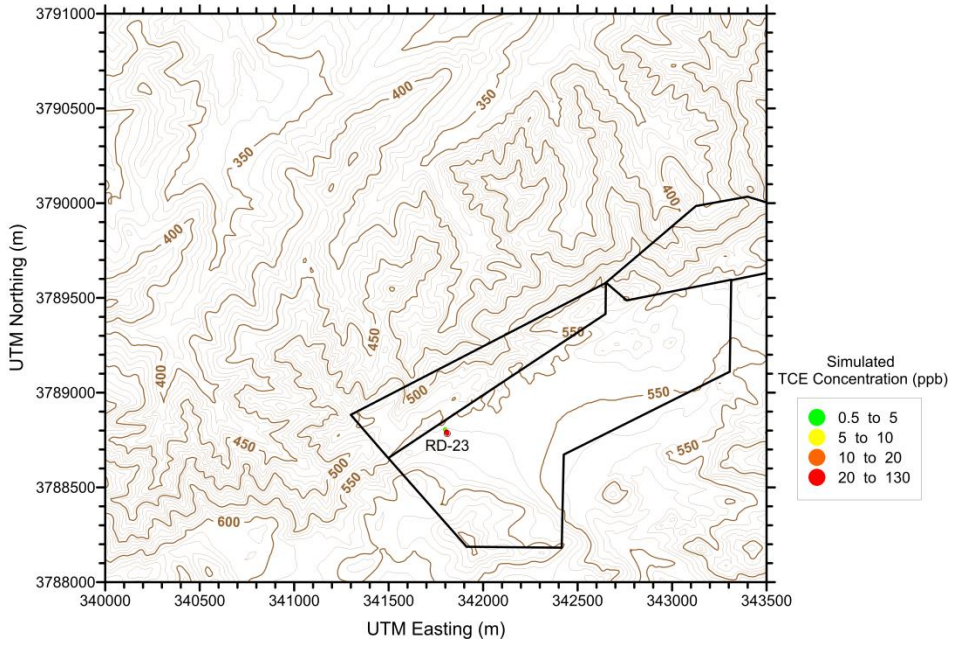

Figure 44: Simulated TCE concentrations 50 years post-release from a source at well RD-23. The particle track was truncated at simulated concentrations of less than 0.5 µg/L.

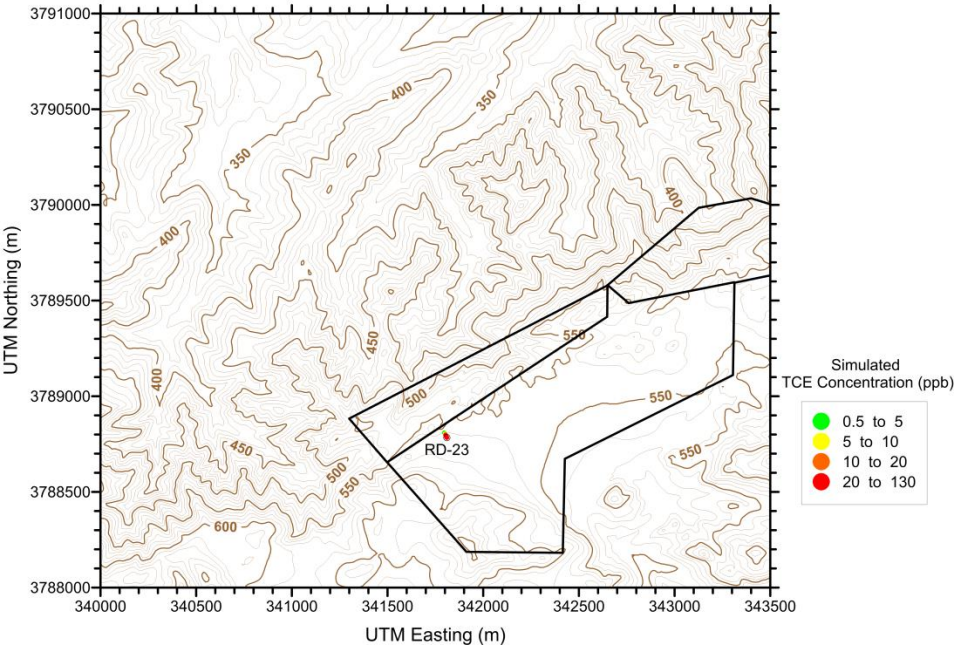

Figure 45: Simulated TCE concentrations 100 years post-release from a source at well RD-23. The particle track was truncated at simulated concentrations of less than 0.5 µg/L.

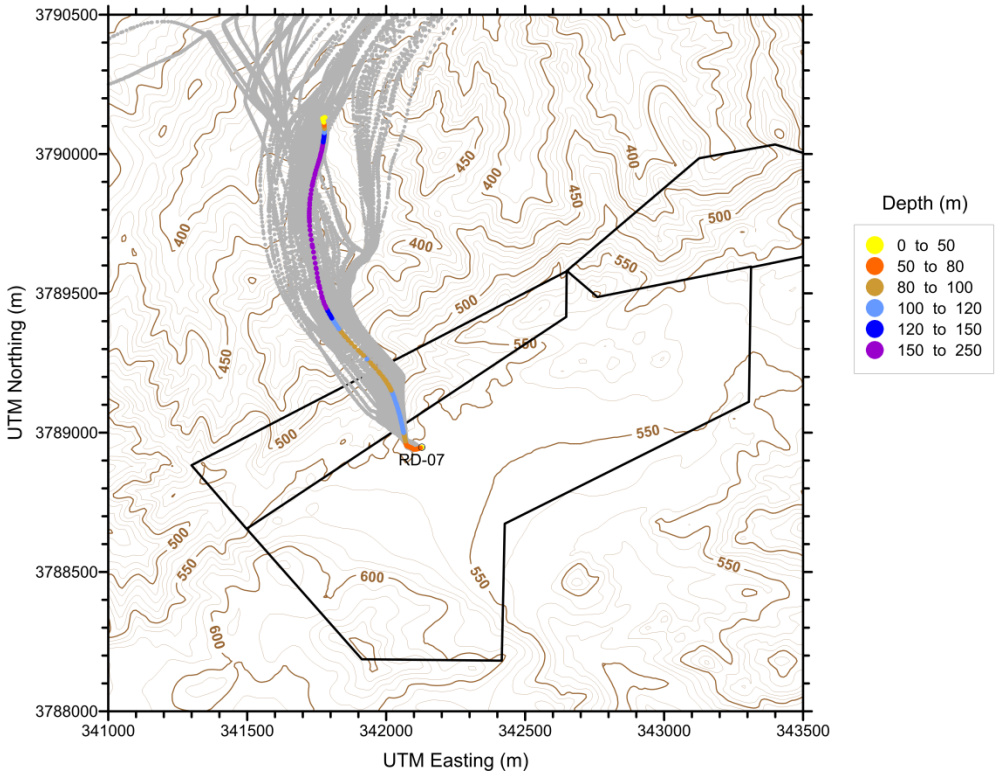

Figure 46: Simulated groundwater flow path with depth from well RD-07. Alternative flow paths from the null-space Monte Carlo analysis are shown in gray.

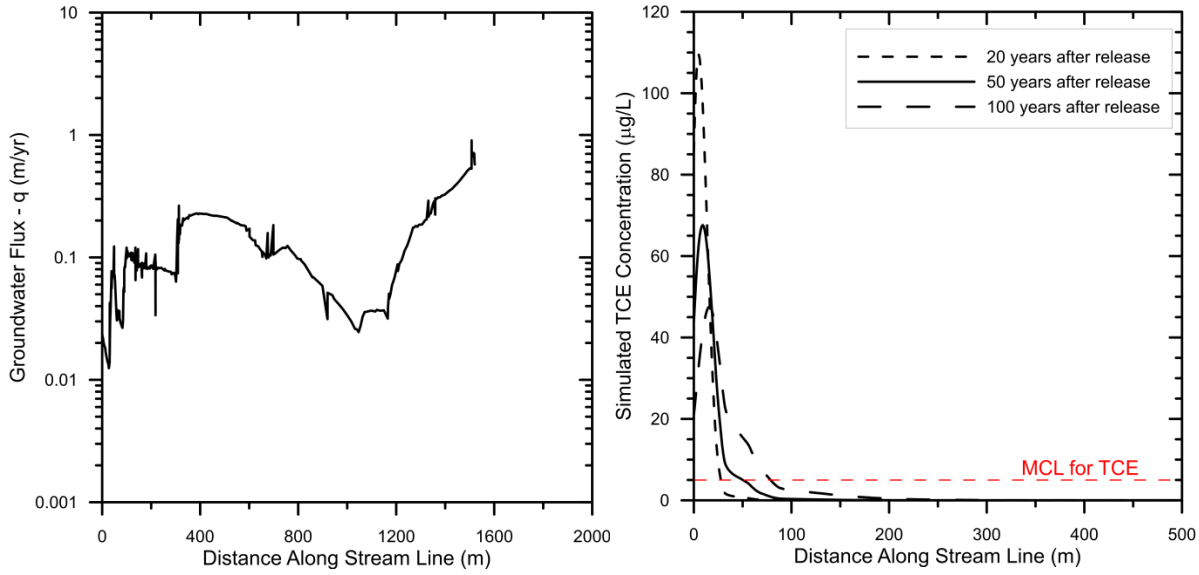

Figure 47: Simulated groundwater-flux profile and TCE-concentration profiles for three times following release along the flow path from well RD-07.

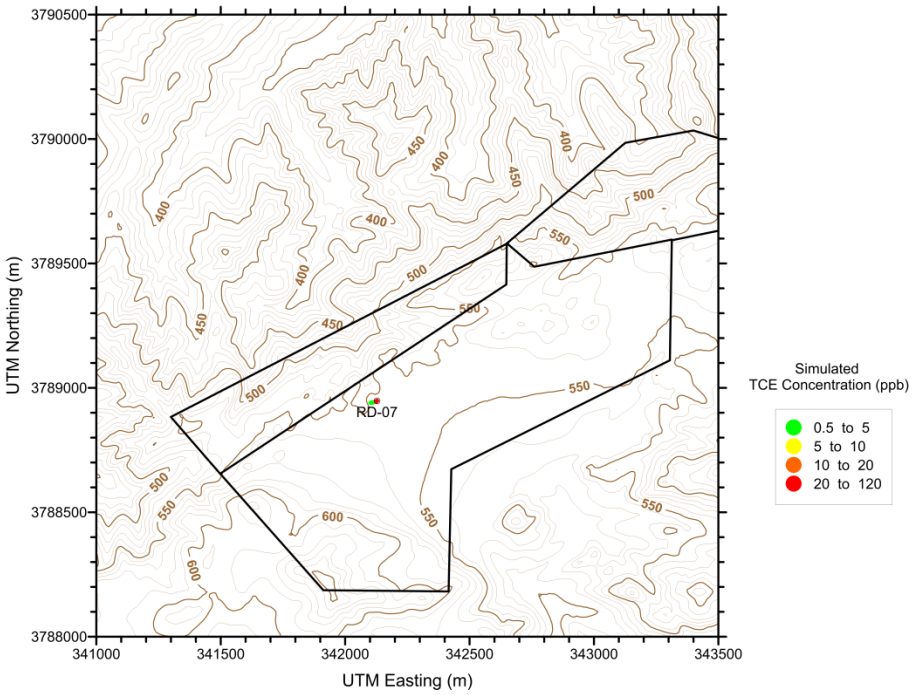

Figure 48: Simulated TCE concentrations 20 years post-release from well RD-07. The particle track was truncated at simulated concentrations of less than 0.5 µg/L.

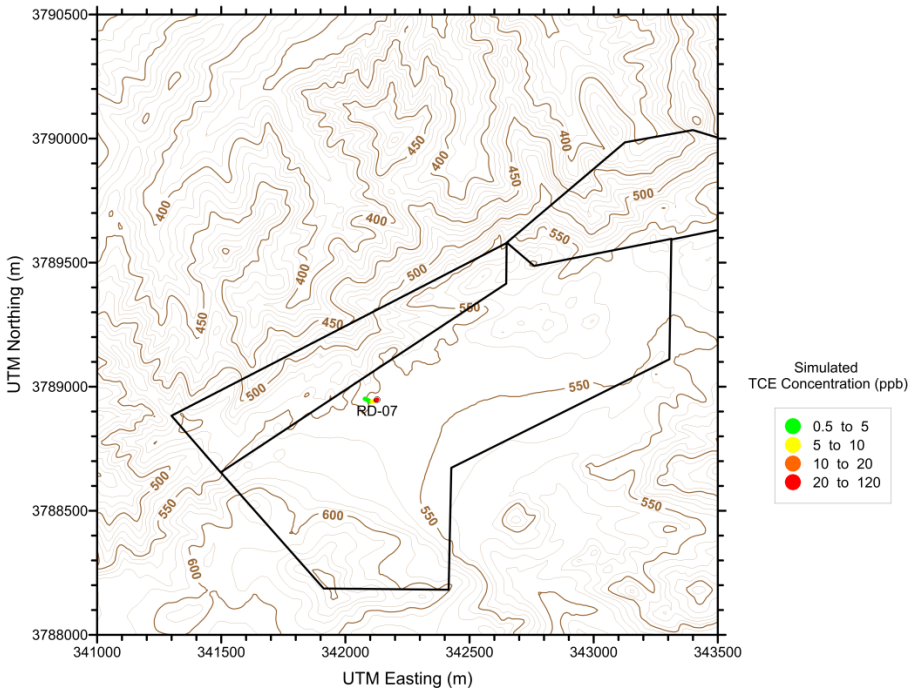

Figure 49: Simulated TCE concentrations 50 years post-release from a source at well RD-07. The particle track was truncated at simulated concentrations of less than 0.5 µg/L.

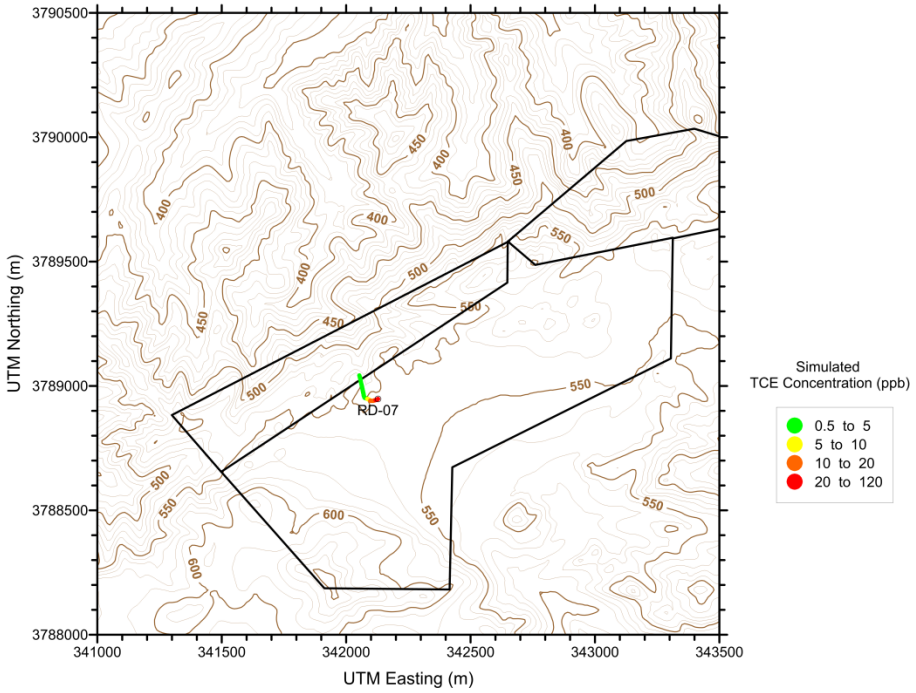

Figure 50: Simulated TCE concentrations 100 years post-release from a source at well RD-07. The particle track was truncated at simulated concentrations of less than 0.5 µg/L.

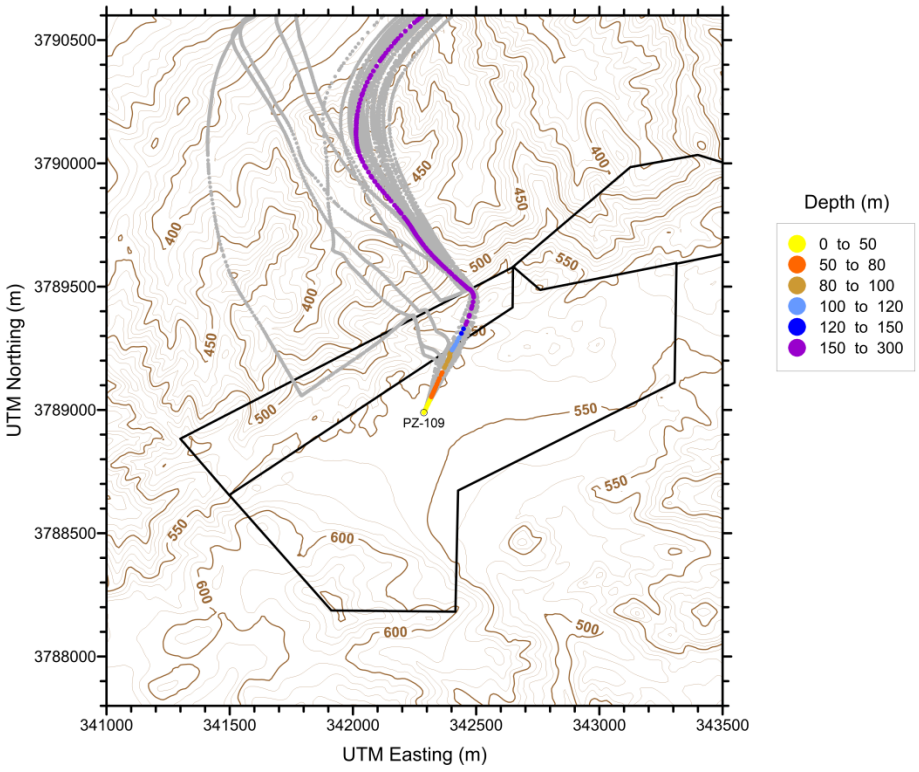

Figure 51: Simulated groundwater flow path with depth from well PZ-109. Alternative flow paths from the null-space Monte Carlo analysis are shown in gray.

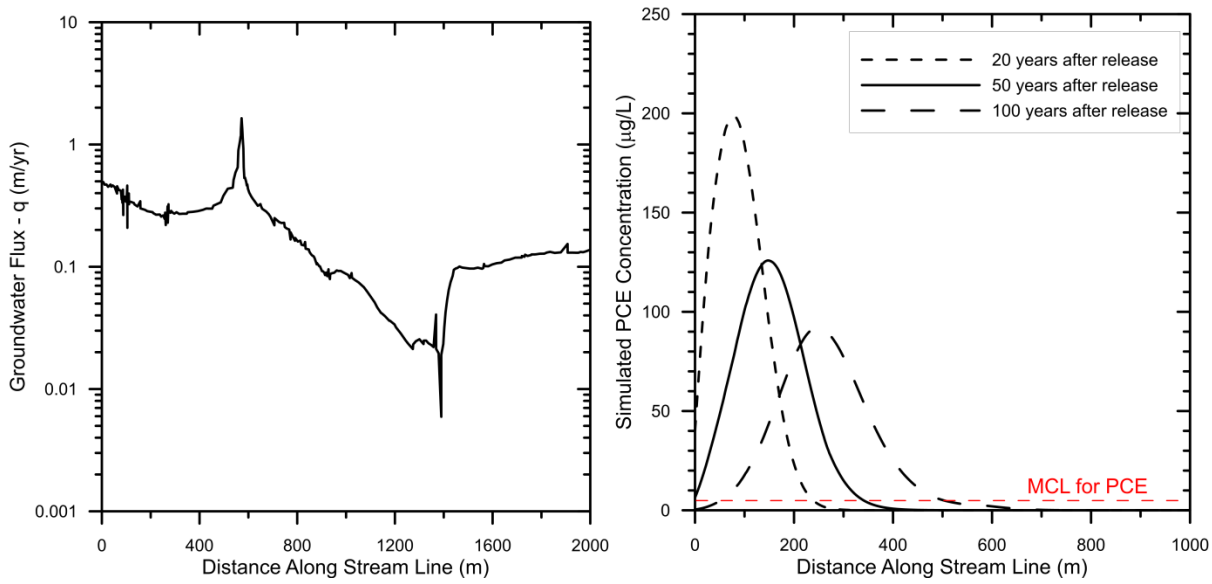

Figure 52: Simulated groundwater-flux profile and PCE-concentration profiles for three times following release along the flow path from well PZ-109.

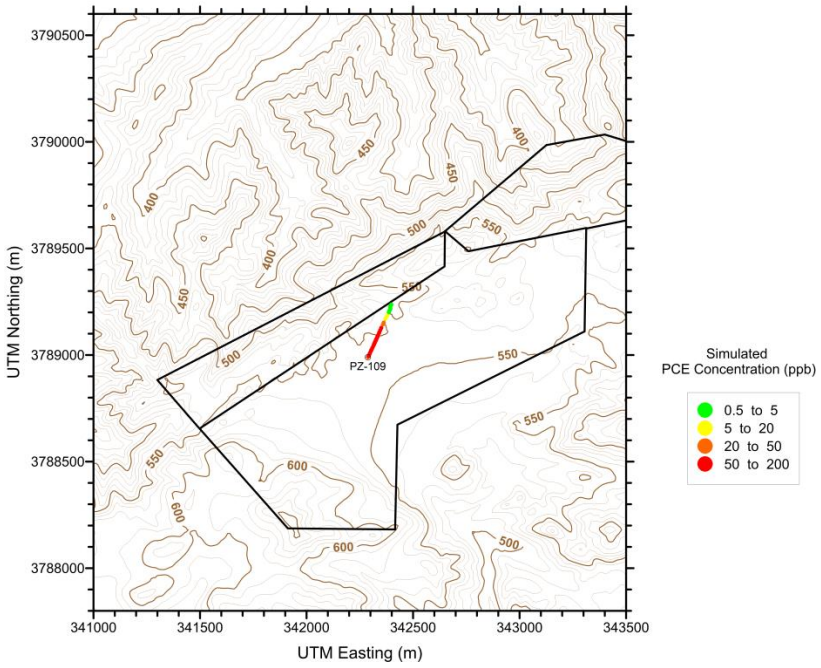

Figure 53: Simulated PCE concentrations 20 years post-release from a source at well PZ-109. The particle track was truncated at simulated concentrations of less than 0.5 µg/L.

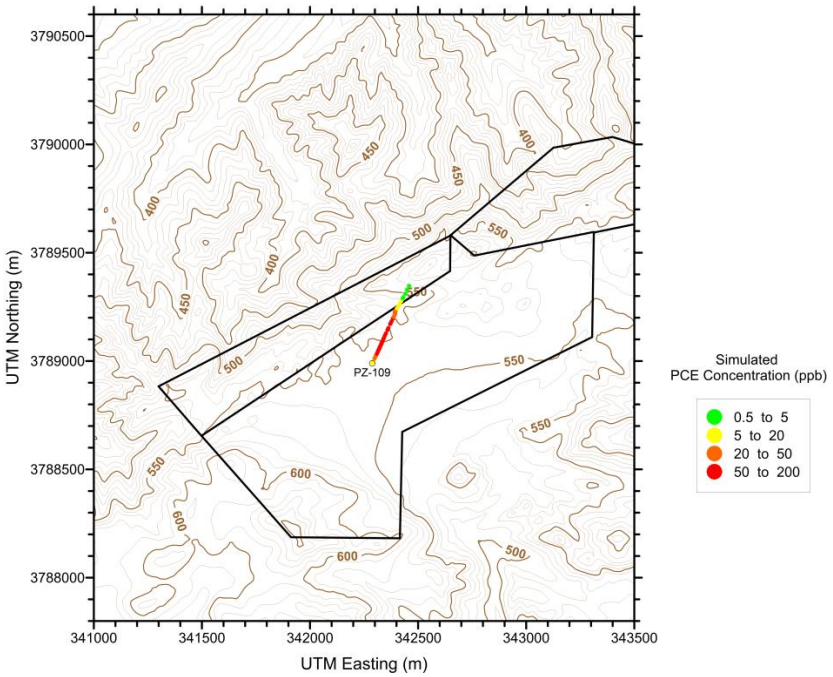

Figure 54: Simulated PCE concentrations 50 years post-release from a source at well PZ-109. The particle track was truncated at simulated concentrations of less than 0.5 µg/L.

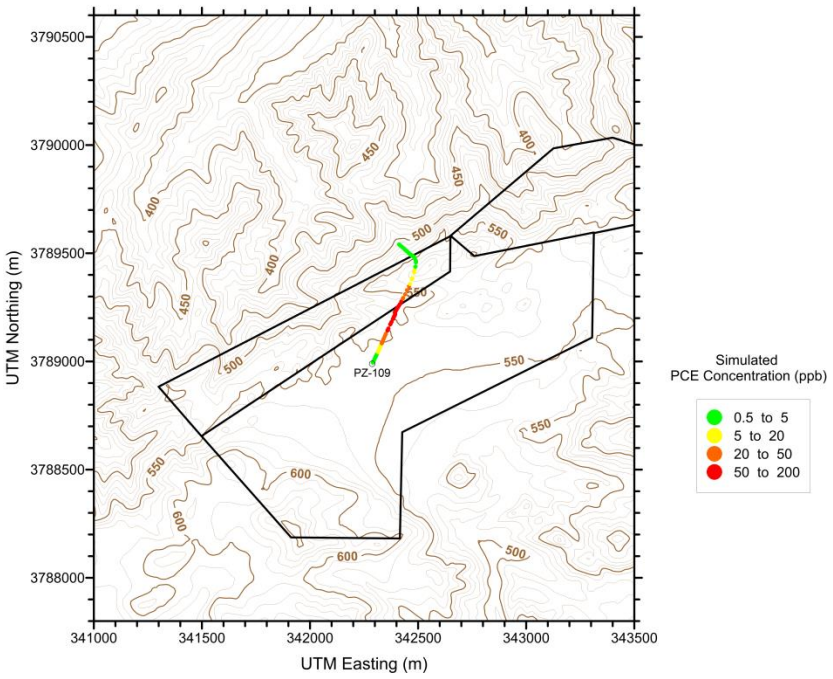

Figure 55: Simulated PCE concentrations 100 years post-release from a source at well PZ-109. The particle track was truncated at simulated concentrations of less than 0.5 µg/L.

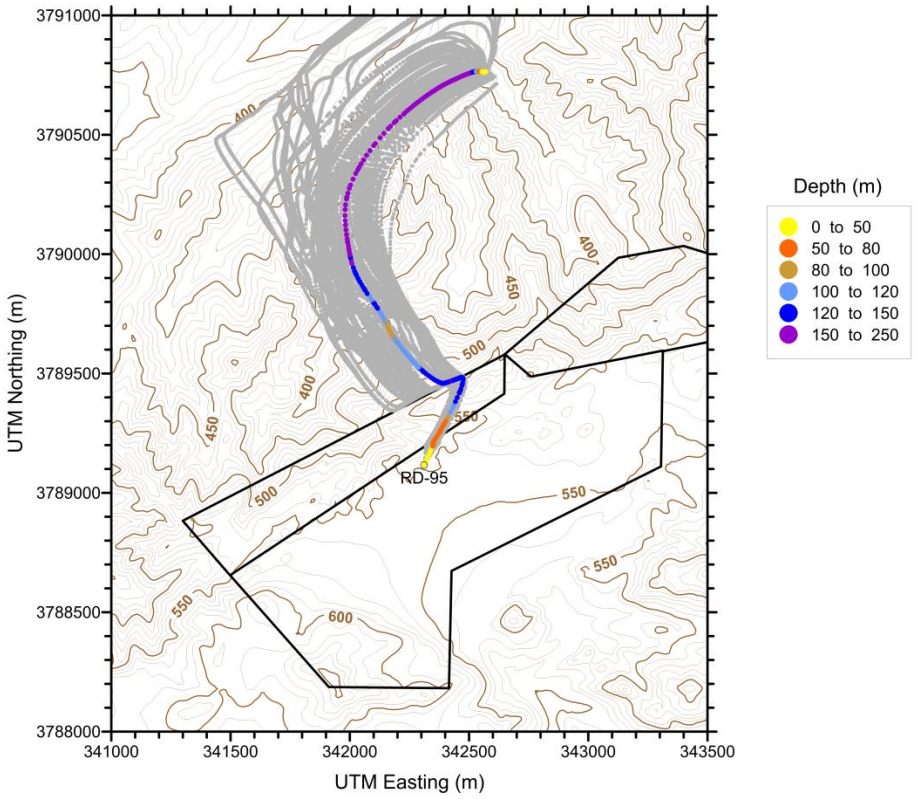

Figure 56: Simulated groundwater flow path with depth from well RD-95. Alternative flow paths from the null-space Monte Carlo analysis are shown in gray.

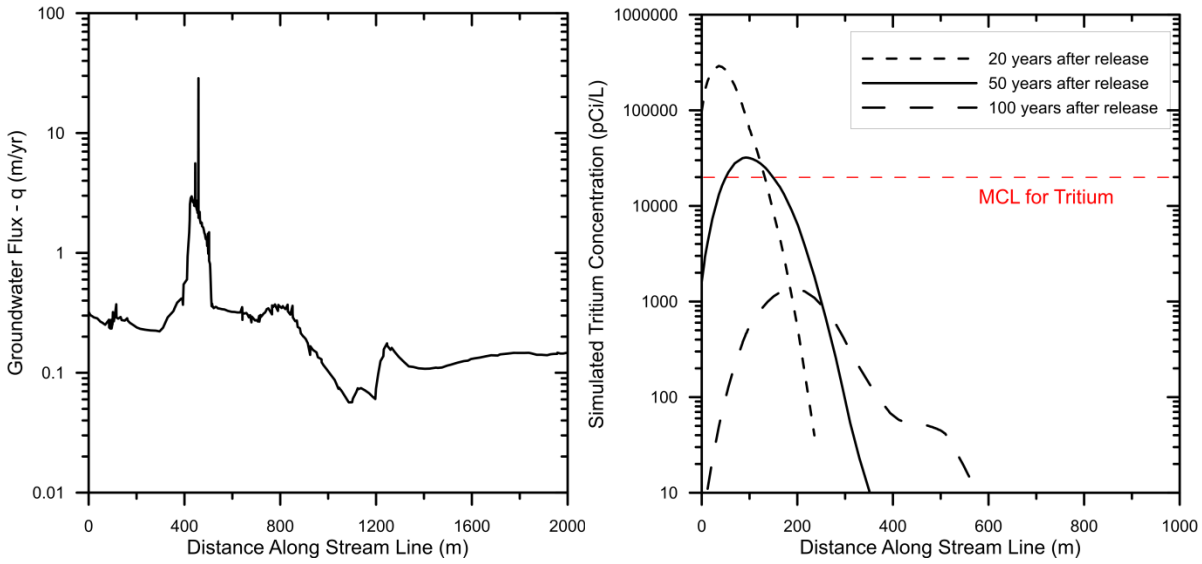

Figure 57: Simulated groundwater-flux profile and tritium-concentration profiles for three times following release along the flow path from well RD-95.

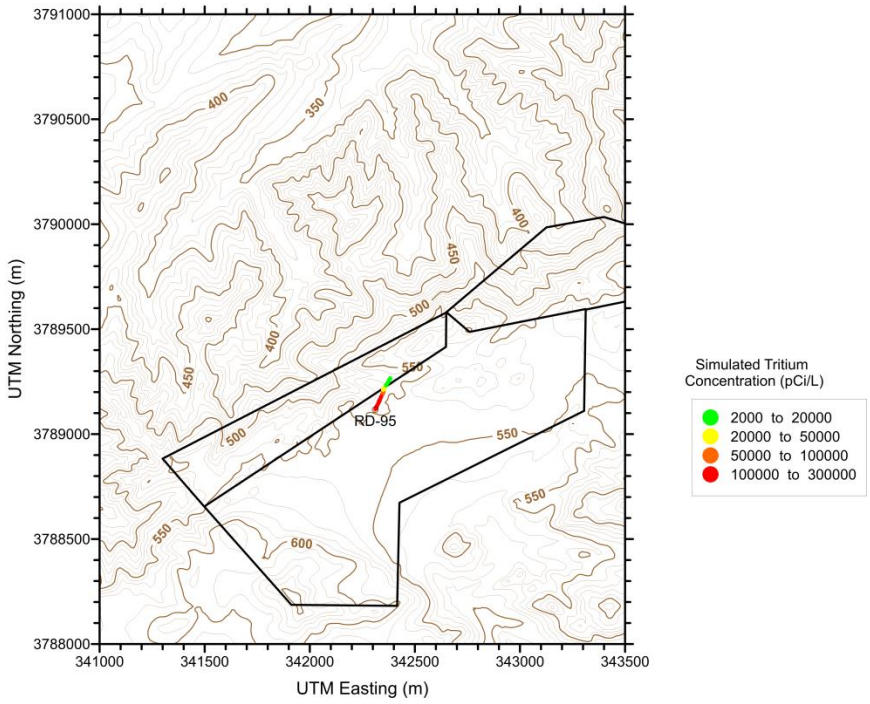

Figure 58: Simulated tritium concentrations 20 years post-release from a source at well RD-95. The particle track was truncated at simulated concentrations of less than 2,000 pCi/L.

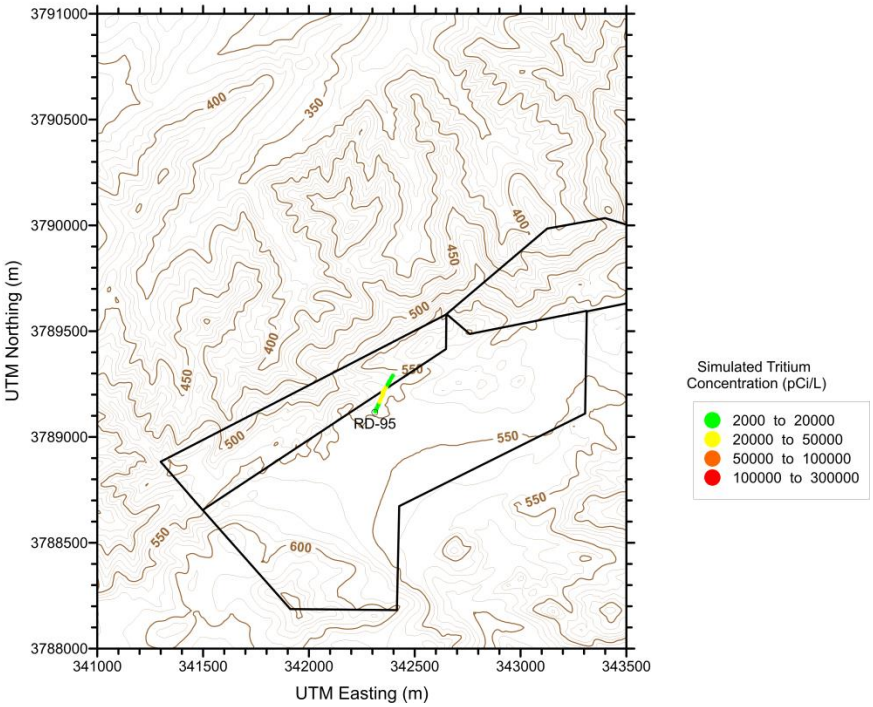

Figure 59: Simulated tritium concentrations 50 years post-release from a source at well RD-95. The particle track was truncated at simulated concentrations of less than 2,000 pCi/L.

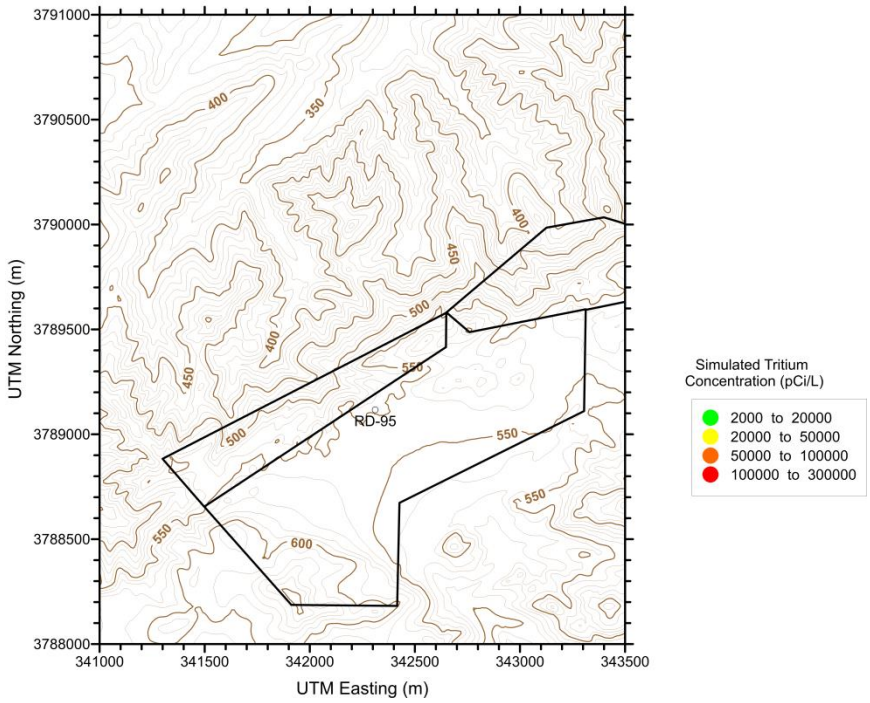

Figure 60: Simulated tritium concentrations 100 years post-release from a source at well RD-95. The particle track was truncated at simulated concentrations of less than 2,000 pCi/L (nowhere was it above this limit).

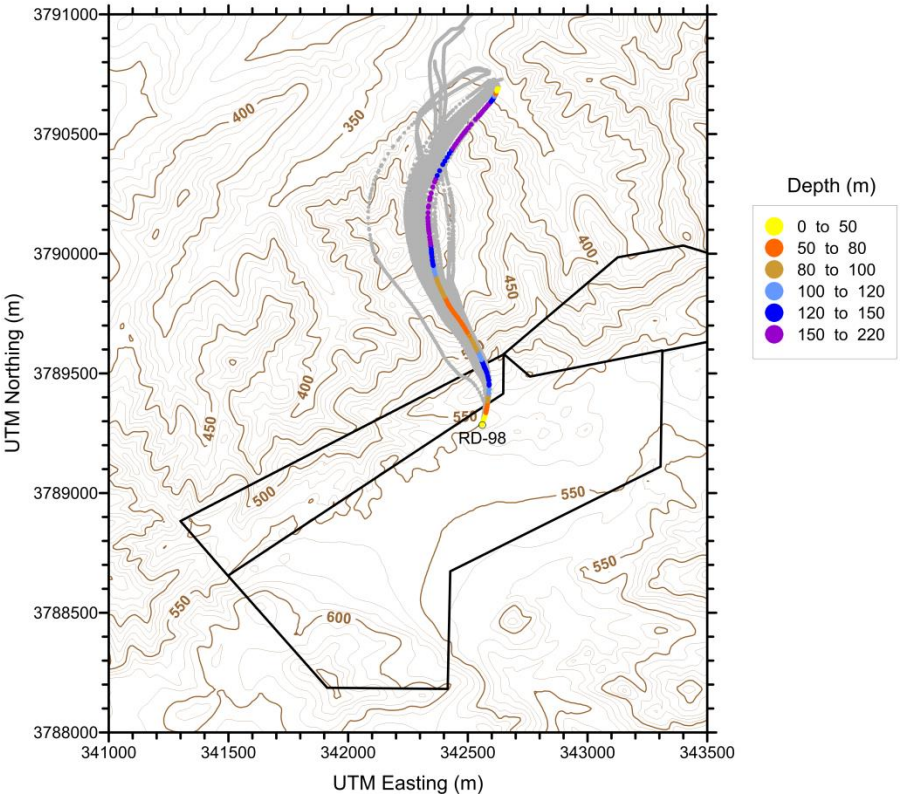

Figure 61: Simulated groundwater flow path with depth from well RD-98. Alternative flow paths from the null-space Monte Carlo analysis are shown in gray.

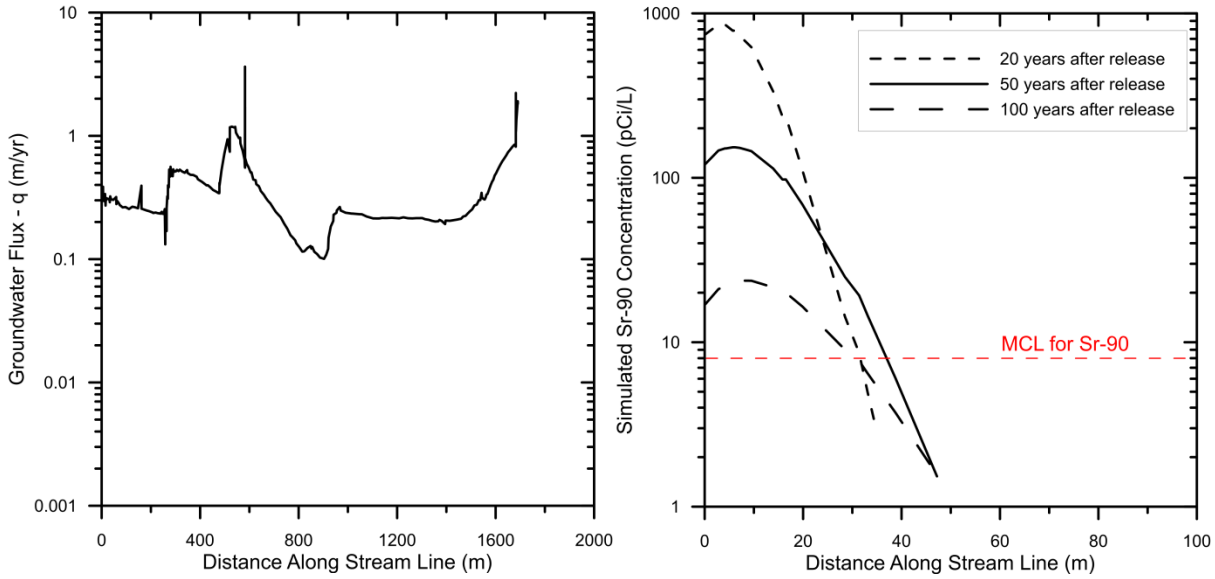

Figure 62: Simulated groundwater-flux profile and Sr-90-concentration profiles for three times following release along the flow path from well RD-98.

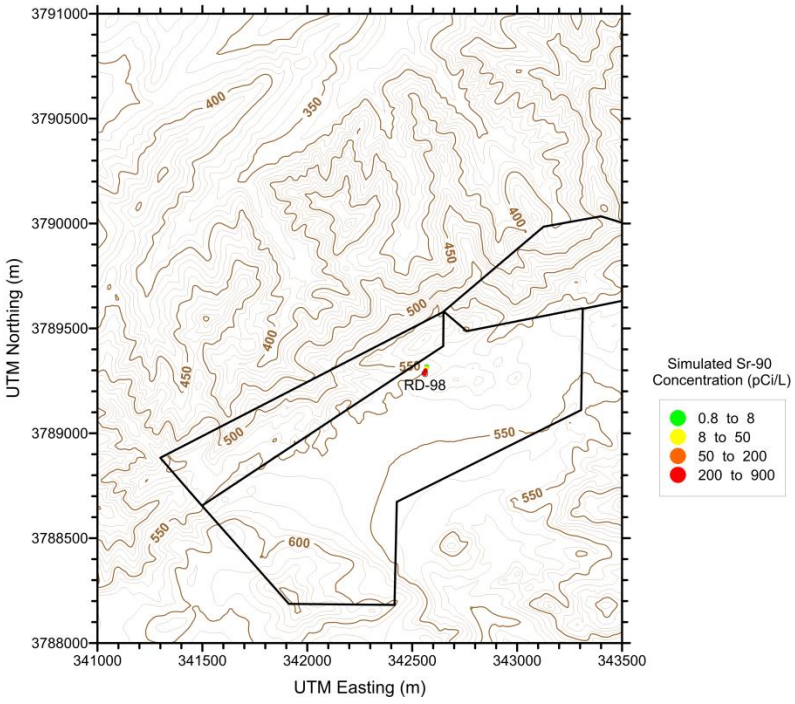

Figure 63: Simulated Sr-90 concentrations 20 years post-release from a source at well RD-98. The particle track was truncated at simulated concentrations of less than 0.8 pCi/L.

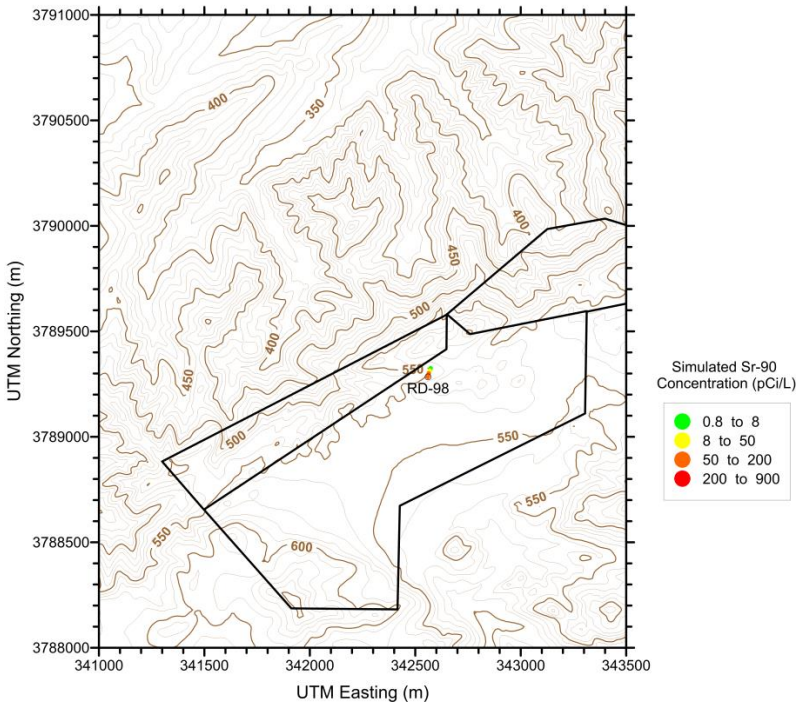

Figure 64: Simulated Sr-90 concentrations 50 years post-release from a source at well RD-98. The particle track was truncated at simulated concentrations of less than 0.8 pCi/L.

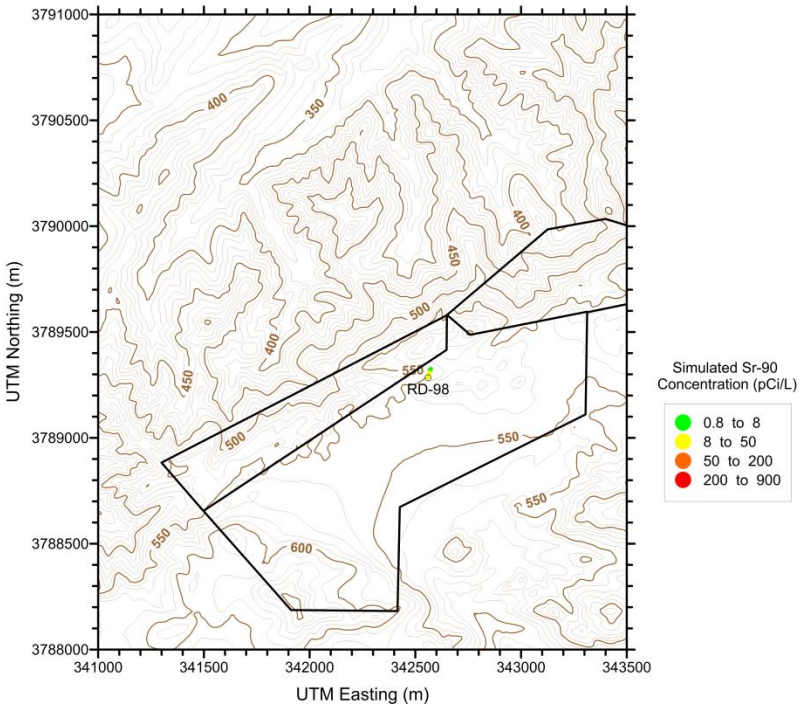

Figure 65: Simulated Sr-90 concentrations 100 years post-release from a source at well RD-98. The particle track was truncated at simulated concentrations of less than 0.8 pCi/L.

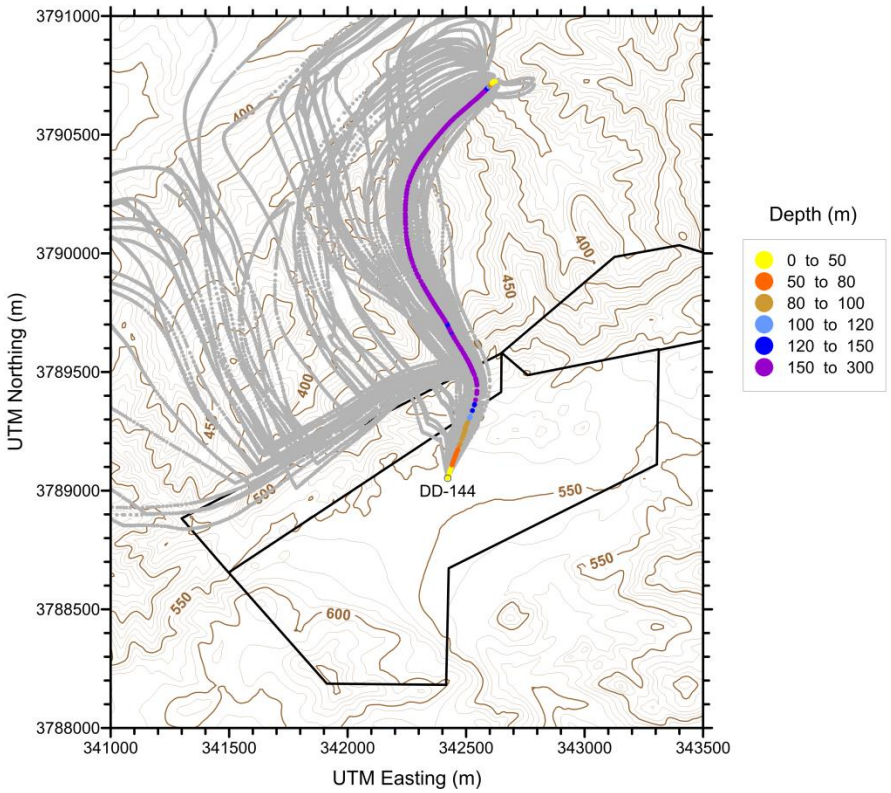

Figure 66: Simulated groundwater flow path with depth from well DD-144. Alternative flow paths from the null-space Monte Carlo analysis are shown in gray.

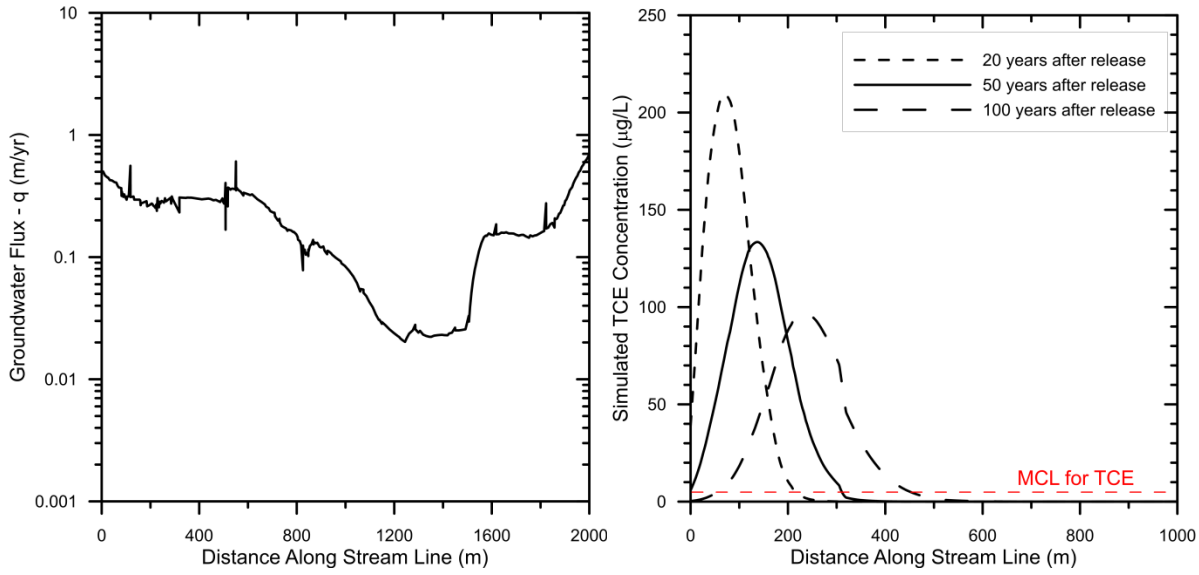

Figure 67: Simulated groundwater-flux profile and TCE-concentration profiles for three times following release along the flow path from well DD-144.

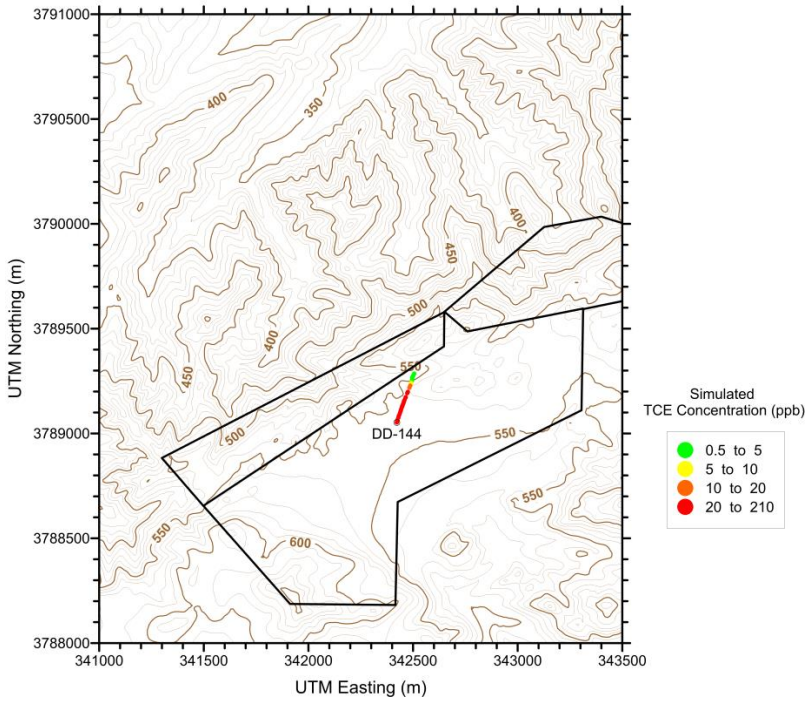

Figure 68: Simulated TCE concentrations 20 years post-release from a source at well DD-144. The particle track was truncated at simulated concentrations of less than 0.5 µg/L.

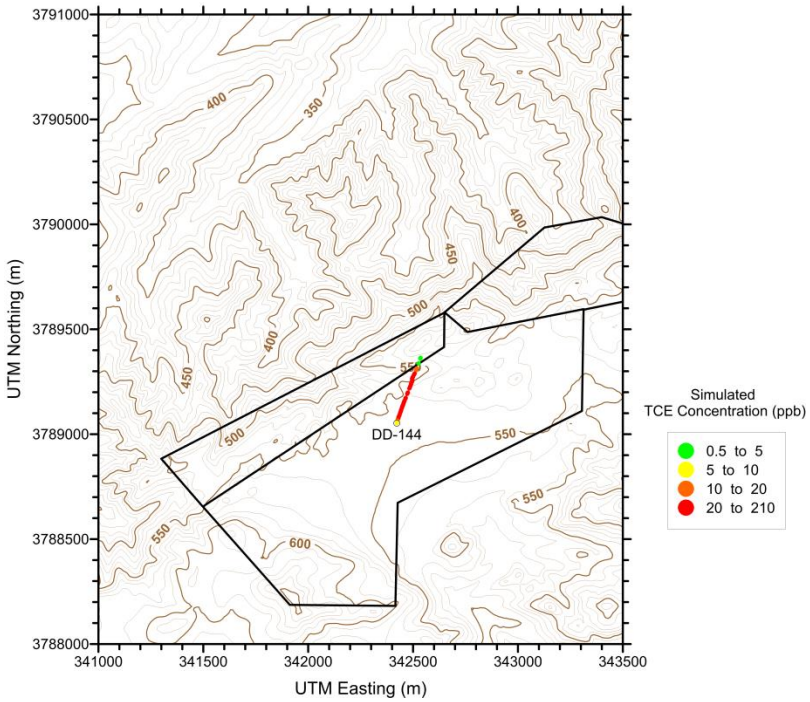

Figure 69: Simulated TCE concentrations 50 years post-release from a source at well DD-144. The particle track was truncated at simulated concentrations of less than 0.5 µg/L.

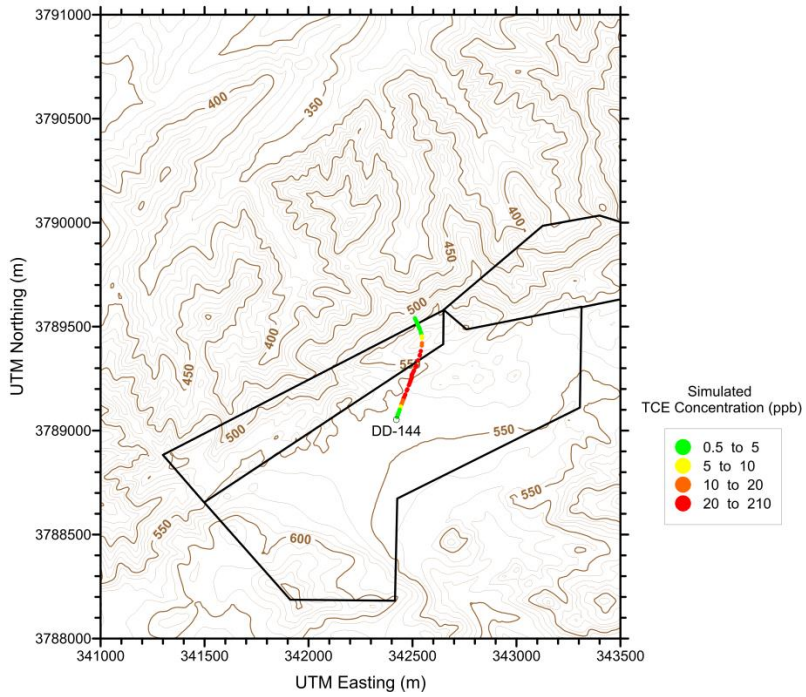

Figure 70: Simulated TCE concentrations 100 years post-release from a source at well DD-144. The particle track was truncated at simulated concentrations of less than 0.5 µg/L.

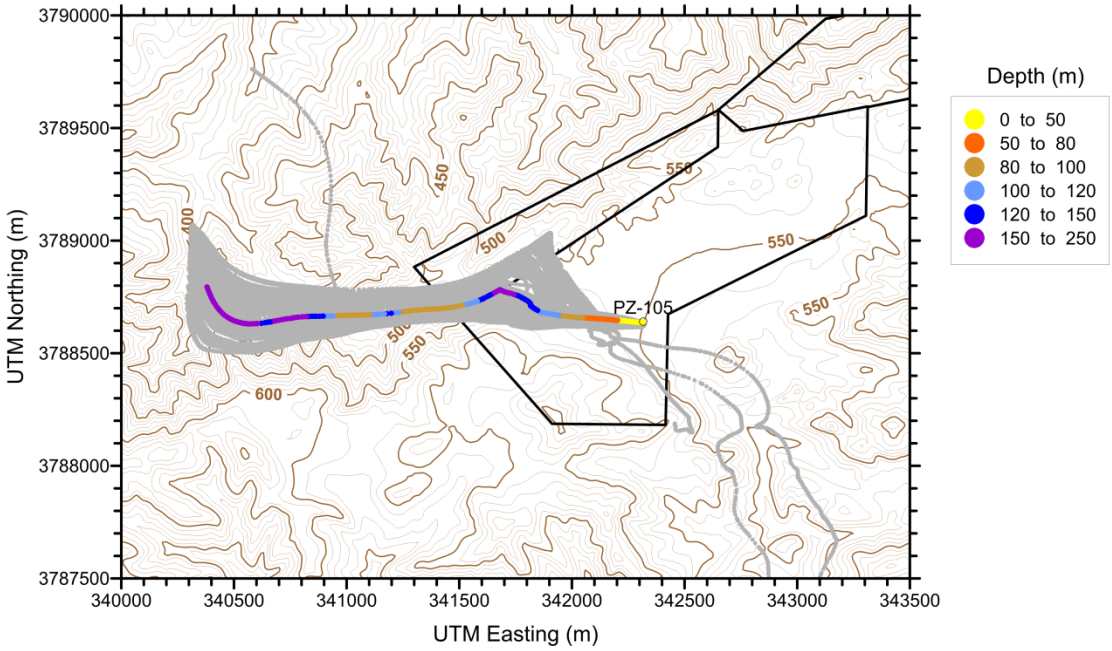

Figure 71: Simulated groundwater flow path with depth well PZ-105. Alternative flow paths from the null-space Monte Carlo analysis are shown in gray.

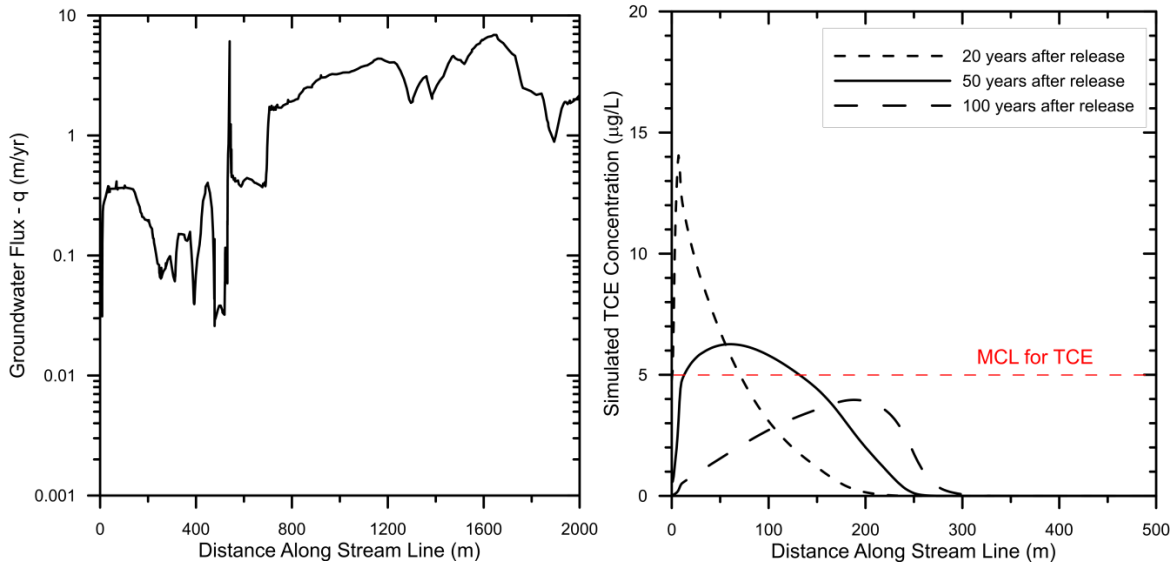

Figure 72: Simulated groundwater-flux profile and TCE-concentration profiles for three times following release along the flow path from well PZ-105.

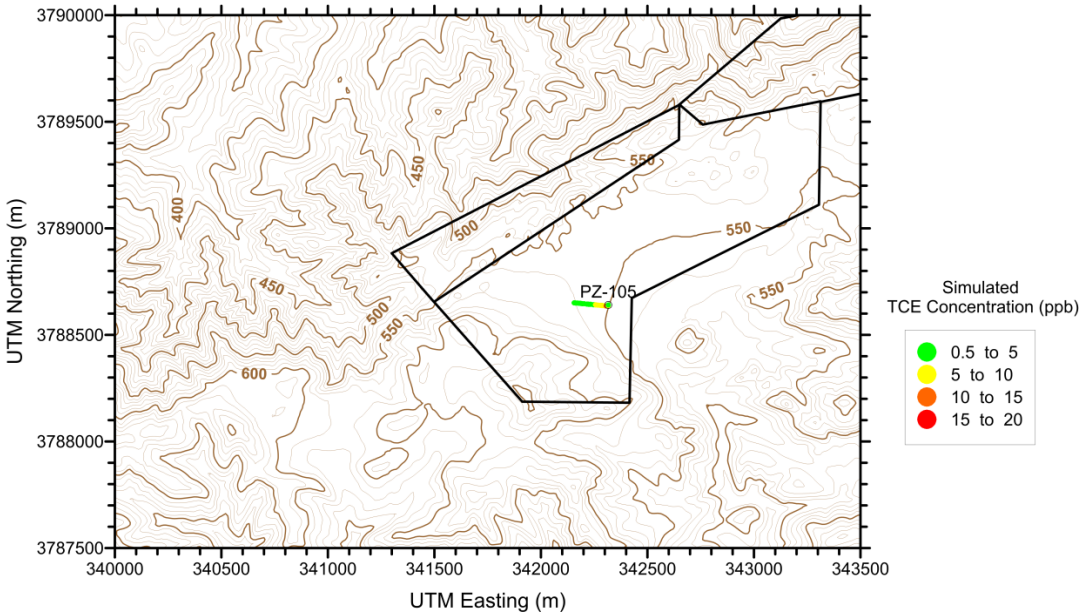

Figure 73: Simulated TCE concentrations 20 years post-release from a source at well PZ-105. The particle track was truncated at simulated concentrations of less than 0.5 µg/L.

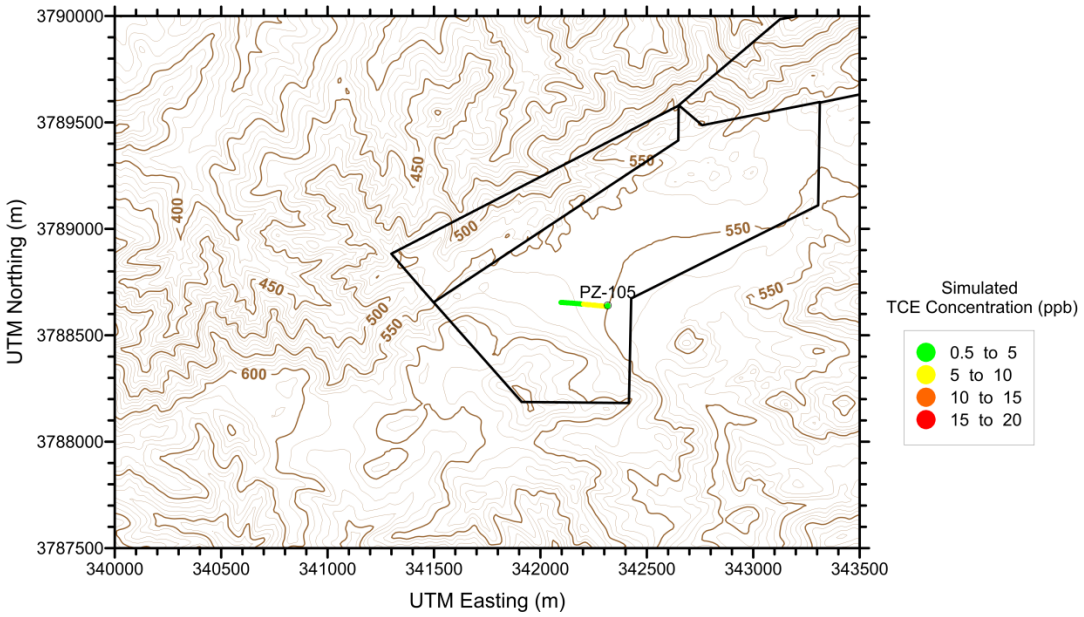

Figure 74: Simulated TCE concentrations 50 years post-release from a source at well PZ-105. The particle track was truncated at simulated concentrations of less than 0.5 µg/L.

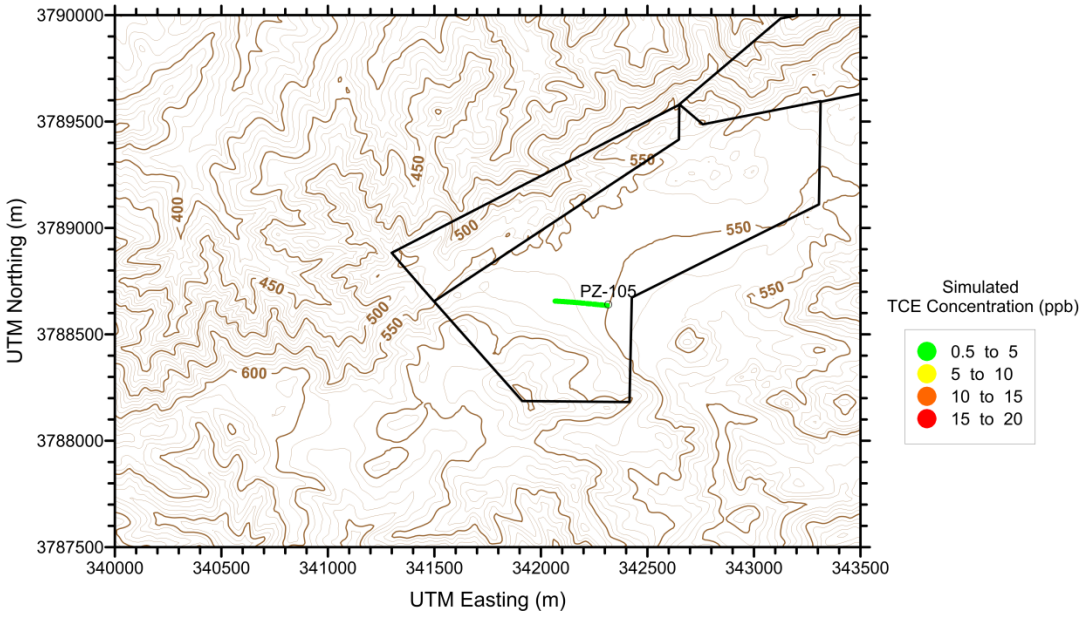

Figure 75: Simulated TCE concentrations 100 years post-release from a source at well PZ-105. The particle track was truncated at simulated concentrations of less than 0.5 µg/L.

4.7 NSMC Contaminant Transport

The 1-D contaminant transport model was developed and linked to the mountain-scale groundwater flow model to provide reasonable estimates of the extent and direction of contaminant migration along flow paths from key source locations in Area IV. The contaminant transport simulations accounted for important physical and chemical processes relevant to contaminant nature and extent, including advection, dispersion, matrix diffusion, potential sorption, and decay. Limitations and simplifications in

the mountain-scale flow model and the 1-D transport model placed some restrictions on the spatial resolution and precision of modeling results. Modeling results were also based on the assumption that relevant hydrogeological features have been identified and implemented in the mountain-scale flow model. However, the modeling results are appropriate for use in the general interpretation of the groundwater system and planning of potential remedial actions and monitoring.

The 1-D contaminant transport model results indicated that groundwater contamination in Area IV has migrated on the scale of tens of meters to hundreds of meters in the approximately 50 years since most contaminant releases occurred, depending on the location and contaminant. This conclusion is broadly consistent with observations from well sampling and the spatial distribution of groundwater contamination. Furthermore, the model results suggest that further migration of groundwater contamination exceeding MCLs over the next 50 years would be limited to a maximum of several hundred meters, even in the absence of intervention. Further migration from some locations could be significantly less than hundreds of meters.

The transport modeling results showed that maximum contaminant concentrations are expected to decline with time in the groundwater, assuming no additional inputs of contaminant mass from the vadose zone. The simulated maximum concentrations in the tritium plume were projected to fall below the MCL within 50 years. The transport model results indicated that the maximum TCE concentrations would fall below the MCL for some locations such as PZ-105 that currently have relatively low contaminant concentrations. In the absence of chemical degradation or sorption of TCE and PCE, as assumed in the 1-D contaminant transport model, contaminant concentrations in groundwater were not simulated to fall below the MCL within 50 years at any of the locations modeled, assuming no further remedial actions.

4.7.1 Horsetail Plots of Contaminant Concentration Profiles

Each of the 100 NSMC flow realizations was used in the FEHM transport model to develop concentration profiles along the corresponding flow path. Transport simulations were not conducted for wells DD-140, DD-145, or RD-54A because these wells have low contaminant concentrations. For well DD-144, TCE concentrations at 20, 50, and 100 years are shown in Figure 76(a) without decay and (b) with first-order degradation (right). First-order degradation rates of PCE (0.11/yr) and TCE (0.18/yr) calculated for chlorinated solvents at the SSFL were used. Note that after 100 yrs concentrations with chemical degradation are so low as to be well below the MCL for many wells. Figure 77 and Figure 78 show PCE and TCE concentrations, respectively, from well PZ-109. Figure 79 shows TCE concentrations (a) without and (b) with first-order degradation from well RD-07. Figure 80 shows TCE concentrations (a) without and (b) with first-order degradation from well RD-21. Figure 81 shows TCE concentrations without (a) and with (b) first-order degradation from well RD-23. Figure 82 shows ^{3}H (12.32-yr half-life) concentrations from well RD-90. Figure 83 shows TCE concentrations without (a) and with (b) first-order degradation from well RD-91. Figure 84 shows ^{3}H (12.32-yr half-life) concentrations from well RD-95. Figure 85 shows ^{90}Sr (28.79-yr half-life) concentrations from well RD-98. Figure 86 shows TCE concentrations without (a) and with (b) first-order degradation from well RD-98.

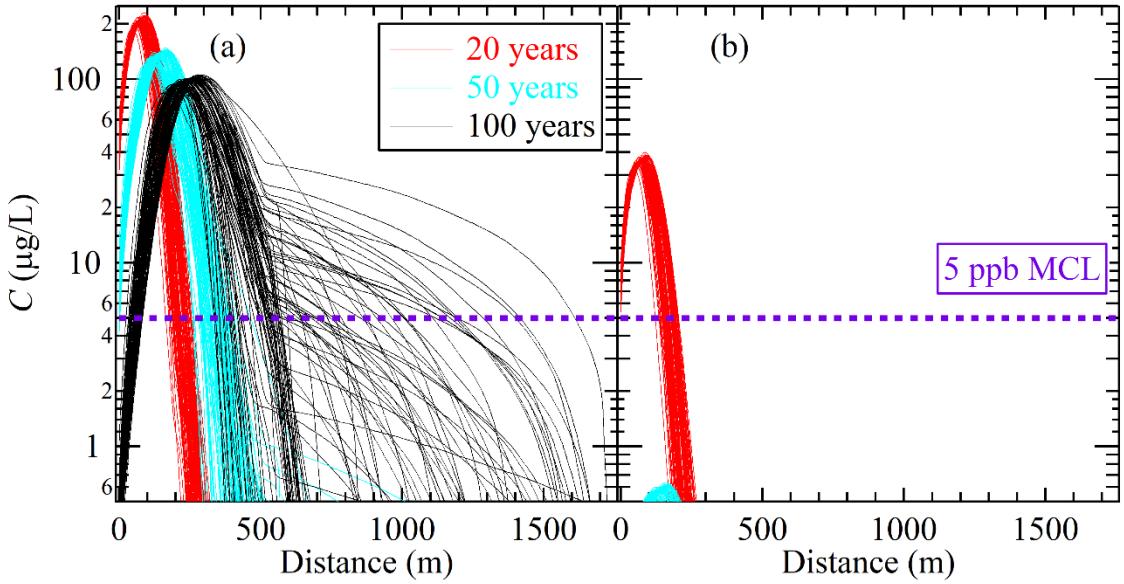

Figure 76: TCE concentration profiles along the 100 NSMC flow paths after 20 (red), 50 (turquoise), and 100 (black) years from well DD-144 (a) without decay and (b) with first-order degradation rate of 0.18/yr.

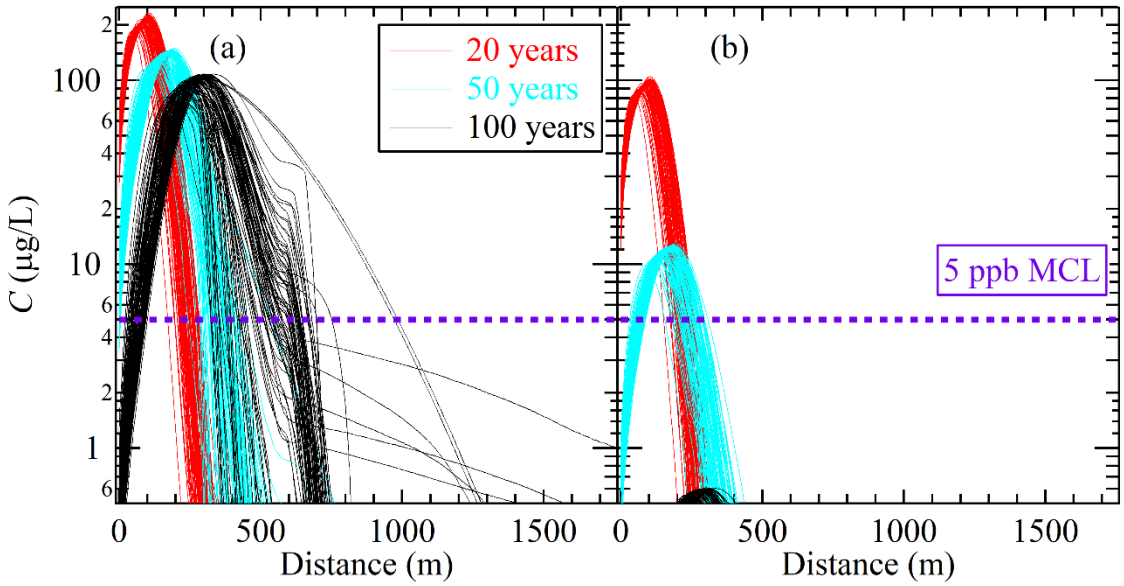

Figure 77: PCE concentration profiles along the 100 NSMC flow paths after 20 (red), 50 (turquoise), and 100 (black) years from well PZ-109 (a) without decay and (b) with first-order degradation rate of 0.11/yr.

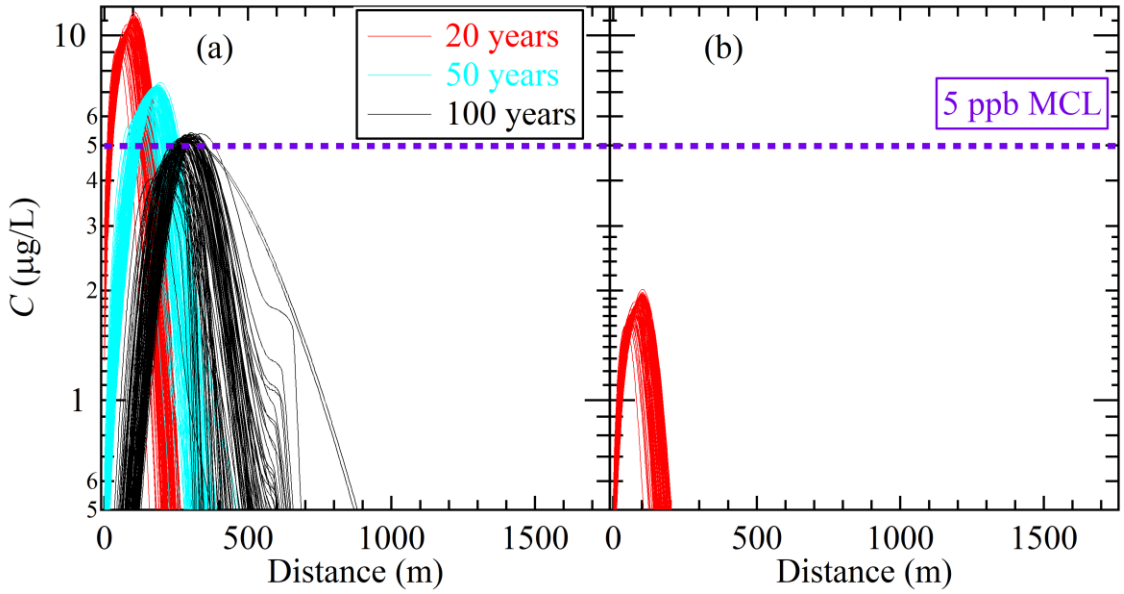

Figure 78: TCE concentration profiles along the 100 NSMC flow paths after 20 (red), 50 (turquoise), and 100 (black) years from well PZ-109 (a) without decay and (b) with first-order degradation rate of 0.18/yr.

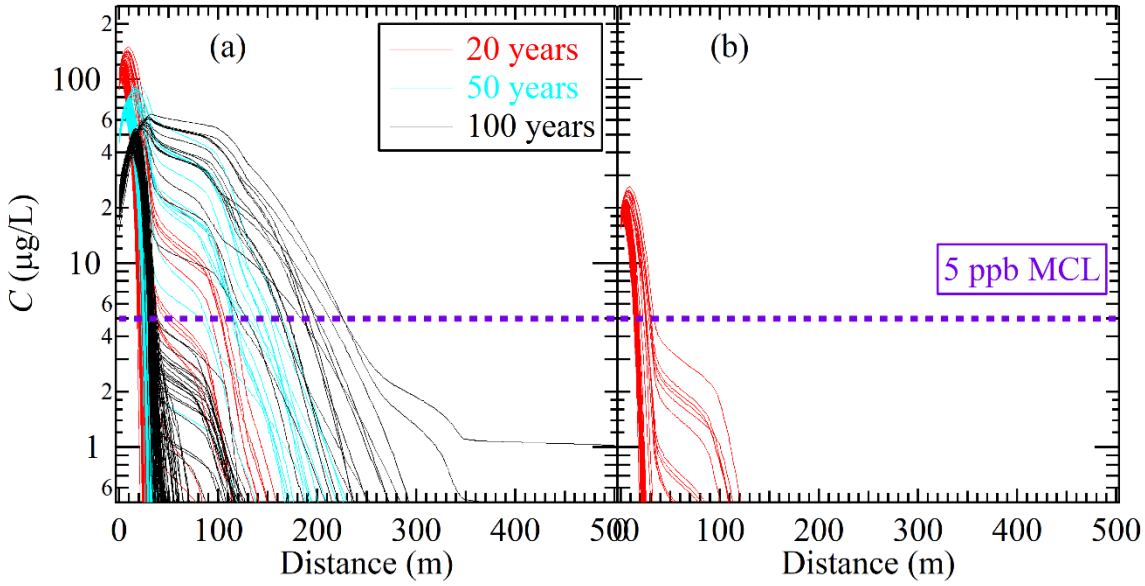

Figure 79: TCE concentration profiles along the 100 NSMC flow paths after 20 (red), 50 (turquoise), and 100 (black) years from well RD-07 (a) without decay and (b) with first-order degradation rate of 0.18/yr (right).

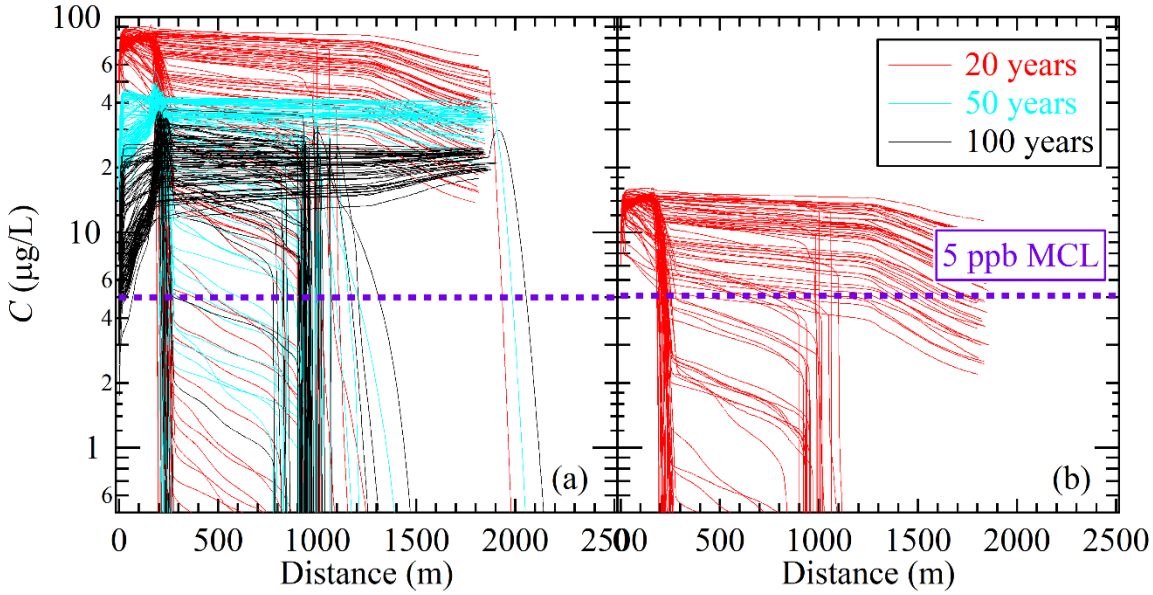

Figure 80: TCE concentration profiles along the 100 NSMC flow paths after 20 (red), 50 (turquoise), and 100 (black) years from well RD-21 (a) without decay and (b) with first-order degradation rate of 0.18/yr.

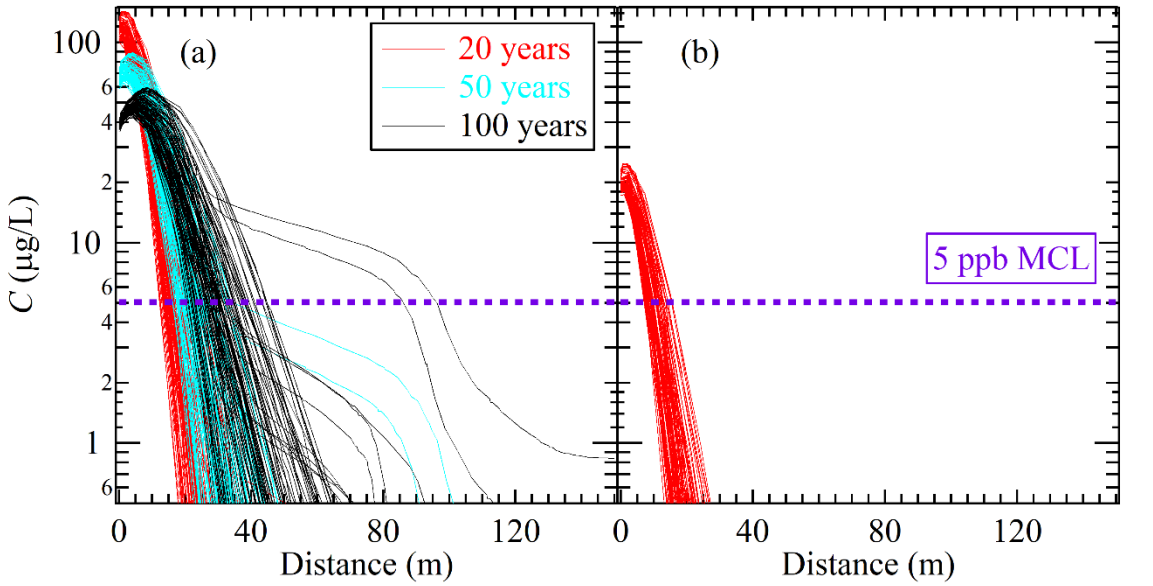

Figure 81: TCE concentration profiles along the 100 NSMC flow paths after 20 (red), 50 (turquoise), and 100 (black) years from well RD-23 (a) without decay and (b) with first-order degradation rate of 0.18/yr.

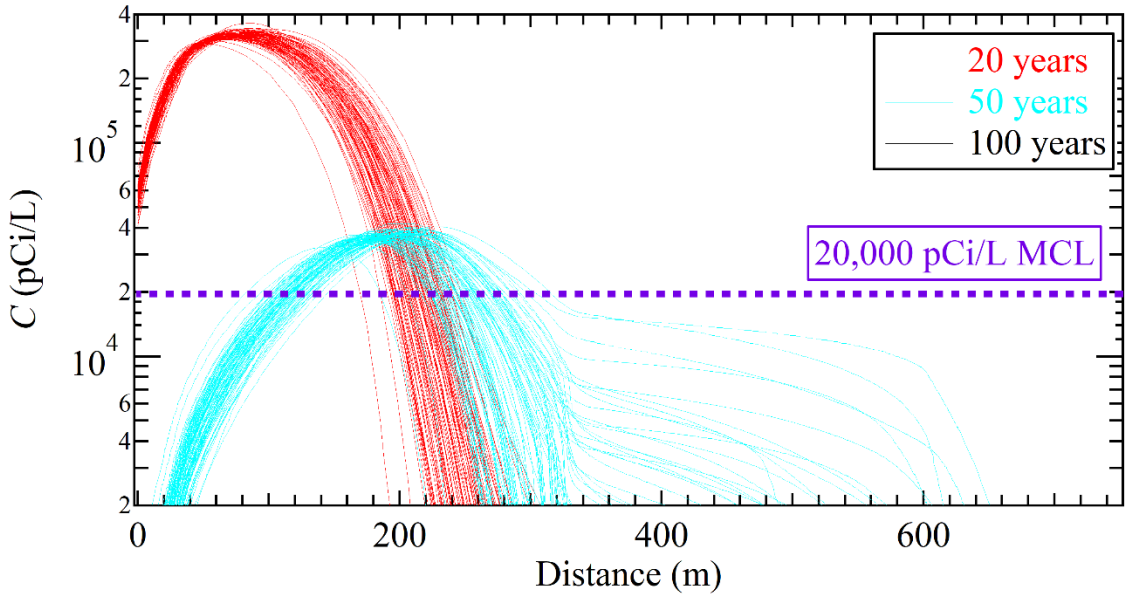

Figure 82: ^{3}H concentration profiles along the 100 NSMC flow paths after 20 (red), 50 (turquoise), and 100 (black) years from well RD-90 with a half-life of 12.32 yr.

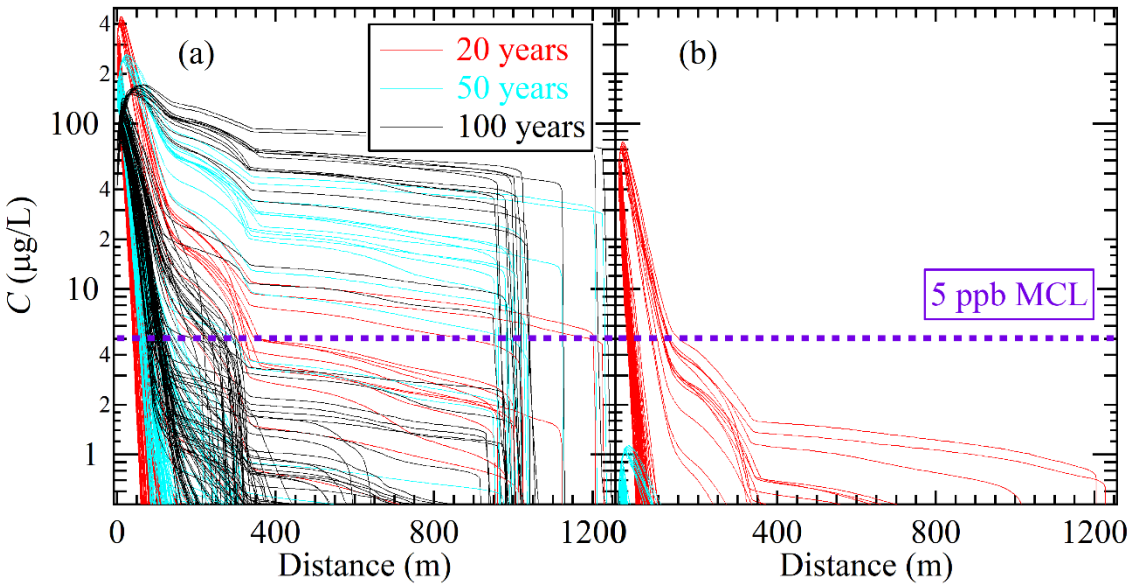

Figure 83: TCE concentration profiles along the 100 NSMC flow paths after 20 (red), 50 (turquoise), and 100 (black) years from well RD-91 (a) without decay and (b) with first-order degradation rate of 0.18/yr.

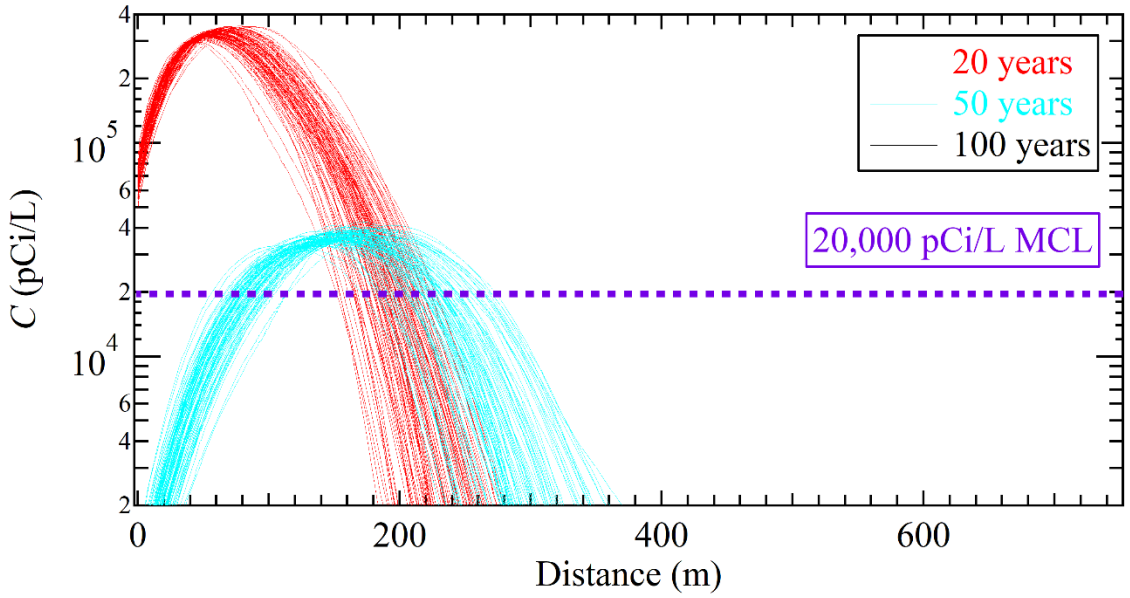

Figure 84: ^{3}H concentration profiles along the 100 NSMC flow paths after 20 (red), 50 (turquoise), and 100 (black) years from well RD-95 with a half-life of 12.32 yr.

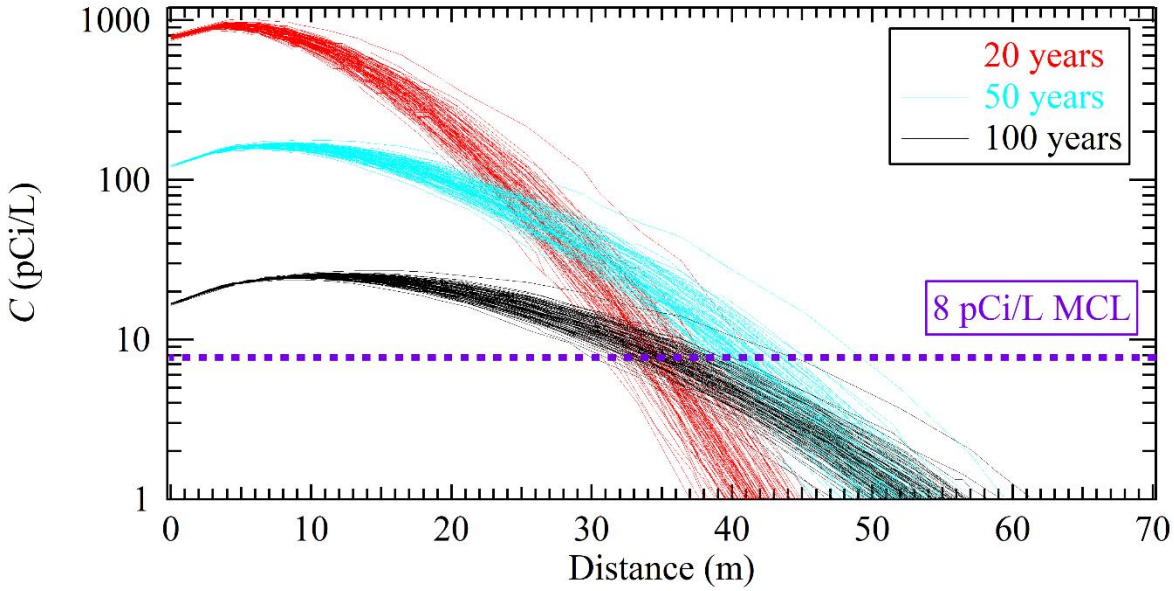

Figure 85: ^{90}Sr concentration profiles along the 100 NSMC flow paths after 20 (red), 50 (turquoise), and 100 (black) years from well RD-98 with a half-life of 28.79 yr. Note that the y axis is in log scale.

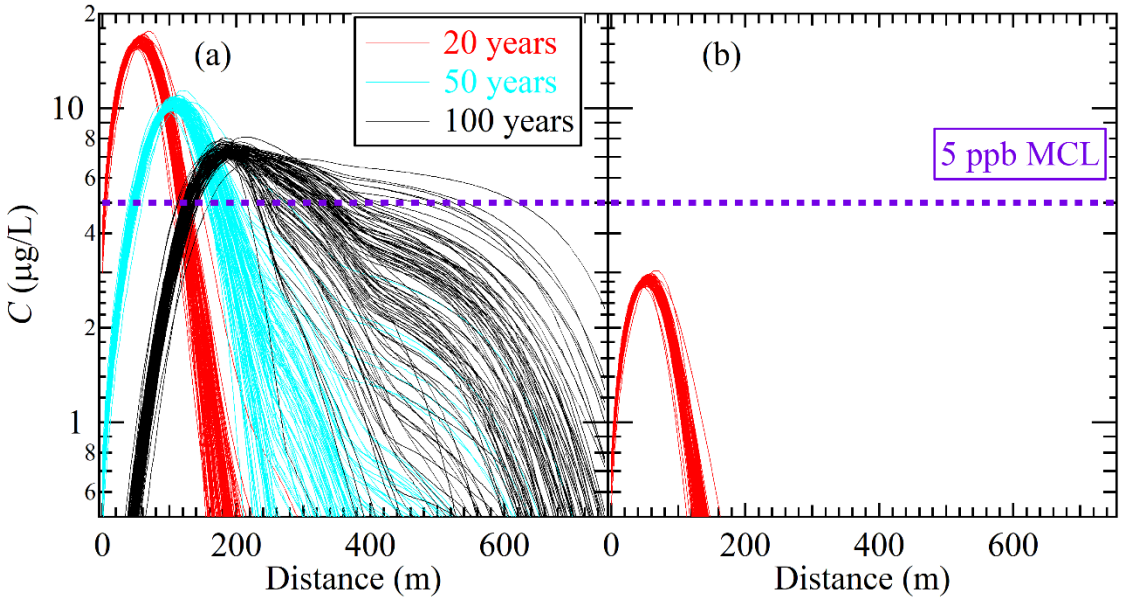

Figure 86: TCE concentration profiles along the 100 NSMC flow paths after 20 (red), 50 (turquoise), and 100 (black) years from well RD-98 (a) without decay and (b) with first-order degradation rate of 0.18/yr (right).

4.7.2 Discussion of Contaminant Transport Horsetail Plots

The MSGFM is a highly complex groundwater flow model. It has 1,244 parameters, 671 of which are adjustable (not tied or fixed). The calibration data set comprises 886 observations: 626 head observations (121 in Area IV), 219 head gradients (14 in Area IV), and 37 seeps (two in Area IV) with three seep ratios provided to ensure that relative flows exit the east, north, and south sides of the mountain appropriately. Given the limited information content in the calibration data set, only between 22 and 57 parameters are identifiable. This means that over 600 of the parameters are not informed by the calibration data set and are thus subject to significant uncertainty. In groundwater models of this complexity, none of this is surprising.

As PEST goes through the calibration process, it varies the adjustable parameters within the specified limits to minimize the objective function (weighted least squares difference between the calibration data set and its modeled equivalent). If a parameter is uninformed by the calibration data set, it is essentially unconstrained unless regularization has been implemented in PEST. Historically, regularization has not been used to calibrate the MSGFM. With regularization, if the parameter is unconstrained by the calibration data, it is assigned a default hydraulic conductivity specified through expert judgment.

During calibration, PEST appropriately minimized the objective function such that observed heads, head gradients, and seeps were honored by the model, especially in Area IV. However, nowhere in the calibration was information supplied about specific discharge, which is nonunique because a given (honored) head gradient yields a specific discharge that is proportional to calibrated hydraulic conductivities. When transport simulations were run on the particle tracks from well RD-21, they were observed to travel unrealistically quickly. Upon careful examination of the hydraulic conductivities along the flow paths, the Upper Sage Unit near the Lower Burro Flats for only model layer 17 had an anomalously high hydraulic conductivity. This aberration does not reveal itself in the objective function

because simulated water levels, gradients, and seeps were all appropriate, but the specific discharge through just this unit is high. The high hydraulic conductivity of this layer of this unit attracts flow paths from well RD-21, which is upgradient. It is not physically plausible for this large unit (11,071 elements with a volume of 39.6 Mm^3) to have a hydraulic conductivity on the order of 1 m/day at the bottom of the model near zero elevation (below more than 500 m of overburden). Notably, the same unit in model layers 16 (just above) and 18 (just below) had hydraulic conductivities on the order of 10^{-4} and 0.01 m/day, respectively, much more realistic values.

This high calibrated hydraulic conductivity will be reexamined in a subsequent model calibration where regularization is used to constrain the hydraulic conductivity of each unit according to expert judgment unless the calibration data set suggests otherwise.

4.7.3 NSMC Contaminant Paths

Results can also be presented as particle tracks colored by contaminant concentrations cut off at $1/10^{th}$ of the MCL. Figure 87 shows TCE concentrations from well DD-144 along the 100 NSMC flow-path realizations after (top) 20, (middle) 50, and (bottom) 100 years without first-order degradation. Figure 88and Figure 89 show PCE and TCE concentrations, respectively, from well PZ-109 along the 100 NSMC flow-path realizations after (left) 20, (center) 50, and (right) 100 years without first-order degradation. Figure 90 shows TCE concentrations from well RD-07 along the 100 NSMC flow-path realizations after 20 (top), 50 (center), and 100 (bottom) years without first-order degradation. Figure 91 shows TCE concentrations from well RD-21 along the 100 NSMC flow-path realizations after 20 (top), 50 (center), and 100 (bottom) years without first-order degradation. Figure 92 shows TCE concentrations from well RD-23 along the 100 NSMC flow-path realizations after 20 (top), 50 (center), and 100 (bottom) years without first-order degradation. Figure 93 shows ^{3}H activities from well RD-90 along the 100 NSMC flow-path realizations after (left) 20 and (right) 50 years. Note that the activity drops below $1/10^{th}$ the MCL after 100 years (2,000 pCi/L). Figure 94 shows TCE concentrations from well RD-91 along the 100 NSMC flow-path realizations after 20 (top), 50 (center), and 100 (bottom) years without first-order degradation. Figure 95 shows ^{3}H activities from well RD-90 along the 100 NSMC flow-path realizations after (left) 20 and (right) 50 years. Note that the activity drops below $1/10^{th}$ the MCL after 100 years (2,000 pCi/L). Figure 96 shows ^{90}Sr activities from well RD-98 along the 100 NSMC flow-path realizations after (left) 20, (center) 50, and (right) 100 years. Figure 97 shows TCE concentrations from well RD-98 along the 100 NSMC flow-path realizations after (left) 20, (center) 50, and (right) 100 years without first-order degradation. Variation among the 100 NSMC realizations is significantly greater for transport from RD-21 and RD-91 than for transport from DD-144. This is because of the anomalously high calibrated hydraulic conductivity that draws particles released from RD-21 and RD-91 into it.

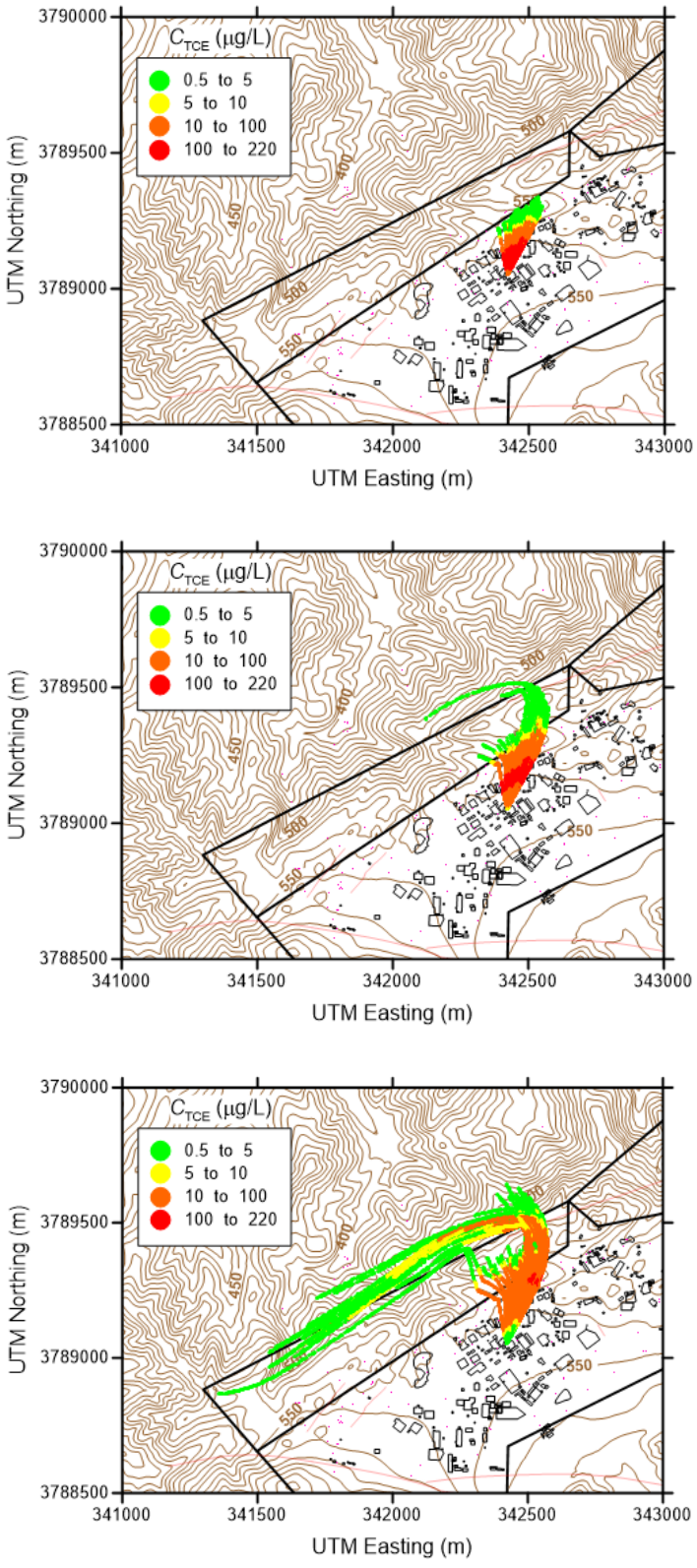

Figure 87: TCE concentrations along the 100 NSMC flow paths from well DD-144 after (top) 20, (center) 50, and (bottom) 100 years.

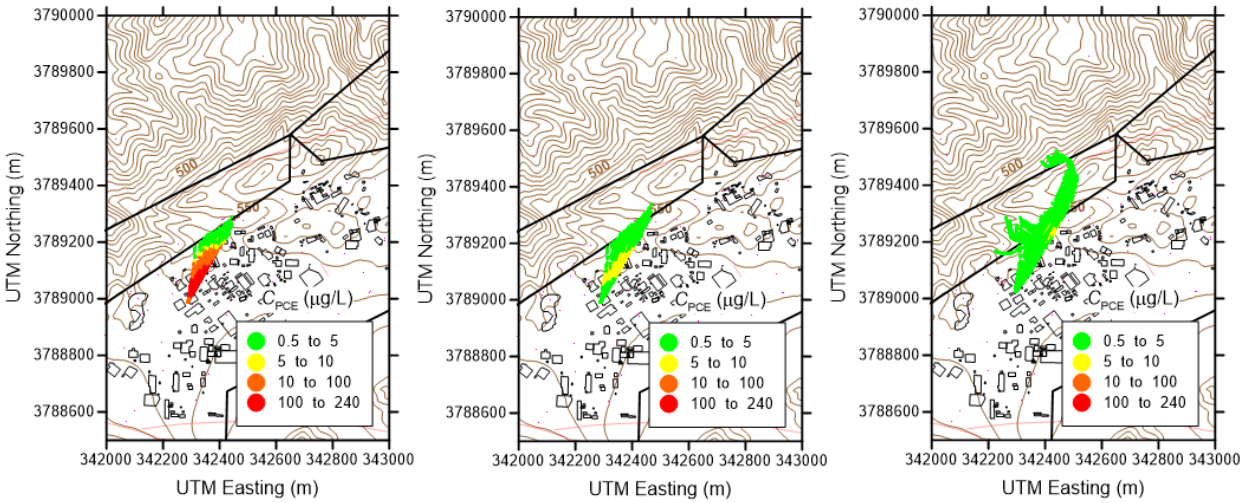

Figure 88: PCE concentrations along the 100 NSMC flow paths from well PZ-109 after (left) 20, (middle) 50, and (right) 100 years.

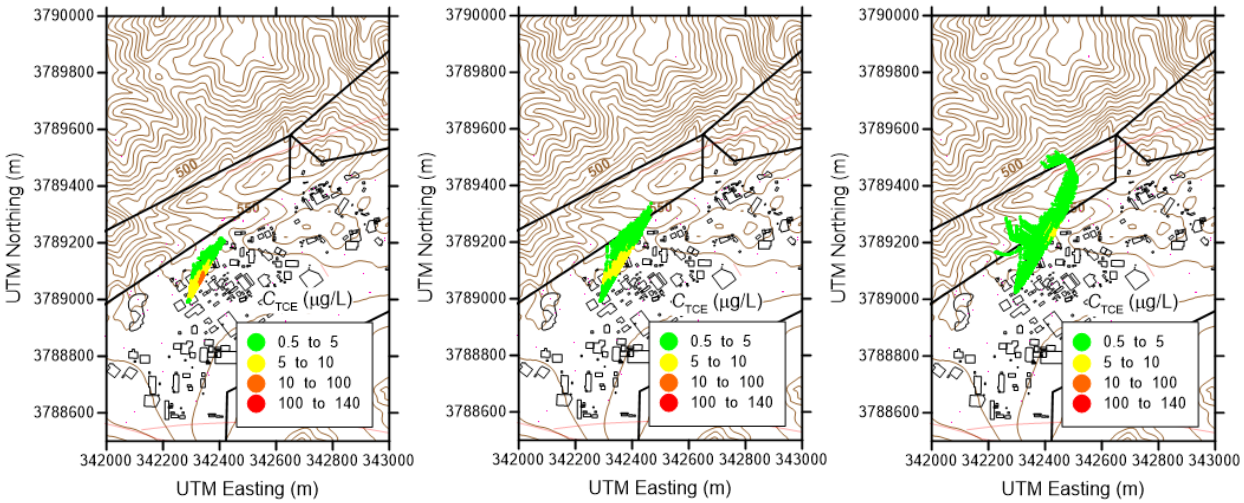

Figure 89: TCE concentrations along the 100 NSMC flow paths from well PZ-109 after (left) 20, (middle) 50, and (right) 100 years.

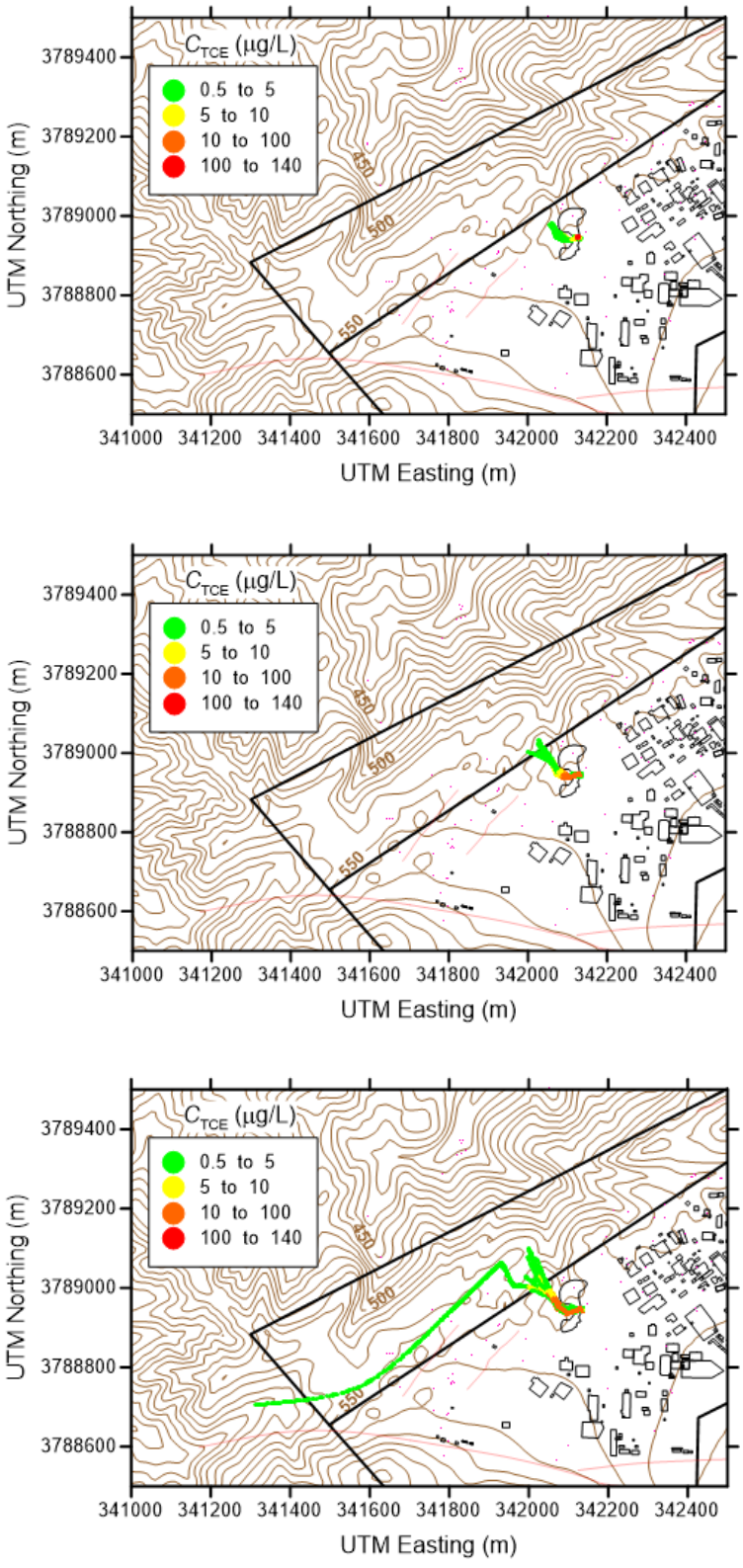

Figure 90: TCE concentrations along the 100 NSMC flow paths from well RD-07 after (top) 20, (center) 50, and (bottom) 100 years.

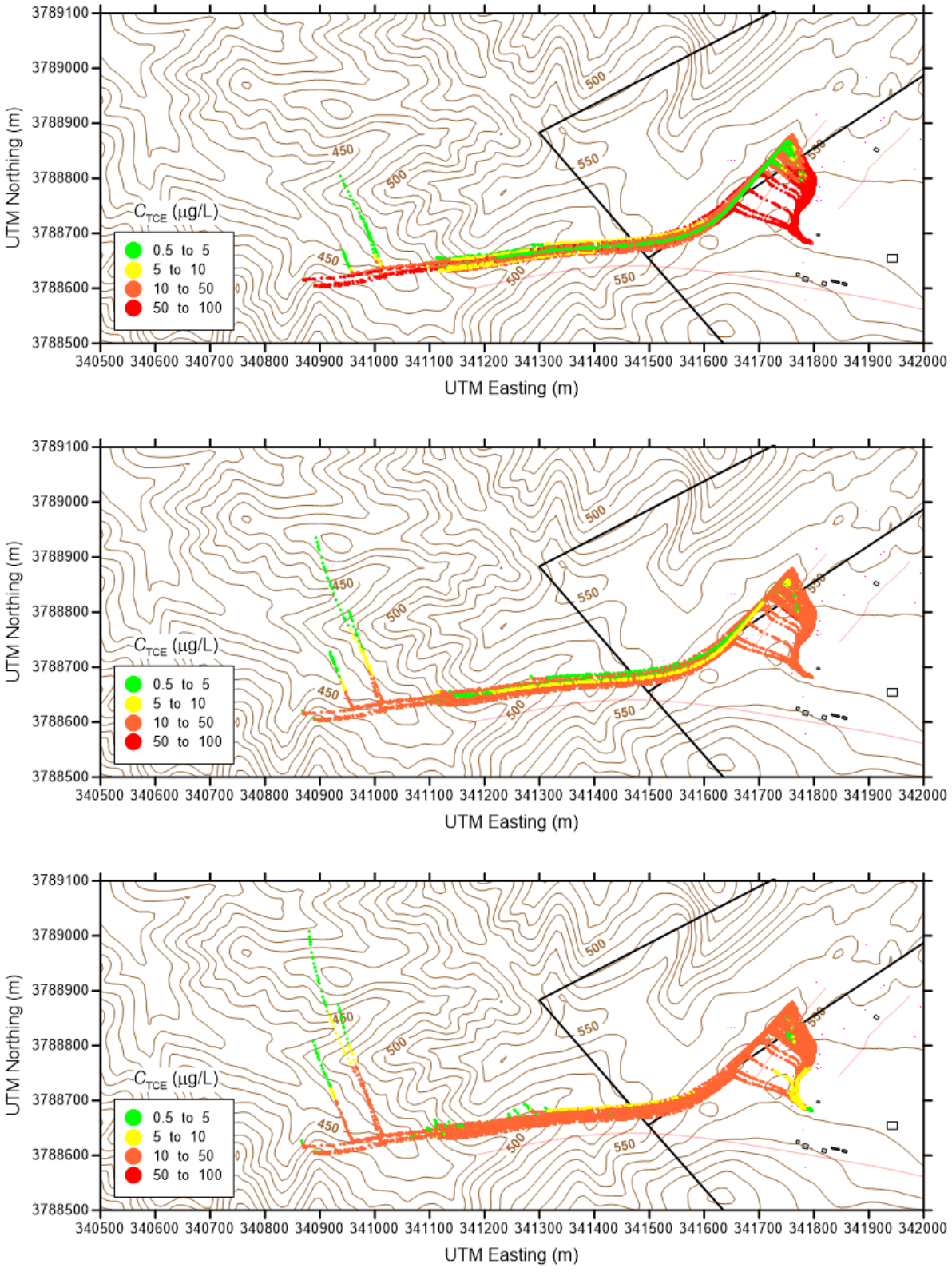

Figure 91: TCE concentrations along the 100 NSMC flow paths from well RD-21 after (top) 20, (center) 50, and (bottom) 100 years.

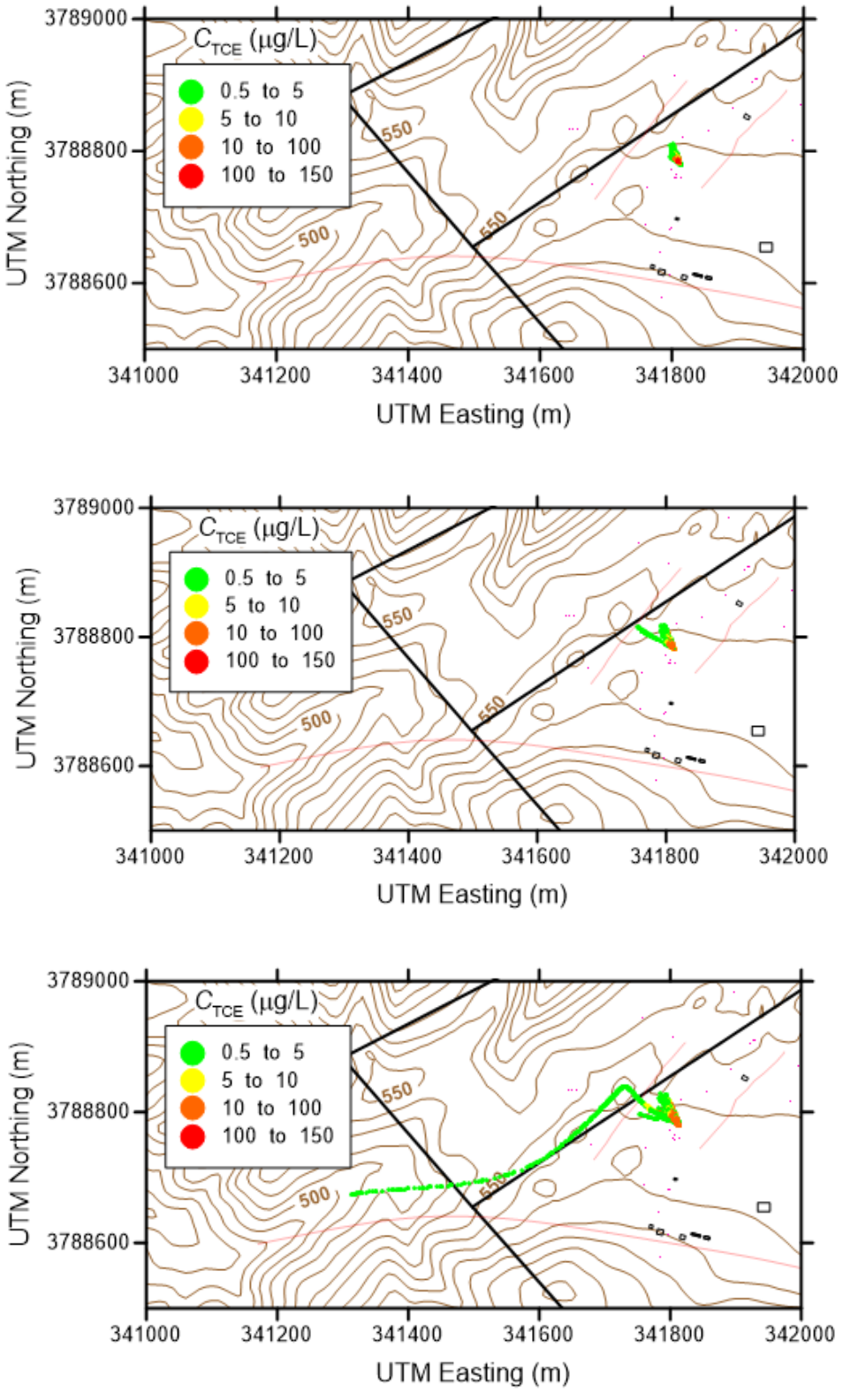

Figure 92: TCE concentrations along the 100 NSMC flow paths from well RD-23 after (top) 20, (center) 50, and (bottom) 100 years.

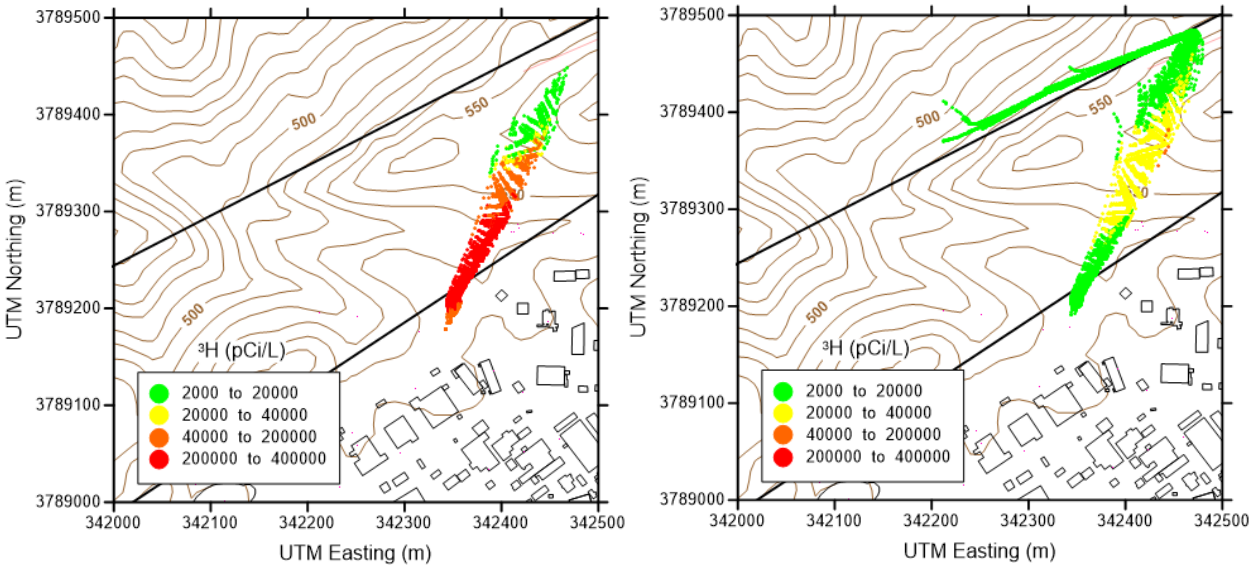

Figure 93: ^{3}H concentrations along the 100 NSMC flow paths from well RD-90 after (left) 20 and (right) 50 years. Note that after 100 years, all activity was below 1/10th the MCL (2,000 pCi/L).

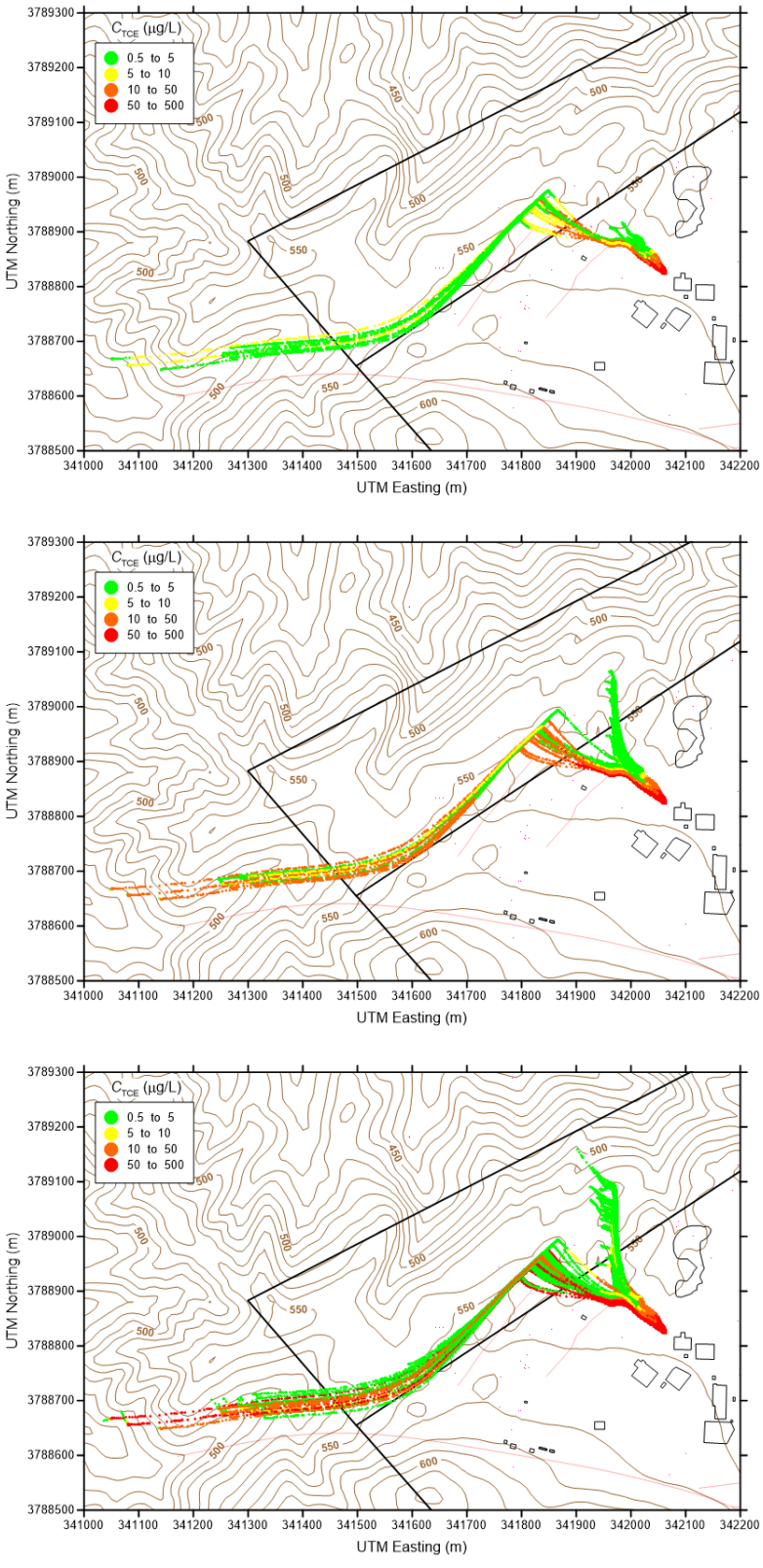

Figure 94: TCE concentrations along the 100 NSMC flow paths from well RD-91 after (top) 20, (center) 50, and (bottom) 100 years.

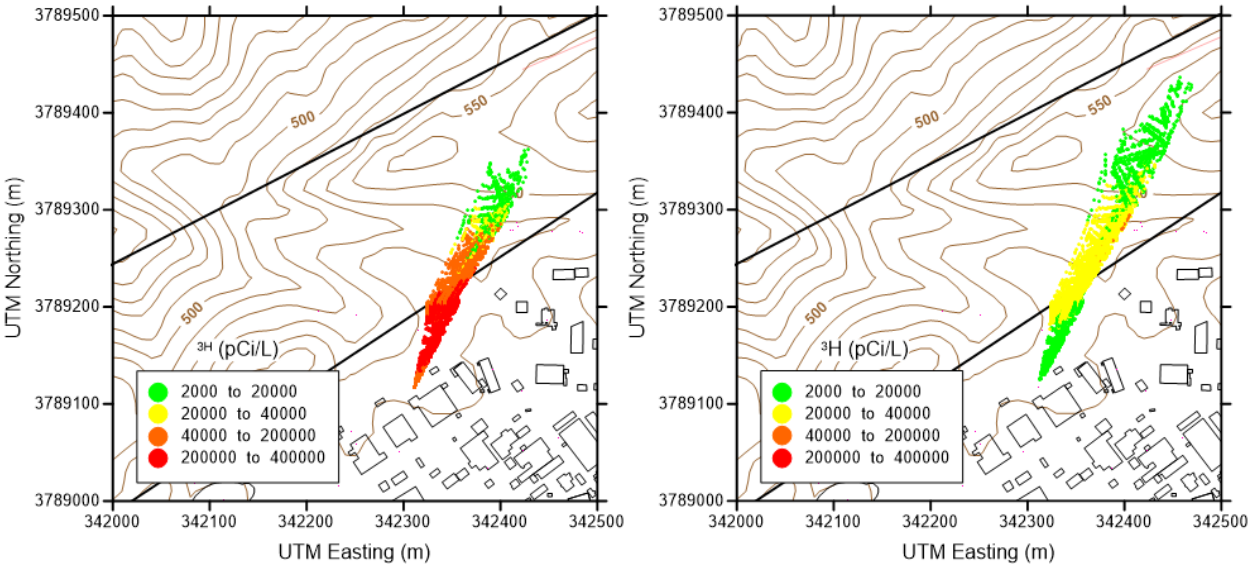

Figure 95: ^{3}H concentrations along the 100 NSMC flow paths from well RD-95 after (top) 20 and (right) 50 years. Note that after 100 years, all activity was below 1/10th the MCL (2,000 pCi/L).

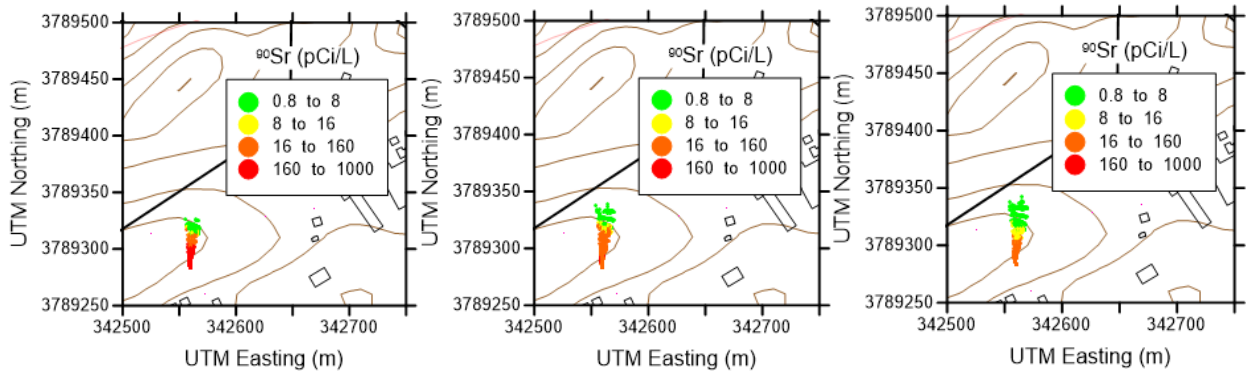

Figure 96: ^{90}Sr concentrations along the 100 NSMC flow paths from well RD-98 after (left) 20, (middle) 50, and (right) 100 years.

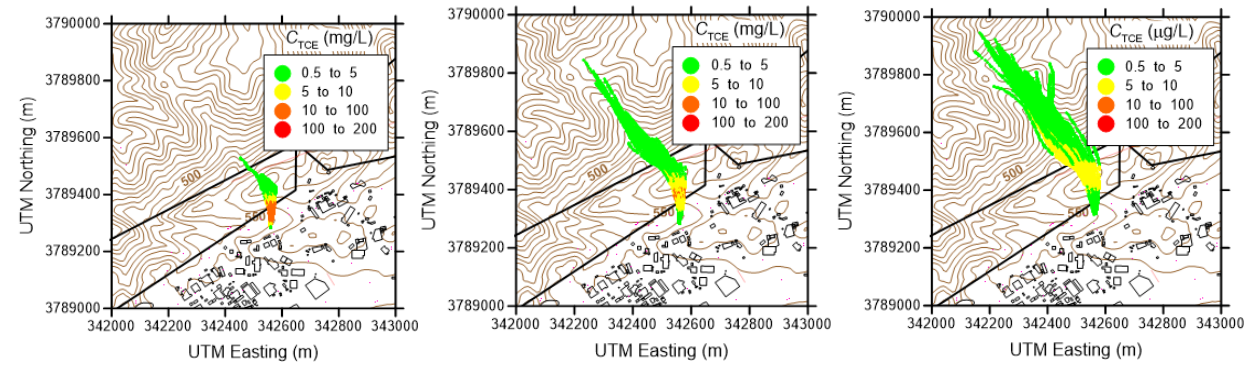

Figure 97: TCE concentrations along the 100 NSMC flow paths from well RD-98 after (top) 20, (center) 50, and (bottom) 100 years.

5. Conclusions

6. References

AquaResource Inc., and MWH Americas Inc., 2007, Three-dimensional Groundwater Flow Model Report, Ventura, CA, p. 429.

Cherry, J. A., D. McWhorter, and B. Parker, 2007, Overview of the Site Conceptual Model for the Migration and Fate of Contaminants in Groundwater at the Santa Susana Field Laboratory, Ventura, CA.

Christensen, S., and J. E. Doherty, 2008, Predictive error dependencies when using pilot points and singular value decomposition in groundwater model calibration: Advances in Water Resources, v. 31, p. 674-700.

DHI-WASY, 2012, FEFLOW 6.1. Finite Element Subsurface Flow & Transport Simulation System. User's Manual, Berlin, Germany, p. 116.

Doherty, J., 2015, Calibration and Uncertainty Analysis for Complex Environmental Models: Brisbane, Australia, Watermark Numerical Computing.

Doherty, J. E., 2016a, Model-independent Parameter Estimation User Manual Part I: PEST, SENSAN and Global Optimisers, *in* J. E. Doherty, ed., Brisbane, Australia, Watermark Numerical Computing, p. 390.

Doherty, J. E., 2016b, Model-independent Parameter Estimation User Manual Part II: PEST Utility Support Software, *in* J. E. Doherty, ed., Brisbane, Australia, Watermark Numerical Computing, p. 226.

Doherty, J. E., and R. J. Hunt, 2009, Two easily-calculated statistics for evaluating parameter identifiability and error reduction: Journal of Hydrology, v. 366, p. 119-127.

Doherty, J. E., S. C. James, and P. W. Reimus, 2011, Model-based decision making: A new perspective, 13th International High-Level Radioactive Waste Management Conference, Albuquerque, NM, American Nuclear Society, p. 1-10.

Gallagher, M., and J. E. Doherty, 2006, Predictive error analysis for a water resource management model: Journal of Hydrology, v. 34, p. 513-533.

James, S. C., B. W. Arnold, C. McMahon, J. Brownlow, J. Wondolleck, and S. Fundingsland, 2017, Santa Susana Field Laboratory Area IV: Flow and Transport Numerical Modeling, Waco, TX, Baylor University, p. 80.

James, S. C., J. E. Doherty, and A.-A. Eddebbarh, 2009, Practical postcalibration uncertainty analysis: Yucca Mountain, Nevada: Ground Water, v. 47, p. 851-869.

Malinowski, M. E., 2011, Letter from Mark Malinowski (DTSC) to Tom Gallacher (Boeing). Department of Toxic Substances Control Comments on the Sitewide Groundwater Remedial Investigation Report for Santa Susana Field Laboratory, Ventura County, California, Cypress, CA, Department of Toxic Substances Control.

Montgomery Watson, 2000, Technical Memorandum, Conceptual Site Model, Movement of TCE in the Chatsworth Formation, Santa Susana Field Laboratory, Walnut Creek, CA, p. 44.

Moore, C., and J. E. Doherty, 2006, The cost of uniqueness in groundwater model calibration: Advances in Water Resources, v. 29, p. 605-623.

Moore, C., T. Wöhling, and J. Doherty, 2010, Efficient regularization and uncertainty analysis using a global optimization methodology: Water Resour. Res., v. 46, p. W08527.

MWH, 2009, Draft Site-Wide Groundwater Remedial Investigation Report, Santa Susana Field Laboratory, Ventura County, California, Walnut Creek, CA, Montgomery-Watson-Harza.

MWH, 2013, Results of Geologic Mapping and Excavations Along the Western and Eastern FSDF Structures (Photolineaments) Area IV, *in* G. Hazelton, ed., Arcadia, CA, Montgomery-Watson-Harza Americas Inc., p. 53.

MWH Inc., 2009, Draft Site-wide Groundwater Remedial Investigation Report, Walnut Creek, CA, p. 648.
Schaap, M. G., and M. T. van Genuchten, 2006, A modified Mualem–van Genuchten formulation for improved description of the hydraulic conductivity near saturation: Vadose Zone Journal, v. 5, p. 27-34.
The Boeing Company, 2009, Draft Sitewide Groundwater Characterization Report, Santa Susana Field Laboratory, Ventura County, California, Canoga Park, CA.
The Boeing Company, 2015, Work Plan Finalization - SSFL Mountain Scale Groundwater Flow Model Update Proposed Numerical Flow Modelling Work Plan in Response to DTSC Comments on Draft SSFL Site-Wide Groundwater RI Report, The Boeing Conmpany, p. 73.
Thum, P., H. J. Diersch, and R. Gründler, 2011, SAMG - The linear solver for groundwater simulation, International Conference on Calibration and Reliability in Groundwater Modeling Leipzig, Germany, p. 183.
Tonkin, M. J., and J. E. Doherty, 2005, A hybrid regularized inversion methodology for highly parameterized environmental models: Water Resources Research, v. 41, p. W10412.
Tonkin, M. J., and J. E. Doherty, 2009, Calibration-constrained Monte Carlo analysis of highly-parameterized models using subspace techniques: Water Resources Research, v. 45, p. W00B10.
Tonkin, M. J., J. E. Doherty, and C. Moore, 2007, Efficient nonlinear predictive error variance for highly parameterized models: Water Resources Research, v. 43, p. W07429.
U.S. EPA, 1999, Understanding Variation in Partition Coefficient, Kd, Values, Volume II: Review of Geochemistry and Kd Values for Cadmium, Cesium, Chromium, Lead, Plutonium, Radon, Strontium, Thorium, Tritium (^{3}H), and Uranium, Washington, DC, US Environmental Protection Agency, p. 341.
van Genuchten, M. T., 1980, A closed-form equation for predicting the hydraulic conductivity of unsaturated soils1: Soil Science Society of America Journal, v. 44, p. 892-898.
White, J. T., M. N. Fienen, and J. E. Doherty, 2016, A python framework for environmental model uncertainty analysis: Environmental Modelling & Software, v. 85, p. 217-228.
Zyvoloski, G. A., 2007, FEHM: A Control Volume Finite Element Code for Simulating Subsurface Multi-Phase Multi-Fluid Heat and Mass Transfer, Los Alamos, NM, Los Alamos National Laboratory.

Appendix A

Table 8: Geologic unit, corresponding *K*-zone number, calibrated hydraulic conductivity, and horizontal-to-vertical anisotropy ratio.

Geologic Unit	***K* zone**	***K* (m/s)**	$K_{x,y}/K_z$ **(−)**
Alluvium	501	1.24×10^{-6}	46.58
Llajas	601	5.97×10^{-9}	113.79
Llajas	611	4.02×10^{-8}	113.79
Santa Susana	701	2.05×10^{-9}	7.50
Santa Susana	711	1.22×10^{-7}	7.50
Simi	801	7.97×10^{-9}	1
Santa Susana	809	2.41×10^{-7}	7.50
Simi	811	7.07×10^{-10}	1
Shale 3	901	4.72×10^{-9}	25.64
Santa Susana	909	7.89×10^{-8}	7.50
Upper Burro Flats	911	6.23×10^{-9}	1000
Shale3 SS	1001	8.05×10^{-10}	36.37
Santa Susana	1009	9.92×10^{-8}	7.50
Upper Burro Flats	1011	1.57×10^{-7}	1000
Shale 3	1101	2.03×10^{-9}	25.64
Santa Susana	1109	4.80×10^{-8}	7.50
Upper Burro Flats	1111	1.59×10^{-7}	1000
Upper Burro Flats	1201	5.15×10^{-11}	1000
Santa Susana	1209	3.69×10^{-7}	7.50
Upper Burro Flats	1210	1.21×10^{-6}	1000
Upper Burro Flats	1211	3.49×10^{-8}	1000
North Fault Zone	1212	1.09×10^{-8}	1000
Upper Burro Low K	1213	2.99×10^{-10}	18.17
Upper Burro Low K	1215	8.74×10^{-9}	18.17
Upper Burro Low K	1216	3.10×10^{-10}	18.17
Upper Burro Flats	1301	1.22×10^{-6}	1000
Santa Susana	1309	1.17×10^{-7}	7.50
Lot Bed	1310	5.05×10^{-10}	55.34
Upper Burro Flats	1311	3.27×10^{-7}	1000
North Fault Zone	1312	5.20×10^{-8}	1000
Upper Burro Low K	1313	2.37×10^{-9}	18.17
Upper Burro Low K	1315	3.59×10^{-9}	18.17
Upper Burro Low K	1316	7.24×10^{-10}	18.17
Upper Burro Flats	1401	2.42×10^{-10}	1000
Upper Burro Flats	1403	5.46×10^{-7}	1000
Santa Susana	1409	1.19×10^{-7}	7.50

Upper Burro Flats	1410	1.00×10^{-4}	1000
Upper Burro Flats	1411	1.20×10^{-8}	1000
North Fault Zone	1412	5.07×10^{-9}	1000
Upper Burro Low K	1413	3.16×10^{-10}	18.17
Upper Burro Low K	1415	1.05×10^{-8}	18.17
Upper Burro Low K	1416	1.85×10^{-9}	18.17
Upper Burro Low K	1417	8.49×10^{-9}	18.17
Upper Burro Low K	1418	3.94×10^{-9}	18.17
Upper Burro Low K	1419	2.01×10^{-9}	18.17
Upper Burro Flats	1501	1.36×10^{-10}	1000
ELV	1503	4.50×10^{-9}	370.01
Santa Susana	1509	1.37×10^{-6}	7.50
ELV	1510	2.71×10^{-9}	370.01
Upper Burro Flats	1511	1.17×10^{-8}	1000
North Fault Zone	1512	1.30×10^{-7}	1000
ELV	1513	6.92×10^{-10}	156.78
ELV	1515	9.29×10^{-10}	156.78
ELV	1516	7.34×10^{-9}	156.78
ELV	1517	9.70×10^{-10}	156.78
ELV	1518	9.90×10^{-10}	156.78
ELV	1519	8.87×10^{-10}	156.78
Lower Burro Flats	1601	1.27×10^{-9}	7.61
Lower Burro Flats	1603	1.18×10^{-5}	7.61
Lower Burro Flats	1607	2.88×10^{-7}	20.06
Santa Susana	1609	1.00×10^{-4}	7.50
Lower Burro Flats	1610	1.01×10^{-7}	7.61
Lower Burro Flats	1611	1.07×10^{-8}	7.61
North Fault Zone	1612	6.96×10^{-8}	1000
Lower Burro Flats	1613	5.28×10^{-8}	401.06
Lower Burro Flats	1615	2.17×10^{-7}	401.06
Lower Burro Flats	1616	3.20×10^{-9}	401.06
Lower Burro Flats	1617	1.21×10^{-6}	401.06
Lower Burro Flats	1618	4.05×10^{-8}	401.06
Lower Burro Flats	1619	1.02×10^{-7}	401.06
Lower Burro Flats	1701	3.69×10^{-5}	7.61
Lower Burro Flats	1703	3.50×10^{-6}	7.61
Lower Burro Flats	1707	6.96×10^{-7}	20.06
Santa Susana	1709	2.89×10^{-5}	7.50
Lower Burro Flats	1710	1.04×10^{-9}	7.61
Lower Burro Flats	1711	9.02×10^{-8}	7.61
North Fault Zone	1712	1.69×10^{-7}	1000

Lower Burro Flats	1713	1.95×10^{-8}	401.06
Lower Burro Flats	1715	1.46×10^{-7}	401.06
Lower Burro Flats	1716	5.57×10^{-9}	401.06
Lower Burro Flats	1717	5.55×10^{-9}	401.06
Lower Burro Flats	1718	7.03×10^{-8}	401.06
Lower Burro Flats	1719	1.72×10^{-7}	401.06
Lower Burro Flats	1801	1.41×10^{-6}	7.61
Silvernale	1802	2.60×10^{-9}	125.38
Lower Burro Flats	1803	1.00×10^{-4}	7.61
Lower Burro Flats	1807	9.88×10^{-7}	20.06
Santa Susana	1809	8.38×10^{-9}	7.50
Lower Burro Flats	1810	1.78×10^{-9}	7.61
Lower Burro Flats	1811	1.87×10^{-7}	7.61
North Fault Zone	1812	1.00×10^{-4}	1000
Lower Burro Flats	1813	9.69×10^{-7}	401.06
Lower Burro Flats	1815	1.79×10^{-8}	401.06
Lower Burro Flats	1816	1.00×10^{-4}	401.06
Lower Burro Flats	1817	1.04×10^{-8}	401.06
Lower Burro Flats	1818	6.41×10^{-8}	401.06
Lower Burro Flats	1819	4.72×10^{-7}	401.06
Shale 2	1901	3.57×10^{-9}	1
Shale 2	1902	2.51×10^{-9}	98
Spa	1903	6.91×10^{-10}	351.89
Lower Burro Flats	1907	5.60×10^{-7}	20.06
Santa Susana	1909	3.82×10^{-7}	7.50
Spa	1910	6.19×10^{-9}	351.89
Shale 2	1911	6.61×10^{-8}	1
North Fault Zone	1912	3.50×10^{-6}	1000
Spa	1913	8.52×10^{-10}	30.82
Spa	1915	9.79×10^{-10}	30.82
Spa	1916	1.41×10^{-9}	30.82
Spa	1917	9.51×10^{-10}	30.82
Spa	1918	2.51×10^{-10}	30.82
Spa	1919	1.01×10^{-9}	30.82
Upper Sage	2001	1.57×10^{-7}	1000
Shale 2	2002	4.09×10^{-9}	98
Silvernale	2003	3.08×10^{-8}	29.61
Silvernale	2007	6.78×10^{-7}	76.96
Santa Susana	2009	3.99×10^{-7}	7.50
Silvernale	2010	2.41×10^{-7}	29.61
Upper Sage	2011	1.65×10^{-6}	1000

North Fault Zone	2012	3.89×10^{-8}	1000
Silvernale	2013	9.78×10^{-7}	1.42
Silvernale	2015	1.07×10^{-8}	1.42
Silvernale	2016	1.00×10^{-4}	1.42
Silvernale	2017	5.87×10^{-7}	1.42
Silvernale	2018	3.71×10^{-8}	1.42
Silvernale	2019	5.99×10^{-7}	1.42
Shale 2	2101	3.44×10^{-9}	1
Shale 2	2102	3.09×10^{-9}	98
Shale 2	2103	3.24×10^{-9}	1
Upper Sage	2107	3.88×10^{-7}	1000
Santa Susana	2109	8.50×10^{-8}	7.50
Shale 2	2110	5.07×10^{-9}	1
Shale 2	2111	6.14×10^{-7}	1
North Fault Zone	2112	6.98×10^{-8}	1000
Shale 2	2113	9.33×10^{-10}	68.96
Shale 2	2115	9.20×10^{-10}	68.96
Shale 2	2116	7.05×10^{-10}	68.96
Shale 2	2117	1.15×10^{-9}	68.96
Shale 2	2118	9.16×10^{-10}	68.96
Shale 2	2119	9.16×10^{-10}	68.96
Upper Sage	2201	7.46×10^{-7}	1000
Upper Sage	2202	8.05×10^{-8}	8.73
Upper Sage	2203	9.19×10^{-9}	1000
Upper Sage	2207	8.96×10^{-9}	1000
Santa Susana	2209	1.07×10^{-8}	7.50
Upper Sage	2210	4.26×10^{-8}	1000
Upper Sage	2211	1.00×10^{-4}	1000
North Fault Zone	2212	7.25×10^{-7}	1000
Upper Sage	2213	4.88×10^{-5}	72.32
Upper Sage	2215	2.23×10^{-8}	72.32
Upper Sage	2216	4.02×10^{-9}	72.32
Upper Sage	2217	5.79×10^{-8}	72.32
Upper Sage	2218	1.21×10^{-8}	72.32
Upper Sage	2219	5.89×10^{-5}	72.32
Upper Sage	2301	5.27×10^{-7}	1000
Upper Sage	2302	6.20×10^{-10}	8.73
Shale 2	2303	3.30×10^{-9}	1
Upper Sage	2307	2.97×10^{-6}	1000
Santa Susana	2309	6.62×10^{-8}	7.50
Shale 2	2310	2.66×10^{-12}	1

Upper Sage	2311	1.02×10^{-5}	1000
North Fault Zone	2312	8.10×10^{-8}	1000
Shale 2	2313	9.03×10^{-10}	68.96
Shale 2	2315	9.66×10^{-10}	68.96
Shale 2	2316	8.82×10^{-10}	68.96
Shale 2	2317	9.97×10^{-10}	68.96
Shale 2	2318	7.23×10^{-10}	68.96
Shale 2	2319	9.70×10^{-10}	68.96
Middle Sage	2401	9.78×10^{-7}	1
Upper Sage	2402	4.62×10^{-9}	8.73
Middle Sage	2403	2.08×10^{-5}	1
Upper Sage	2407	1.17×10^{-7}	1000
Santa Susana	2409	2.62×10^{-9}	7.50
Upper Sage	2410	7.93×10^{-8}	1000
Middle Sage	2411	5.36×10^{-5}	1
North Fault Zone	2412	2.39×10^{-7}	1000
Upper Sage	2413	4.44×10^{-5}	72.32
Upper Sage	2415	1.18×10^{-8}	72.32
Upper Sage	2416	1.40×10^{-9}	72.32
Upper Sage	2417	5.59×10^{-8}	72.32
Upper Sage	2418	2.70×10^{-8}	72.32
Upper Sage	2419	2.20×10^{-8}	72.32
Lower Sage	2501	2.00×10^{-6}	2.43
Upper Line Bed	2502	5.11×10^{-10}	105.29
Middle Sage	2503	1.19×10^{-6}	1
Middle Sage	2507	1.25×10^{-6}	65.09
Santa Susana	2509	1.70×10^{-8}	7.50
Upper Bravo	2510	9.28×10^{-9}	89.22
Lower Sage	2511	1.67×10^{-6}	2.43
North Fault Zone	2512	4.54×10^{-7}	1000
Upper Bravo	2513	7.86×10^{-9}	52.93
Upper Bravo	2515	8.38×10^{-9}	52.93
Upper Bravo	2516	7.44×10^{-9}	52.93
Upper Bravo	2517	9.39×10^{-9}	52.93
Upper Bravo	2518	7.63×10^{-9}	52.93
Upper Bravo	2519	6.68×10^{-9}	52.93
Lower Sage	2601	1.04×10^{-6}	2.43
Middle Sage	2602	2.84×10^{-8}	24.26
Middle Sage	2603	2.08×10^{-6}	1
Canyon	2604	1.27×10^{-8}	1.83
Middle Sage	2607	2.22×10^{-5}	65.09

Simi	2608	2.36×10^{-7}	1
Santa Susana	2609	2.31×10^{-8}	7.50
Middle Sage	2610	8.73×10^{-7}	1
Lower Sage	2611	5.53×10^{-6}	2.43
North Fault Zone	2612	5.97×10^{-7}	1000
Middle Sage	2613	2.32×10^{-7}	58.54
Middle Sage	2615	6.88×10^{-8}	58.54
Middle Sage	2616	2.75×10^{-7}	58.54
Middle Sage	2617	1.13×10^{-7}	58.54
Middle Sage	2618	8.38×10^{-8}	58.54
Middle Sage	2619	1.32×10^{-7}	58.54
Lower Sage	2701	1.26×10^{-6}	2.43
Lower Line Bed	2702	2.87×10^{-10}	170.85
Middle Sage	2703	1.33×10^{-6}	1
Canyon	2704	3.25×10^{-7}	1.83
Middle Sage	2707	7.57×10^{-6}	65.09
Simi	2708	1.27×10^{-7}	1
Santa Susana	2709	2.61×10^{-8}	7.50
Lower Bravo	2710	3.90×10^{-9}	54.43
Lower Sage	2711	2.89×10^{-5}	2.43
North Fault Zone	2712	9.61×10^{-8}	1000
Lower Bravo	2713	7.21×10^{-9}	55.06
Lower Bravo	2715	7.09×10^{-9}	55.06
Lower Bravo	2716	6.19×10^{-9}	55.06
Lower Bravo	2717	1.00×10^{-9}	55.06
Lower Bravo	2718	7.29×10^{-9}	55.06
Lower Bravo	2719	7.27×10^{-9}	55.06
Woolsey	2801	4.51×10^{-9}	99.18
Lower Sage	2802	7.27×10^{-6}	163.48
Lower Sage	2803	3.91×10^{-5}	9.19
Canyon	2804	6.79×10^{-6}	1.83
Canyon	2805	4.80×10^{-10}	1.83
Lower Sage	2807	1.00×10^{-4}	107.89
Simi	2808	1.64×10^{-7}	1
Santa Susana	2809	8.04×10^{-8}	7.50
Lower Sage	2810	9.90×10^{-5}	2.43
Woolsey	2811	3.64×10^{-9}	99.18
North Fault Zone	2812	1.23×10^{-7}	1000
Lower Sage	2813	1.54×10^{-6}	9.19
Canyon B	2814	4.25×10^{-8}	1.83
Lower Sage	2815	2.66×10^{-6}	9.19

Lower Sage	2816	4.80×10^{-7}	9.19
Lower Sage	2817	4.10×10^{-6}	9.19
Lower Sage	2818	4.08×10^{-7}	9.19
Lower Sage	2819	4.88×10^{-7}	9.19
Woolsey	2902	2.22×10^{-10}	175.57
Lower Sage	2903	1.00×10^{-4}	9.19
Canyon	2904	1.10×10^{-5}	1.83
Happy Valley	2905	1.46×10^{-9}	506.96
Lower Sage	2907	1.33×10^{-8}	107.89
Simi	2908	1.79×10^{-7}	1
Santa Susana	2909	2.02×10^{-9}	7.50
Lower Sage	2910	1.29×10^{-6}	2.43
Canyon	2911	9.55×10^{-8}	67.03
North Fault Zone	2912	9.95×10^{-8}	1000
Canyon B	2914	7.37×10^{-8}	1.83
Lower Sage	2916	1.26×10^{-6}	9.19
Lower Sage	2917	4.95×10^{-7}	9.19
Canyon	3002	4.48×10^{-9}	1000
Lower Sage	3003	3.54×10^{-8}	9.19
Canyon	3004	3.19×10^{-10}	1.83
Bowl	3005	8.05×10^{-9}	68.57
Bowl	3007	4.34×10^{-6}	1.21
Bowl	3008	1.73×10^{-6}	1.21
Las Virgenes	3009	2.37×10^{-9}	1000
Lower Sage	3010	3.35×10^{-6}	2.43
Canyon	3011	1.71×10^{-7}	67.03
North Fault Zone	3012	1.02×10^{-7}	1000
Canyon B	3014	4.27×10^{-6}	1.83
Lower Sage	3017	7.51×10^{-7}	9.19
Canyon	3102	1.77×10^{-5}	1000
Woolsey	3103	5.02×10^{-9}	99.18
Happy Valley	3104	8.29×10^{-11}	506.96
Bowl	3105	8.76×10^{-8}	68.57
Bowl	3107	5.64×10^{-7}	1.21
Bowl	3108	4.65×10^{-6}	1.21
Simi	3109	2.00×10^{-8}	1
Woolsey	3110	5.72×10^{-9}	99.18
Canyon	3111	3.92×10^{-7}	67.03
North Fault Zone	3112	7.08×10^{-8}	1000
Happy Valley	3114	1.02×10^{-9}	506.96
Canyon	3202	2.25×10^{-7}	1000

Canyon	3203	3.18×10^{-7}	67.03
Bowl	3204	1.00×10^{-5}	68.57
Bowl	3205	5.55×10^{-10}	68.57
Canyon	3206	1.56×10^{-7}	48.61
Bowl	3207	5.37×10^{-7}	1.21
Lower Chatsworth SS	3208	2.46×10^{-7}	1000
Lower Chatsworth SS	3209	9.47×10^{-6}	1000
Canyon	3210	1.06×10^{-6}	67.03
Happy Valley	3211	2.62×10^{-9}	49.43
North Fault Zone	3212	9.99×10^{-8}	1000
Bowl	3214	7.74×10^{-10}	68.57
Happy Valley	3302	7.51×10^{-10}	1000
Canyon	3303	4.61×10^{-7}	67.03
Bowl Bed	3304	7.69×10^{-9}	13.71
Bowl Bed	3305	2.54×10^{-8}	13.71
Canyon	3306	4.60×10^{-8}	48.61
Lower Chatsworth SS	3307	5.02×10^{-7}	1000
Lower Chatsworth SS	3308	3.65×10^{-7}	1000
Lower Chatsworth SS	3309	1.22×10^{-6}	1000
Canyon	3310	1.28×10^{-7}	67.03
Bowl	3311	3.81×10^{-7}	81.90
North Fault Zone	3312	1.12×10^{-7}	1000
Bowl Bed	3314	3.60×10^{-10}	13.71
Happy Valley	3402	1.42×10^{-9}	1000
Canyon	3403	4.69×10^{-8}	67.03
Bowl	3404	2.54×10^{-8}	68.57
Bowl	3405	1.26×10^{-7}	68.57
Happy Valley	3406	2.53×10^{-9}	56.47
Lower Chatsworth SS	3407	1.48×10^{-6}	1000
Lower Chatsworth SS	3408	1.07×10^{-7}	1000
Lower Chatsworth SS	3409	4.41×10^{-8}	1000
Canyon	3410	1.01×10^{-7}	67.03
Bowl	3411	6.75×10^{-8}	81.90
North Fault Zone	3412	9.24×10^{-8}	1000
Bowl	3414	2.49×10^{-7}	68.57
Happy Valley	3502	1.53×10^{-9}	1000
Canyon	3503	1.49×10^{-7}	67.03
Bowl Bed	3504	2.18×10^{-9}	13.71
Bowl Bed	3505	1.92×10^{-8}	13.71
Happy Valley	3506	2.67×10^{-9}	56.47
Lower Chatsworth SS	3507	5.94×10^{-7}	1000

Lower Chatsworth SS	3508	1.01×10^{-7}	1000
Lower Chatsworth SS	3509	7.69×10^{-7}	1000
Canyon	3510	7.19×10^{-7}	67.03
Bowl	3511	3.83×10^{-8}	81.90
North Fault Zone	3512	1.13×10^{-7}	1000
Bowl Bed	3514	5.21×10^{-8}	13.71
Happy Valley	3602	1.58×10^{-9}	1000
Canyon	3603	1.56×10^{-7}	67.03
Bowl	3604	9.79×10^{-9}	68.57
Bowl	3605	2.25×10^{-8}	68.57
Happy Valley	3606	2.46×10^{-9}	56.47
Lower Chatsworth SS	3607	6.05×10^{-8}	1000
Lower Chatsworth Shale	3608	5.93×10^{-9}	121.51
Lower Chatsworth SS	3609	3.17×10^{-7}	1000
Canyon	3610	8.70×10^{-7}	67.03
Bowl	3611	2.25×10^{-7}	81.90
North Fault Zone	3612	1.10×10^{-7}	1000
Bowl	3614	8.03×10^{-9}	68.57
Bowl	3702	9.87×10^{-7}	45.17
Happy Valley	3703	2.42×10^{-9}	49.43
Bowl	3704	5.80×10^{-8}	68.57
Lower Chatsworth SS	3705	3.28×10^{-8}	1000
Happy Valley	3706	2.74×10^{-9}	56.47
Lower Chatsworth Shale	3707	7.43×10^{-9}	121.51
Lower Chatsworth SS	3708	2.08×10^{-7}	1000
Lower Chatsworth Conglomerate	3709	2.10×10^{-8}	1000
Bowl	3710	5.45×10^{-7}	81.90
Bowl	3711	7.68×10^{-7}	81.90
Bowl	3714	5.61×10^{-9}	68.57
Bowl	3802	6.90×10^{-7}	45.17
Bowl	3803	7.10×10^{-8}	81.90
Lower Chatsworth SS	3804	4.84×10^{-7}	1000
Lower Chatsworth SS	3805	1.01×10^{-9}	1000
Bowl	3806	6.87×10^{-5}	1.21
Lower Chatsworth SS	3807	9.91×10^{-7}	1000
Lower Chatsworth SS	3808	1.78×10^{-8}	1000
Lower Chatsworth Shale	3809	1.32×10^{-9}	121.51
Bowl	3810	7.74×10^{-8}	81.90
Lower Chatsworth Shale	3811	4.26×10^{-9}	121.51
Lower Chatsworth SS	3814	2.89×10^{-9}	1000
Lower Chatsworth SS	3902	3.32×10^{-7}	1000

Bowl	3903	1.18×10^{-7}	81.90
Lower Chatsworth SS	3904	7.81×10^{-8}	1000
Lower Chatsworth SS	3905	1.51×10^{-6}	1000
Bowl	3906	3.64×10^{-7}	1.21
Lower Chatsworth Shale 2	3907	2.84×10^{-9}	121.51
Lower Chatsworth SS	3908	4.26×10^{-8}	1000
Lower Chatsworth Shale	3909	1.59×10^{-8}	121.51
Bowl	3910	1.96×10^{-7}	81.90
Lower Chatsworth SS	3911	7.72×10^{-8}	1000
Lower Chatsworth SS	3914	2.90×10^{-8}	1000
Lower Chatsworth SS	4002	7.33×10^{-8}	1000
Bowl	4003	1.21×10^{-7}	81.90
Lower Chatsworth SS	4004	1.60×10^{-7}	1000
Lower Chatsworth SS	4005	2.06×10^{-7}	1000
Bowl	4006	1.19×10^{-7}	1.21
Lower Chatsworth Shale 2	4007	2.72×10^{-9}	121.51
Lower Chatsworth SS	4008	6.00×10^{-8}	1000
Lower Chatsworth SS	4009	9.55×10^{-7}	1000
Bowl	4010	1.07×10^{-7}	81.90
Lower Chatsworth SS	4011	2.90×10^{-7}	1000
Lower Chatsworth SS	4014	1.22×10^{-7}	1000
Lower Chatsworth SS	4102	6.12×10^{-7}	1000
Bowl	4103	3.90×10^{-7}	81.90
Lower Chatsworth SS	4104	8.46×10^{-8}	1000
Lower Chatsworth SS	4105	1.26×10^{-7}	1000
Bowl	4106	4.43×10^{-8}	1.21
Lower Chatsworth SS	4107	1.09×10^{-6}	1000
Lower Chatsworth Shale	4108	8.04×10^{-9}	121.51
Lower Chatsworth Shale	4109	3.39×10^{-9}	121.51
Bowl	4110	6.85×10^{-7}	81.90
Bowl	4111	8.31×10^{-8}	81.90
Lower Chatsworth SS	4114	5.30×10^{-7}	1000
Lower Chatsworth SS	4202	2.75×10^{-7}	1000
Bowl	4203	4.81×10^{-8}	81.90
Lower Chatsworth SS	4204	2.45×10^{-7}	1000
Lower Chatsworth SS	4205	5.86×10^{-8}	1000
Bowl	4206	3.66×10^{-7}	1.21
Lower Chatsworth SS	4207	1.14×10^{-8}	1000
Lower Chatsworth SS	4208	3.36×10^{-7}	1000
Lower Chatsworth Shale	4209	2.98×10^{-9}	121.51
Bowl	4210	7.30×10^{-8}	81.90

Lower Chatsworth SS	4214	1.75×10^{-7}	1000
Lower Chatsworth SS	4302	7.83×10^{-8}	1000
Lower Chatsworth SS	4303	1.58×10^{-7}	1000
Lower Chatsworth SS	4304	5.85×10^{-8}	1000
Lower Chatsworth Shale 3	4305	2.34×10^{-10}	121.51
Lower Chatsworth SS	4306	1.34×10^{-7}	1000
Lower Chatsworth SS	4307	7.22×10^{-9}	1000
Lower Chatsworth Shale	4308	8.31×10^{-9}	121.51
Lower Chatsworth SS	4309	1.01×10^{-6}	1000
Lower Chatsworth SS	4310	1.33×10^{-7}	1000
Lower Chatsworth SS	4314	7.46×10^{-7}	1000
Lower Chatsworth SS	4402	4.18×10^{-7}	1000
Lower Chatsworth SS	4403	2.09×10^{-6}	1000
Lower Chatsworth SS	4404	7.98×10^{-9}	1000
Lower Chatsworth SS	4405	8.45×10^{-9}	1000
Lower Chatsworth SS	4406	8.44×10^{-8}	1000
Lower Chatsworth SS	4407	5.01×10^{-8}	1000
Lower Chatsworth SS	4408	5.26×10^{-8}	1000
Lower Chatsworth Shale	4409	4.06×10^{-9}	121.51
Lower Chatsworth SS	4410	3.10×10^{-7}	1000
Lower Chatsworth SS	4414	1.19×10^{-7}	1000
Lower Chatsworth SS	4502	1.92×10^{-7}	1000
Lower Chatsworth SS	4503	7.74×10^{-8}	1000
Lower Chatsworth SS	4504	2.48×10^{-6}	1000
Lower Chatsworth SS	4505	2.91×10^{-7}	1000
Lower Chatsworth SS	4506	3.45×10^{-7}	1000
Lower Chatsworth SS	4507	5.13×10^{-7}	1000
Lower Chatsworth SS	4508	6.12×10^{-7}	1000
Lower Chatsworth SS	4509	8.70×10^{-6}	1000
Lower Chatsworth SS	4510	5.21×10^{-7}	1000
Lower Chatsworth SS	4514	2.88×10^{-7}	1000
Lower Chatsworth SS	4602	1.35×10^{-7}	1000
Lower Chatsworth SS	4604	4.29×10^{-7}	1000
Lower Chatsworth Shale	4605	2.53×10^{-8}	121.51
Lower Chatsworth SS	4606	2.41×10^{-6}	1000
Lower Chatsworth Shale	4607	7.84×10^{-9}	121.51
Lower Chatsworth SS	4608	1.05×10^{-7}	1000
Lower Chatsworth Shale	4609	1.01×10^{-8}	121.51
Lower Chatsworth SS	4610	4.24×10^{-7}	1000
Lower Chatsworth SS	4702	3.76×10^{-7}	1000
Lower Chatsworth SS	4704	2.61×10^{-6}	1000

Lower Chatsworth SS	4705	9.29×10^{-7}	1000
Lower Chatsworth SS	4706	2.88×10^{-6}	1000
Lower Chatsworth SS	4707	2.61×10^{-7}	1000
Lower Chatsworth SS	4708	3.80×10^{-7}	1000
Lower Chatsworth SS	4709	8.42×10^{-8}	1000
Lower Chatsworth SS	4710	4.82×10^{-8}	1000
Lower Chatsworth SS	4802	1.53×10^{-7}	1000
Lower Chatsworth Shale	4804	4.76×10^{-9}	121.51
Lower Chatsworth Shale	4805	6.26×10^{-9}	121.51
Lower Chatsworth Shale	4806	5.54×10^{-8}	121.51
Lower Chatsworth SS	4807	1.31×10^{-7}	1000
Lower Chatsworth Shale	4808	1.72×10^{-8}	121.51
Lower Chatsworth SS	4809	1.97×10^{-7}	1000
Lower Chatsworth SS	4904	2.45×10^{-7}	1000
Lower Chatsworth SS	4905	2.95×10^{-7}	1000
Lower Chatsworth SS	4906	2.66×10^{-7}	1000
Lower Chatsworth SS	4907	1.04×10^{-7}	1000
Miocene	4908	5.65×10^{-7}	68.37
Lower Chatsworth Shale	4909	5.01×10^{-10}	121.51
Lower Chatsworth SS	5004	3.06×10^{-7}	1000
Lower Chatsworth SS	5005	1.24×10^{-7}	1000
Lower Chatsworth SS	5006	6.10×10^{-7}	1000
Lower Chatsworth SS	5007	6.77×10^{-7}	1000
Miocene	5008	7.43×10^{-8}	68.37
Miocene	5009	6.84×10^{-7}	68.37
Lower Chatsworth SS	5104	7.90×10^{-8}	1000
Lower Chatsworth SS	5105	1.22×10^{-7}	1000
Lower Chatsworth SS	5106	3.62×10^{-7}	1000
Lower Chatsworth SS	5107	4.01×10^{-7}	1000
Miocene	5108	5.35×10^{-7}	68.37
Miocene	5109	4.20×10^{-9}	68.37
Onsite Alluvium West	61000	1.42×10^{-5}	56.78
Onsite Alluvium East	62000	1.06×10^{-8}	56.78
Offsite Alluvium	99991	2.17×10^{-9}	50
Weathered rock	99998	9.00×10^{-8}	1

Table 9: Fault, *K*-zone number, calibrated hydraulic conductivity, and *K*-zone number to which it is tied (included to allow for fault damage zones to have unique hydraulic conductivities, but not implemented).

Fault Name	***K* zone**	***K* (m/s)**	**Tied to**
Santa Susana Pass Fault	70011	1.82×10^{-9}	
Santa Susana Pass Fault	70012	1.82×10^{-9}	70011
Shear Zone Fault	71011	8.24×10^{-12}	
Shear Zone Fault	71012	8.24×10^{-12}	71011
Shear Zone Fault	71013	8.24×10^{-12}	71011
Shear Zone Fault	71021	3.51×10^{-11}	
Shear Zone Fault	71022	3.51×10^{-11}	71021
Shear Zone Fault	71023	3.51×10^{-11}	71021
Shear Zone Fault	71031	3.52×10^{-11}	
Shear Zone Fault	71032	3.52×10^{-11}	71031
Shear Zone Fault	71033	3.52×10^{-11}	71031
Shear Zone Fault	71041	4.24×10^{-11}	
Shear Zone Fault	71042	4.24×10^{-11}	71041
Shear Zone Fault	71043	4.24×10^{-11}	71041
Shear Zone Fault	71051	2.86×10^{-11}	
Shear Zone Fault	71052	2.86×10^{-11}	71051
Shear Zone Fault	71053	2.86×10^{-11}	71051
Shear Zone Fault	71061	4.76×10^{-12}	
Shear Zone Fault	71062	4.76×10^{-12}	71061
Shear Zone Fault	71063	4.76×10^{-12}	71061
Shear Zone Fault	71081	2.56×10^{-12}	
Shear Zone Fault	71082	2.56×10^{-12}	71081
Shear Zone Fault	71083	2.56×10^{-12}	71081
Shear Zone Fault	71101	2.55×10^{-11}	
Shear Zone Fault	71102	2.55×10^{-11}	71101
Shear Zone Fault	71103	2.55×10^{-11}	71101
Box Canyon Fault	72011	1.67×10^{-9}	
Box Canyon Fault	72012	1.67×10^{-9}	72011
Box Canyon Fault	72013	1.67×10^{-9}	72011
Box Canyon Fault	72031	7.96×10^{-10}	
Box Canyon Fault	72032	7.96×10^{-10}	72031
Box Canyon Fault	72033	7.96×10^{-10}	72031
Box Canyon Fault	72041	1.63×10^{-9}	
Box Canyon Fault	72042	1.63×10^{-9}	72041
Box Canyon Fault	72043	1.63×10^{-9}	72041
Box Canyon Fault	72051	1.04×10^{-7}	
Box Canyon Fault	72052	1.04×10^{-7}	72051
Box Canyon Fault	72053	1.04×10^{-7}	72051

Box Canyon Fault	72061	1.07×10^{-9}	
Box Canyon Fault	72062	1.07×10^{-9}	72061
Box Canyon Fault	72063	1.07×10^{-9}	72061
Box Canyon Fault	72071	1.40×10^{-8}	
Box Canyon Fault	72072	1.40×10^{-8}	72071
Box Canyon Fault	72073	1.40×10^{-8}	72071
Box Canyon Fault	72081	4.56×10^{-10}	
Box Canyon Fault	72082	4.56×10^{-10}	72081
Box Canyon Fault	72083	4.56×10^{-10}	72081
Box Canyon Fault	72091	8.41×10^{-10}	
Box Canyon Fault	72092	8.41×10^{-10}	72091
Box Canyon Fault	72093	8.41×10^{-10}	72091
Box Canyon Fault	72101	7.98×10^{-10}	
Box Canyon Fault	72102	7.98×10^{-10}	72101
Box Canyon Fault	72103	7.98×10^{-10}	72101
Woolsey Fault	73011	9.34×10^{-11}	
Woolsey Fault	73012	9.34×10^{-11}	73011
Woolsey Fault	73013	9.34×10^{-11}	73011
Woolsey Fault	73021	2.73×10^{-8}	
Woolsey Fault	73022	2.73×10^{-8}	73021
Woolsey Fault	73023	2.73×10^{-8}	73021
Woolsey Fault	73031	3.20×10^{-10}	
Woolsey Fault	73032	3.20×10^{-10}	73031
Woolsey Fault	73033	3.20×10^{-10}	73031
Woolsey Fault	73041	1.25×10^{-9}	
Woolsey Fault	73042	1.25×10^{-9}	73041
Woolsey Fault	73043	1.25×10^{-9}	73041
Woolsey Fault	73051	3.61×10^{-12}	
Woolsey Fault	73052	3.61×10^{-12}	73051
Woolsey Fault	73053	3.61×10^{-12}	73051
IEL Fault	74011	4.24×10^{-12}	
IEL Fault	74012	4.24×10^{-12}	74011
IEL Fault	74013	4.24×10^{-12}	74011
Happy Valley Fault	75011	4.84×10^{-9}	
Happy Valley Fault	75012	4.84×10^{-9}	75011
Happy Valley Fault	75013	4.84×10^{-9}	75011
Happy Valley Fault	75021	1.57×10^{-10}	
Happy Valley Fault	75022	1.57×10^{-10}	75021
Happy Valley Fault	75023	1.57×10^{-10}	75021
Bowl Structure	75031	1.28×10^{-7}	
Bowl Structure	75032	1.28×10^{-7}	75031

Bowl Structure	75033	1.28×10^{-7}	75031
Happy Valley Fault	75041	3.31×10^{-8}	
Happy Valley Fault	75042	3.31×10^{-8}	75041
Happy Valley Fault	75043	3.31×10^{-8}	75041
Happy Valley Fault	75061	4.25×10^{-10}	
Happy Valley Fault	75062	4.25×10^{-10}	75061
Happy Valley Fault	75063	4.25×10^{-10}	75061
Happy Valley Fault	75071	1.01×10^{-7}	
Happy Valley Fault	75072	1.01×10^{-7}	75071
Happy Valley Fault	75073	1.01×10^{-7}	75071
Happy Valley Fault	75081	5.86×10^{-9}	
Happy Valley Fault	75082	5.86×10^{-9}	75081
Happy Valley Fault	75083	5.86×10^{-9}	75081
North Fault	76011	6.07×10^{-9}	
North Fault	76012	6.07×10^{-9}	76011
North Fault	76021	2.40×10^{-10}	
North Fault	76022	2.40×10^{-10}	76021
North Fault	76031	3.02×10^{-11}	
North Fault	76032	3.02×10^{-11}	76031
North Fault	76041	5.96×10^{-5}	
North Fault	76042	5.96×10^{-5}	76041
North Fault	76051	2.74×10^{-7}	
North Fault	76052	2.74×10^{-7}	76051
North Fault	76053	2.74×10^{-7}	76051
FSDF Fault	76061	1.00×10^{-7}	
FSDF Fault	76062	1.00×10^{-7}	76061
FSDF Fault	76081	1.00×10^{-7}	
FSDF Fault	76082	1.00×10^{-7}	76081
FSDF Fault	76101	1.00×10^{-7}	
FSDF Fault	76102	1.00×10^{-7}	76101
North Fault	76131	2.95×10^{-6}	
North Fault	76132	2.95×10^{-6}	76131
North Fault	76141	1.00×10^{-4}	
North Fault	76142	1.00×10^{-4}	76141
North Fault	76151	2.21×10^{-6}	
North Fault	76152	2.21×10^{-6}	76151
North Trace Fault	76161	3.07×10^{-9}	
North Trace Fault	76162	3.07×10^{-9}	76161
North Trace Fault	76171	9.76×10^{-7}	
North Trace Fault	76172	9.76×10^{-7}	76171
Coca Fault	77011	1.54×10^{-9}	

Coca Fault	77012	1.54×10^{-9}	77011
Coca Fault	77013	1.54×10^{-9}	77011
Coca Fault	77021	1.99×10^{-10}	
Coca Fault	77022	1.99×10^{-10}	77021
Coca Fault	77023	1.99×10^{-10}	77021
Coca Fault	77031	2.68×10^{-10}	
Coca Fault	77032	2.68×10^{-10}	77031
Coca Fault	77033	2.68×10^{-10}	77031
Coca Fault	77041	1.99×10^{-7}	
Coca Fault	77042	1.99×10^{-7}	77041
Coca Fault	77051	2.66×10^{-10}	
Coca Fault	77052	2.66×10^{-10}	77051
Coca Fault	77053	2.66×10^{-10}	77051
Burro Flats Fault	78011	2.88×10^{-8}	
Burro Flats Fault	78012	2.88×10^{-8}	78011
Burro Flats Fault	78013	2.88×10^{-8}	78011
Burro Flats Fault	78031	3.51×10^{-10}	
Burro Flats Fault	78032	3.51×10^{-10}	78031
Burro Flats Fault	78033	3.51×10^{-10}	78031
Burro Flats Fault	78041	4.58×10^{-10}	
Burro Flats Fault	78042	4.58×10^{-10}	78041
Burro Flats Fault	78043	4.58×10^{-10}	78041
Burro Flats Fault	78051	6.01×10^{-11}	
Burro Flats Fault	78052	6.01×10^{-11}	78051
Burro Flats Fault	78061	3.76×10^{-10}	
Burro Flats Fault	78062	3.76×10^{-10}	78061
Burro Flats Fault	78063	3.76×10^{-10}	78061
Burro Flats Fault	78071	4.35×10^{-10}	
Burro Flats Fault	78072	4.35×10^{-10}	78071
Burro Flats Fault	78073	4.35×10^{-10}	78071
Burro Flats Fault	78091	2.86×10^{-10}	
Burro Flats Fault	78092	2.86×10^{-10}	78091
Burro Flats Fault	78093	2.86×10^{-10}	78091
Burro Flats Fault	78101	2.57×10^{-11}	
Burro Flats Fault	78102	2.57×10^{-11}	78101
Burro Flats Fault	78111	1.91×10^{-10}	
Burro Flats Fault	78112	1.91×10^{-10}	78111
Burro Flats Fault	78121	1.07×10^{-10}	
Burro Flats Fault	78122	1.07×10^{-10}	78121
Burro Flats Fault	78123	1.07×10^{-10}	78121
Burro Flats Fault	78131	4.84×10^{-10}	

Burro Flats Fault	78132	4.84×10^{-10}	78131
Burro Flats Fault	78133	4.84×10^{-10}	78131
Burro Flats Fault	78141	2.29×10^{-10}	
Burro Flats Fault	78142	2.29×10^{-10}	78141
Burro Flats Fault	78143	2.29×10^{-10}	78141
Burro Flats Fault	78151	5.32×10^{-10}	
Burro Flats Fault	78152	5.32×10^{-10}	78151
Burro Flats Fault	78153	5.32×10^{-10}	78151
Burro Flats Fault	78161	2.02×10^{-10}	
Burro Flats Fault	78162	2.02×10^{-10}	78161
Burro Flats Fault	78163	2.02×10^{-10}	78161
Burro Flats Fault	78171	4.63×10^{-10}	
Burro Flats Fault	78172	4.63×10^{-10}	78171
Burro Flats Fault	78173	4.63×10^{-10}	78171
Burro Flats Fault	78181	4.71×10^{-10}	
Burro Flats Fault	78182	4.71×10^{-10}	78181
Burro Flats Fault	78183	4.71×10^{-10}	78181
Burro Flats Fault	78191	4.47×10^{-10}	
Burro Flats Fault	78192	4.47×10^{-10}	78191
Burro Flats Fault	78193	4.47×10^{-10}	78191
Burro Flats Fault	78201	5.25×10^{-10}	
Burro Flats Fault	78202	5.25×10^{-10}	78201
Burro Flats Fault	78203	5.25×10^{-10}	78201
Burro Flats Fault	78211	4.30×10^{-10}	
Burro Flats Fault	78212	4.30×10^{-10}	78211
Burro Flats Fault	78213	4.30×10^{-10}	78211
Lakeside North Fault	79011	4.96×10^{-9}	
Lakeside North Fault	79012	4.96×10^{-9}	79011
Lakeside North Fault	79013	4.96×10^{-9}	79011
Lakeside South Fault	80011	1.00×10^{-4}	
Lakeside South Fault	80012	1.00×10^{-4}	80011
Lakeside South Fault	80013	1.00×10^{-4}	80011
Lakeside South Fault	80021	9.60×10^{-10}	
Lakeside South Fault	80022	9.60×10^{-10}	80021
Lakeside South Fault	80023	9.60×10^{-10}	80021
Lakeside South Fault	80031	1.94×10^{-9}	
Lakeside South Fault	80032	1.94×10^{-9}	80031
Lakeside South Fault	80033	1.94×10^{-9}	80031
North Drain Fault	81011	2.52×10^{-10}	
North Drain Fault	81012	2.52×10^{-10}	81011
North Drain Fault	81021	4.44×10^{-10}	

North Drain Fault	81022	4.44×10^{-10}	81021
North Drain Fault	81051	4.82×10^{-10}	
North Drain Fault	81052	4.82×10^{-10}	81051
Tank Fault	82011	3.43×10^{-10}	
Tank Fault	82012	3.43×10^{-10}	82011
Tank Fault	82013	3.43×10^{-10}	82011
Skyline Fault	83011	8.87×10^{-8}	
Skyline Fault	83012	8.87×10^{-8}	83011
Skyline Fault	83013	8.87×10^{-8}	83011
Skyline Fault	83021	4.55×10^{-10}	
Skyline Fault	83022	4.55×10^{-10}	83021
Skyline Fault	83023	4.55×10^{-10}	83021
Skyline Fault	83031	3.75×10^{-10}	
Skyline Fault	83032	3.75×10^{-10}	83031
Skyline Fault	83033	3.75×10^{-10}	83031
Skyline Fault	83041	7.38×10^{-10}	
Skyline Fault	83042	7.38×10^{-10}	83041
Skyline Fault	83043	7.38×10^{-10}	83041
Ridge Structure	83051	2.02×10^{-6}	
Ridge Structure	83052	2.02×10^{-6}	83051
Ridge Structure	83053	2.02×10^{-6}	83051
CTL	83061	1.06×10^{-7}	
CTL	83062	1.06×10^{-7}	83061
CTL	83063	1.06×10^{-7}	83061
Pond Fault	83071	5.53×10^{-7}	
Pond Fault	83072	5.53×10^{-7}	83071
Pond Fault	83073	5.53×10^{-7}	83071
CTL	83081	1.46×10^{-9}	
CTL	83082	1.46×10^{-9}	83081
CTL	83083	1.46×10^{-9}	83081
IEL South Fault	874011	1.22×10^{-5}	
IEL North Fault	974011	4.47×10^{-11}	

Table 10: Calibrated recharge multipliers.

Unit number	Calibrated multiplier
1001010	0.0007
1001020	0.0621
1001030	0.0000
1002010	0.0213
1002020	0.0019
1002030	0.0000
1005000	0.0000
1009000	0.5000
1009010	0.3000
1009020	0.1457
1009030	0.3000
1009040	0.3000
1009050	0.3000
1009060	0.0139
1009070	0.0118
1009080	0.0071
1009090	0.0127
1009100	0.0180
1009110	0.0094
1009120	0.1010
1009130	0.3000
1009140	0.3000
1009150	0.3000
1009160	0.3000
1009170	0.3000
1009180	0.3000
1009190	0.3000
1009200	0.3000
1009210	0.3000
1009220	0.1627
1009230	0.1945
1009240	0.0908
1009250	0.1383
1009260	0.1789
1009270	0.3000
1009280	0.3000
1009290	0.3000
1009300	0.0020

1009310	0.1673
1009320	0.0885
1009330	0.0626
1009340	0.1339
1009350	0.1616
1009360	0.2205
1009999	0.0014